Extended Depth of Field Optical Projection Tomography

MSc Thesis

R. Djajadiningrat

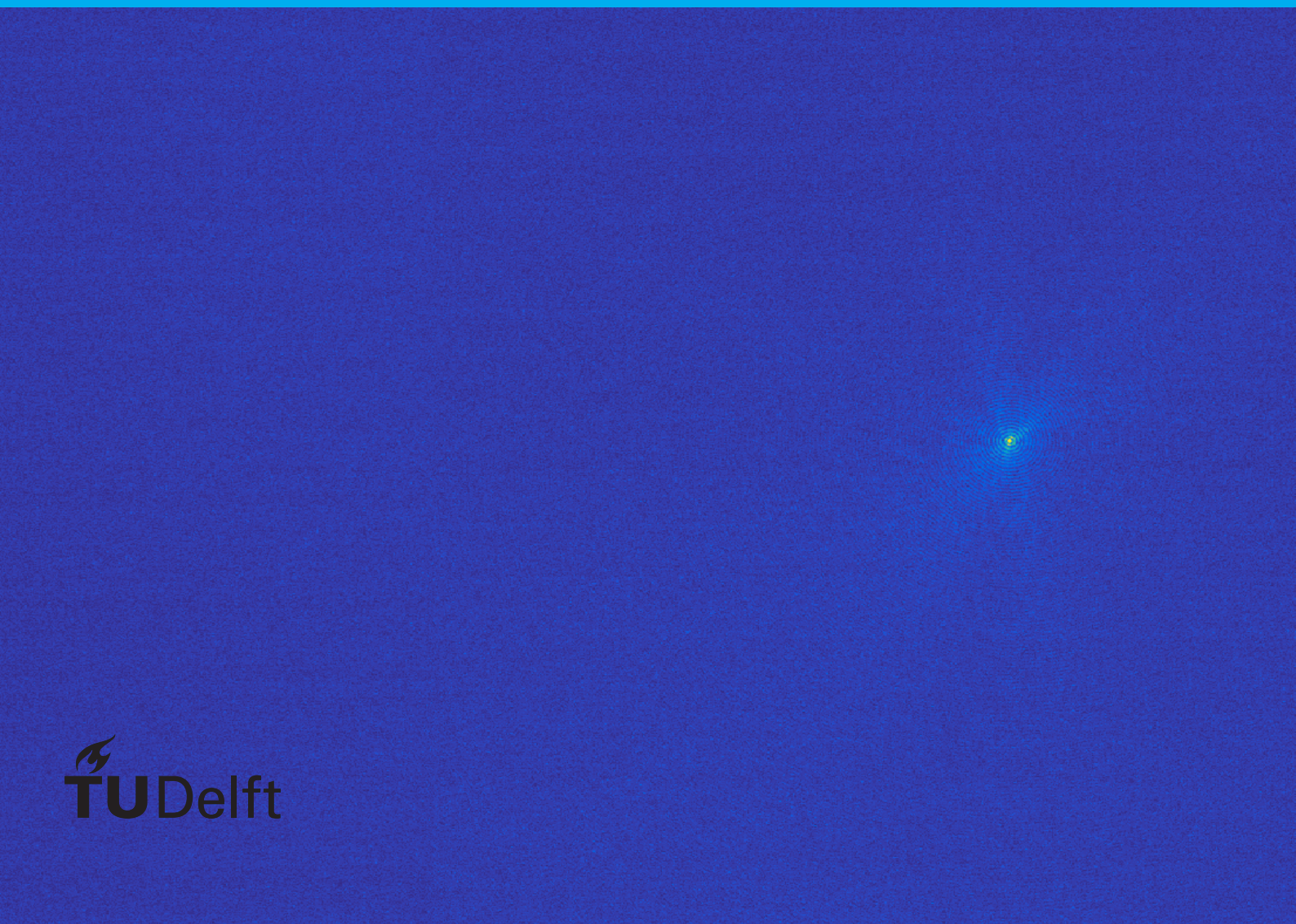

TU Delft

Extended Depth of Field Optical Projection Tomography

MSc Thesis

by

R. Djajadiningrat

to obtain the degree of Master of Science
at the Delft University of Technology
to be defended publicly on Monday November 26, 2018 at 10:30 AM.

Student number: 4012739

Thesis committee:

Dr. ir. J.C.F. de Winter,	TU Delft
Dr. J. Kalkman,	TU Delft
Dr. ir. J. van der Horst,	TU Delft
Prof. dr. S. Stallinga,	TU Delft

TU Delft

Abstract

3D optical projection tomography (OPT) is an optical imaging technique that allows for the reconstruction of biological samples of about a cubic centimetre with a resolution of several micrometres. It is a valuable optical imaging technique in biomedical research as measurements can be performed relatively fast and a full three-dimensional reconstruction of the sample can be made.

A limiting factor with regard to resolution in OPT is the limited depth of field (DoF) due to light detection with a Gaussian beam profile. In emission based OPT a sample is rotated to construct multiple images through excitation of fluorescent labels in the sample. An external source like a laser supplies energy and fluorophores achieve an excited state. As they return to their ground state a photon is emitted, and emission can be detected. The further the fluorescent light emitting source in the sample is removed from the centre of rotation in the focal plane, the more distorted the image is in tangential direction due to the limited DoF. The goal of this research is to extend the depth of field in Optical Projection Tomography.

The DoF limitations due to diffraction are mainly caused by the Gaussian beam shape and its inherent limitations such as a small high intensity spot and a small region of focus. A review of several DoF extension approaches shows that the most commonly used solution to the DoF problem is focus scanning. Here, the DoF is not increased but additional measurements with different DoFs are performed. This involves additional image acquisition and/or more complexity in imaging systems. A more fundamental approach to the problem is to find an alternative to the Gaussian beam shape. An alternative to Gaussian beams is found sporadically in the literature in the form of non-diffracting beams. Non-diffracting beams are beams that propagate without diffraction and show regenerative properties after obstruction. In theory, they have the same intensity distribution anywhere over propagation, i.e. an unlimited DoF. However, as these theoretical beams cannot be produced alternatives with finite DoF are considered.

The Bessel beam is a non-diffracting beam that is rotationally symmetric and displays a transversal high-intensity core. It can be generated without energy loss with a lens shaped like a rotationally symmetric prism, called an axicon. An analytic description of the axicon generated Bessel beam from the literature is presented and it is shown that, theoretically, an axicon with a base angle of 20° can produce a beam with a near uniform intensity distribution in the order of centimetres with a resolution in the order of micrometres. This combination of DoF and resolution is sufficient for OPT.

A propagation simulation of the axicon generated Bessel beam, using the Hankel transform as a rotationally symmetric alternative to the 2D Fourier transform, is performed and used to verify the analytic description of the axicon generated Bessel beam. A model of an imaging set-up of an axicon with an objective lens from the literature is presented for light collection. Simulations for coherent and incoherent paraxial point sources show that the imaging resolution increases as the object distance from the objective lens increases. The verified analytic description of axicon generated Bessel beams from the literature is integrated into theoretical descriptions of OPT from the literature. A description of the horizontal sections of the 2D projections in OPT with an axicon generated Bessel beam is derived. A numerical OPT simulation shows that OPT reconstructions of point sources show virtually no blurring, but do show concentric rings due to the intensity distribution of the Bessel beam. These rings can be removed by deconvolution of the projection or deconvolution of the reconstruction of simulated OPT results with the imaging point spread function (PSF) of the axicon-generated Bessel beam. The PSF describes the response of the imaging system to a point source.

Practical work is presented with the imaging set-up of an axicon with an objective lens as described earlier. A bright point source is emulated by illumination of a small aperture to obtain an experimental PSF. The resolution of the PSF is analysed over paraxial distance from the objective lens for both coherent and incoherent illumination. The same is done for a resolution target in transmission. Comparison of the Bessel system with Gaussian models show that the DoF increase shown by the Bessel system is significant in all cases. It is found that for sources with spatially narrow intensity distributions (near-point source) the PSF resolution

matches theoretical predictions. However, as the spatial light source distribution increases slightly, Bessel distributions overlap spatially. This creates artefacts and deteriorates the resolution.

It is concluded that extended depth of field in OPT can be achieved with non-diffracting axicon generated Bessel beams. However, for objects larger than point sources the resolution deteriorates. Furthermore, the means of illumination are a major influence on the resulting images when using an axicon.

Further research on the optimization of illumination is recommended. Additionally, recommendations for further research on the significance of self-regeneration are made. The use of axicons with a lower base angle may decrease regeneration effects. Recommended applications for use of Bessel beams in optical imaging are those where a large DoF is desired and high resolution is less of a priority, or imaging and OPT of very sparse but large samples. Apertured Bessel beams are recommended for use in scanning applications, where the Bessel distribution overlay will not be an issue and resolution remains high.

Lastly, an OPT outlook is given. A final exploratory transmission OPT measurement of ceramic beads in agarose is performed. The reconstruction results show poor resolution and contrast. This aligns with the earlier experimental findings and consolidates the recommendations.

Preface

This thesis 'Extended Depth of Field Optical Projection Tomography' describes my research project aimed at advancing the quality of an object reconstruction out of multiple images, by increasing the distance at which an object appears sharp in such an image. It has been written to obtain the degree of Master of Science at the Delft University of Technology. The research has been exciting and absorbing, and has grabbed my full attention for the past nine months.

I would like to thank Dr. Kalkman for giving me the chance to take on this interesting project. As a Mechanical Engineering student with a background in robotics I wanted to discover the field of imaging and Dr. Kalkman has allowed me to do so, providing me with excellent supervision along the way. I would like to thank Dr. ir. Van der Horst for his excellent guidance and support during this project, both at our desks and in the lab, and for always being available for help and advice. Furthermore I would like to thank my thesis committee chair Dr. ir. De Winter for taking me on for supervision and providing me with constructive comments throughout the research process. I would also like to thank Prof. dr. Stallinga for the time and effort he has put into joining my thesis committee.

Thank you to my family and friends for batting ideas around about the research. Special thanks to Marnix for helping me with several mathematical derivations and my room-mates for proofreading my work.

I hope you enjoy your reading.

Roel Djajadiningrat

R. Djajadiningrat
Delft, 12 November 2018

Contents

Abbreviations and Symbols

DoF	Depth of Field
FBP	Filtered Back Projection
FDR	Frequency Distance Relationship
LSM	Light Sheet Microscopy
OCT	Optical Coherence Tomography
OCPT	Optical Coherence Projection Tomography
OPT	Optical Projection Tomography
OTF	Optical Transfer Function
PSF	Point Spread Function
PT	Phase Tomography
SLM	Spatial Light Modulator

α	Axicon base angle [rad]
β	Axicon conical angle [rad]
U	Electric field [V/m]
I	Intensity [W/m^2]
J_0	Zero-order Bessel function
k	Angular wave number [m^{-1}]
λ	Wavelength [m]
ω	Gaussian beam waist [m]
P	Power [W]
ρ	Radial distance [m]
z_{max}	Range of uniform intensity distribution [m]
Z_R	Rayleigh Range [m]

1 Introduction

Optical projection tomography, or OPT, is a form of imaging that allows for the creation of three-dimensional reconstructions of biological samples [43]. In OPT a sample is rotated and imaged repeatedly under multiple angles. This is different from most imaging techniques, where images are made by lateral scanning in a reflection geometry. OPT can be transmission based, where the observed light has been sent through the sample, or emission based, where the observed light is emitted by activated fluorescent labels. Figure 1.1 shows the working principle of emission based OPT. OPT is a valuable optical imaging technique in biomedical research as measurements can be performed relatively fast and a full three-dimensional reconstruction of the sample can be made. A limiting factor with regard to resolution in OPT is the limited depth of field, or DoF [43] [40] [41] [24]. The DoF can be described as the distance where objects appear acceptably sharp in an image. A limited DoF poses a problem in almost all imaging techniques which is why scanning mechanisms are often used to maintain a high resolution for all depths in the image. However, in OPT a complete volume is imaged without scanning or optical sectioning. Hence, volumes outside the DoF are also considered as information carriers. The reconstruction of these out of focus volumes is blurred. Consequently, we wish to extend the DoF in OPT, so that objects in the entire volume can be imaged with a high resolution.

Obtaining images without blurring in single detector OPT has not yet been achieved. Recently, the use of non-diffracting Bessel beams has shown to increase the DoF in several optical imaging techniques [32] [34] [22] [50] [51] [25] [46].

The goal of this research is to explore the use of non-diffracting Bessel beams for depth of field extension in OPT. The research question of this research is: 'Can an extended depth of field in optical projection tomography be achieved with non-diffracting Bessel beams?'

In this thesis extension of the DoF in 3D OPT is investigated, the non-diffracting Bessel beam is investigated, numerical simulations are used and practical work is performed. The results are discussed and recommendations for further research are made.

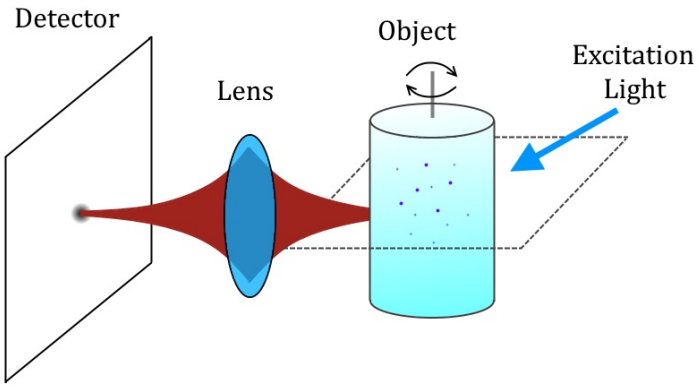

Figure 1.1: Emission OPT working principle: fluorescent labels in the object are excited and the emitted light is detected through a lens system. Measurements on the object are performed for different angles and used for a 3D reconstruction of the object. Source: Adaptation of [41].

Thesis Layout

In Chapter 2 the challenge regarding DoF and resolution in optical imaging is identified and state-of-the-art optical tomography based imaging techniques, including OPT, are reviewed. In Chapter 3 DoF extension with non-diffracting beams is elaborated on, and the choice for further exploration of the Bessel beam generated by an axicon lens is explained. This is followed by a description of the intensity distribution of axicon lens generated Bessel beams in Chapter 4. In this chapter an axicon lens set-up for light collection is elaborated on, and a Bessel beam simulation is presented and compared to the analytic description. In Chapter 5 a theoretical discussion of OPT based on the literature is shown, and a novel theoretical derivation for OPT with an axicon generated Bessel beam is presented. Also, the principles behind several computerized image reconstruction methods are discussed. The analytic description of the previous chapter is then used for an OPT simulation and simulated image reconstruction. Chapter 6 presents the methods and materials used to perform practical work with regard to DoF extension with axicon generated Bessel beams. The results of this work are presented in Chapter 7. This thesis is completed with conclusions, a discussion and an OPT outlook in Chapter 8.

2

Challenges in Optical Imaging

In this chapter an overview of the challenges and techniques in optical imaging is established. In the first section of this chapter an introduction to optical imaging in biomedicine is given. Several imaging concepts are established and the DoF problem is explained. Several optical tomography imaging techniques, including OPT, are discussed. Then, OPT and blurring in OPT are elaborated on in more detail.

2.1. Optical Imaging in Biomedicine

In optical imaging (near) visible light and the properties of photons are used to obtain detailed images of organs, tissues, cells and smaller structures. Optical imaging plays a great role in life sciences research and disease diagnosis and treatment. An overview of different optical imaging techniques and their corresponding resolutions and imaging depths is shown in Figure 2.1. In optical imaging non-ionizing radiation is used, and samples are not exposed to harmful radiation. Images are generated with detection of large quantities of near-infrared photons, making it much safer than imaging techniques which use ionizing radiation. Therefore, optical imaging is suitable for long repeated procedures. Because of the variety of ways different types of biological tissue absorb and scatter light, optical imaging is particularly useful for visualizing soft tissues.

Scattering & Absorption

In essence, assuming no change in the energy of the photon, scattering is the change in propagation direction of a photon [39]. Photons can undergo multiple scattering events during propagation, depending on the medium through which they travel. Particles may scatter light in all directions or mainly in the forward direction, depending on the size of the particle, causing both spatial and temporal blurring of a light pulse. When imaging through turbid media, spatial blurring degrades the image as the travelled path of the detected light is unknown.

In Figure 2.1 OPT is categorized under the red and purple areas which visualize optical techniques which operate with an imaging depth in the range of 0.1 µm to 1 mm [42]. Ideally, researchers would like to obtain high-resolution images throughout large volumes of tissue in small amounts of time. However, the physical interactions of photons with tissue raise issues with regard to imaging large volumes at high resolution. Physical interactions of the information carrier with the imaging system or a sample deteriorate the image quality as the imaging depth increases. As a result, imaging depth is limited and is only increased at the cost of resolution. The concepts 'depth of field' and 'resolution' are discussed from here on.

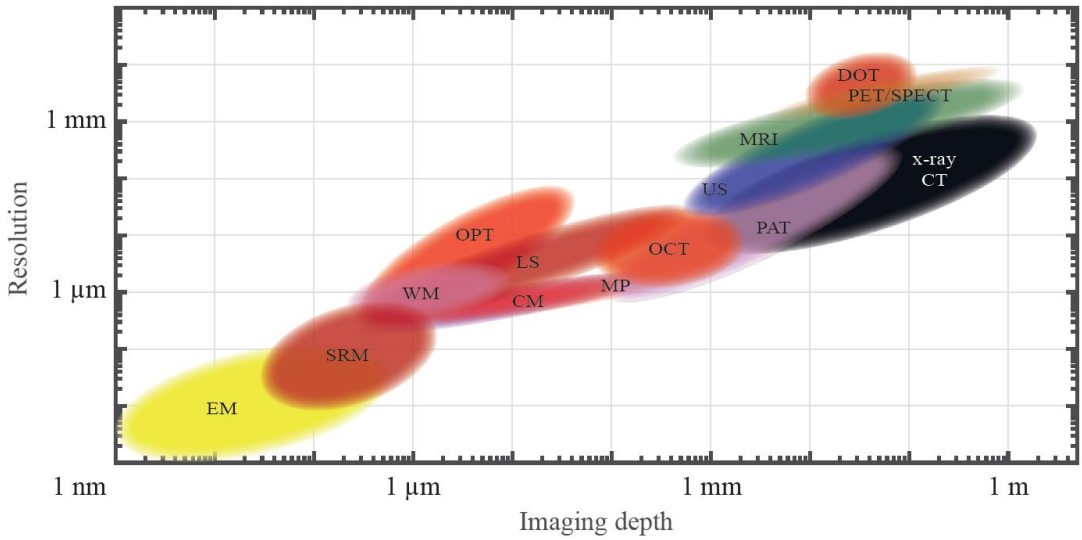

Figure 2.1: Resolutions and imaging depths for different 3D imaging techniques: EM: electron microscopy, SRM: super-resolution microscopy, WM: widefield microscopy, OPT: optical projection tomography, LS: light sheet microscopy, CM: Confocal microscopy, MP: Multi-photon microscopy, OCT: Optical coherence tomography, PAT: Photoacoustic tomography, US: Ultrasound, MRI: Magnetic resonance imaging, CT: computed tomography, DOT: Diffuse optical tomography, PET: Positron emission tomography, and SPECT: Single photon emission computed tomography. Source: [42]

2.2. Spatial resolution and Depth of Field

Depth of Field or DoF can be described as the distance where objects appear acceptably sharp in an image. Figure 2.2a shows two images of the same setting with an extreme difference in DoF. A large difference between the decrease in detail from the plane of focus for the two images can be seen. The left image has been captured with a system with a relatively small DoF and the right image has been captured with a system with a relatively large DoF. Spatial resolution refers to the ability of a system to distinguish small details of an object. The higher the resolution, the smaller distinguishable objects are. Figure 2.2b shows two images of the same setting with an extreme difference in spatial resolution. In the high-resolution image more details can be discerned than in the low-resolution image.

In imaging with Gaussian beams a trade-off between the resolution and the DoF is present. In this paragraph the Gaussian beam is elaborated on and the resolution and DoF trade-off is explained for this beam.

2.2.1. Diffraction

When light waves from different parts of a wavefront meet interference takes place, causing diffraction when obstacles are encountered. Diffraction from an obstacle results in deviations from the classical straight ray model for light propagation. Figure 2.3a shows diffraction of light through an aperture. According to the straight ray model, a lens creates an infinitely small spot focus as shown in black in Figure 2.3b. However, in reality a flat wavefront with a Gaussian intensity profile creates a focus with a finite spot size due to diffraction effects, shown in the same figure in red. The maximum resolution of optical imaging systems without limiting factors in the set-up , i.e. lens imperfections or misalignment, is limited by diffraction.

(a) Left: photo of bottle caps with small DoF. Right: photo of bottle caps with large DoF.

(b) Left: photo of a hand with high spatial resolution. Right: photo of a hand with low spatial resolution.

Figure 2.2: Examples of difference in DoF and resolution. Sources:
(a) *https://nl.pinterest.com/pin/816347869928675932/?lp=true* and
(b) *http://lrrpublic.cli.det.nsw.edu.au/lrrSecure/Sites/Web/1144B/ndt/content/radiographic/CTScanning/CT.htm*

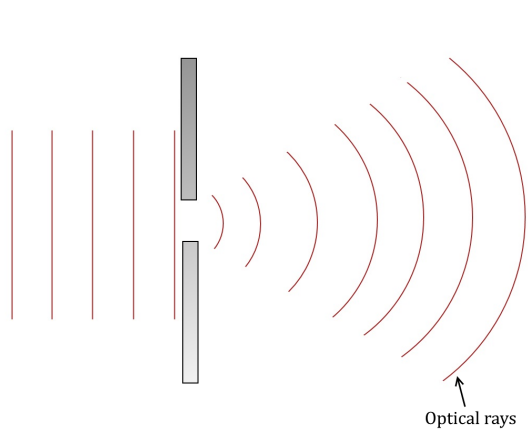

(a) Diffraction through an aperture for a plane wave.

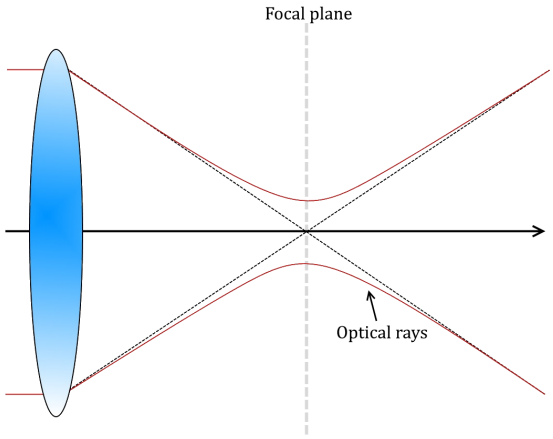

(b) Diffraction after a lens with straight rays in black and a Gaussian beam shape due to diffraction in red.

Figure 2.3: Diffraction effects due to an aperture and a lens. The optical rays are depicted in red.

2.2.2. Gaussian Beam

Gaussian beams are considered in situations where the beam divergence is relatively small, and the paraxial approximation can be applied. In general, laser-beam propagation can be approximated by assuming that the laser beam has an ideal Gaussian intensity profile. The electric field strength during propagation in z-direction of such a beam can be described in $x, y, z-$coordinates by [38]:

$$U(x,y,z) = \frac{\exp\left(\frac{2\pi j z}{\lambda_0}\right)}{2\pi\omega_0^2 + j\lambda_0 z} \exp\left(-\frac{\pi(x^2+y^2)}{2\pi\omega_0^2 + j\lambda_0 z}\right), \tag{2.1}$$

where ω_0 is the smallest half beam waist size as shown in Figure 2.4, λ_0 is the free-space wavelength and $j = \sqrt{-1}$. The Gaussian beam light intensity is at its maximum in focus. In Figure 2.5 an example of the normalised intensity distribution of a focused Gaussian beam can be seen. The high intensity region at the focus of the beam determines the DoF of the beam. For imaging it is desired that this high intensity region is large in the propagation direction in order to obtain a large DoF and therefore a large imaging depth. However,

it is desired that the intensity distribution is small along the lateral $x, y-$direction to achieve a high spatial resolution. The interplay between DoF and resolution is discussed from here on.

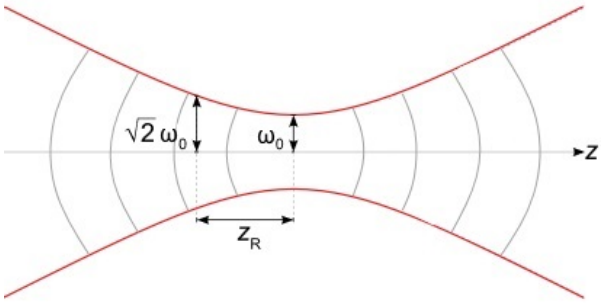

Figure 2.4: Gaussian beam in the propagation plane, with half-width in focus ω_0, Rayleigh range Z_R and wavefronts in grey. Source: adaptation of *https://en.wikipedia.org/wiki/Gaussian_beam* .

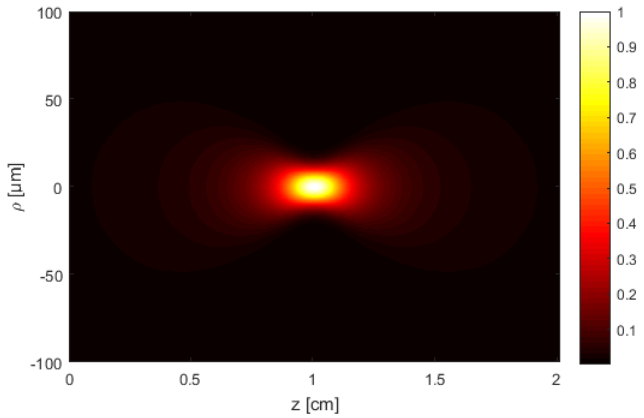

Figure 2.5: Normalized intensity distribution of a focused Gaussian beam in the propagation plane. With $\omega_0 = 10$ µm, $\lambda = 550$ nm, radial coordinate ρ and propagation direction z.

2.2.3. Resolution and Depth of Field Trade-off

In every Gaussian imaging system a trade-off between spatial resolution and DoF is present. To achieve a high spatial resolution in imaging a small beam waist ω_0 is desirable. However, the Rayleigh range, the distance over which a Gaussian beam increases its cross-sectional area by a factor two, is defined by $Z_R = \pi\omega_0^2/\lambda_0$ for $\omega_0 \geq 2\lambda/\pi$ [28]. One can easily see that the Rayleigh range becomes very small when a very small ω_0 is chosen. To illustrate this, in OPT a spatial resolution corresponding to $\omega_0 = 3$ µm can be desirable. For $\omega_0 = 3$ µm and $\lambda_0 = 550$ nm the Rayleigh range is $Z_R = 51.4$ µm. In OPT imaging of biological tissue of several millimetres thickness a doubling of cross-sectional beam area every 51.4 µm will cause tremendous blurring in the out-of-focus regions of a sample in OPT. It is obvious that a compromise has to be made between resolution and depth of field, due to the physical limitations of the imaging system.

2.3. Approaches for DoF Extension

The diffraction problem described above limits the DoF in optical imaging with Gaussian systems. Approaches to counter the resolution and DoF trade-off problem are discussed from here on.

Focus Scanning

An obvious way to increase the region of focus without sacrificing spatial resolution is the execution of additional measurements with different focal planes. For microscopy this is achieved with through-focus scanning. For a technique such as OPT, where projections are made under different angles, an additional measurement with the focal plane moved out of the axis of rotation into an otherwise out-of-focus region can provide more detailed images of otherwise blurred regions of the image [9].

Computerized Deblurring

Blurring in an image due to a limited DoF can be removed through computerized reconstruction. An example in OPT is the method of image deconvolution, where the blurring is predicted and corrected for with post-processing [43]. Deconvolution and other computerized methods are discussed in more detail in Section 5.2.

Non-Diffracting Beams

As shown in Section 2.2 the use of Gaussian beams comprises a trade-off between resolution and DoF; the larger the DoF, the lower the resolution and vice versa. Non-diffracting beams are a special type of beam which can be made to have a relatively large DoF, independent of their resolution [14] [13]. These beams are formed by wavefront interference phenomena that show self-regenerating properties, which, to a certain degree, may prove useful for imaging in turbid media [15]. The price for these unique properties is that the beams yield a lower peak intensity than comparable focused Gaussian beams as non-diffracting beams usually have an energy distribution over a large area. Nevertheless, non-diffracting beams are currently very popular in research. Non-diffracting beams and some of their current applications are discussed in Chapter 3 and Appendix A.

The use of non-diffracting beams in OPT has not yet been explored. As the restriction in the DoF posed by the Gaussian beam shape constitutes one of the main issues in image quality in OPT and other wide-field imaging techniques, the use of non-diffracting beams with extended DoF shows potential to achieve improvements in OPT. A prerequisite is the possibility to reconstruct OPT images made with non-diffracting beam shapes.

2.4. Optical Tomography Imaging Techniques

Optical tomography is the collective name for forms of computed tomography. Images made from light transmitted and scattered through an object are reconstructed to create a digital volumetric model of an object. It is mostly suited for research on soft tissue as its working principle relies on the light-transmittance of the object. Several variants of optical tomography are discussed here.

PT Phase tomography, or PT, uses information concerning changes in the phase of the light beam that passes through an object in order to create its images. Typically, holographic imaging is used to record the light field for each projection. An object is illuminated from various angles. The beam's phase shift caused by the sample is extracted from the recorded projections and the phase shift in each point of the three-dimensional object can be retrieved. The phase shift in a point is proportional to the refractive index that the light field has accumulated along its path through the object and the object can be reconstructed using a reconstruction algorithm [16].

OPT Optical Projection Tomography, or OPT, typically has a resolution in the order of several microns, and can cover relatively large samples of about a cubic centimetre [45]. The entire sample is considered because in OPT a sample is imaged and rotated, to obtain many images from many different angles. Computerized reconstruction is then used to combine the different images and construct a 3D model of the sample. OPT can be either emission based, where fluorescent labels in a sample are excited and emit light which is observed by the imaging system, or transmission based, where light is transmitted directly through the sample and observed by the system. OPT will be discussed in more detail in the next section and a more theoretical elaboration on OPT is given in Chapter 5.

OCT Another variant of optical tomography is Optical Coherence Tomography, or OCT, where the interference properties of coherent wave forms are used to measure a backscattering profile of the sample along the direction of light propagation [21]. In OCT, scanning mechanisms are used as opposed to OPT where the sample as a whole is imaged for each angle.

OCPT Very recently another form of tomography called Optical Coherence Projection Tomography, or OCPT, has emerged. This form of tomography combines many different methods such as heterodyne detection (a method of extracting information encoded as modulation of the phase and/or frequency of light), confocal gating, coherence gating and time gating. This technique has been used to image a non-transparent adult zebrafish in high resolution with an imaging depth of 4 mm [42].

As stated, in the research presented in this report the focus will be on OPT. But problems concerning DoF versus resolution exist in all optical tomography techniques for which the results of this work may also be applicable.

2.5. Optical Projection Tomography

In this section an overview of OPT image acquisition, image reconstruction and limited DoF effects is given. A theoretical elaboration on OPT and reconstruction techniques is given in Chapter 5. OPT is a valuable optical imaging technique in biomedical research as measurements can be performed relatively fast, and a full three-dimensional reconstruction of the sample can be made. Because (near) visible light is used, lenses can be used in the imaging process to achieve several micrometer spatial resolution. A limiting factor with regard to resolution in OPT is the limited DoF due to transmission or emitted light detection with a Gaussian beam profile.

Working Principle

In transmission OPT light is sent directly through an object and observed by the imaging system. An example of emission based OPT is shown in Figure 2.6a: a sample is rotated to construct multiple images through excitation of fluorescent labels in the sample. A top view of the sample can be seen in Figure 2.6b. The further the fluorescent light emitting source in the sample is removed from the Gaussian beam focal plane, the more blurring will occur in the sinogram. For each full rotation each off-centre point will be located in the focal plane twice. Figure 2.7 shows an off-centre point source and the evolution of the corresponding sinogram with projections observed by the detector for angles up to $\theta = 0°, 90°, 180°, 270°$ and $360°$. Figure 2.7b indicates the blurring that occurs in the sinogram when the point source is out of focus.

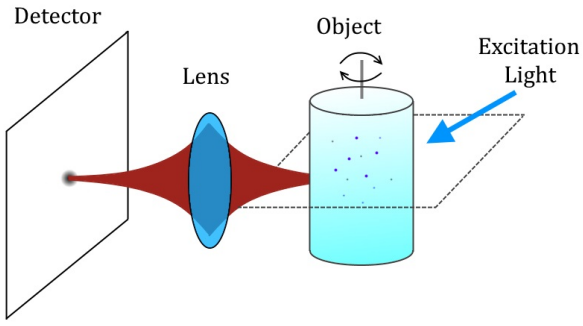

(a) Emission OPT working principle: fluorescent labels in the object are excited and the emitted light is detected through a lens. Measurements on the object are performed for different angles.

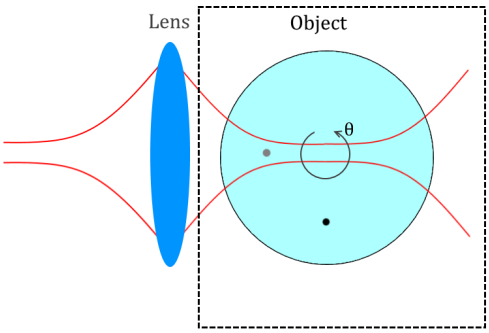

(b) Top view: the black fluorescent label is in the focal plane, the grey label is out of focus.

Figure 2.6: OPT working principle. Adaptation of [41].

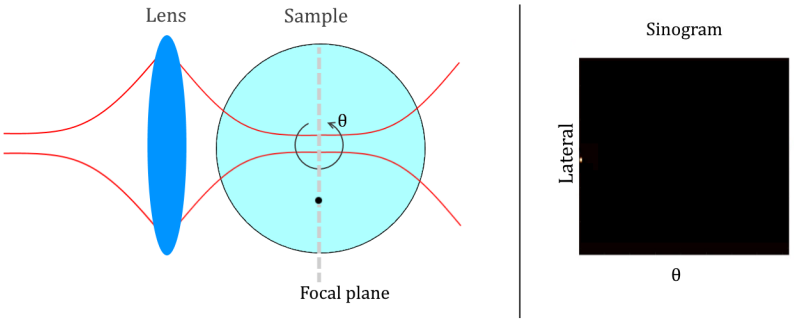

(a) $\theta = 0°$, the point source is located in the focal plane.

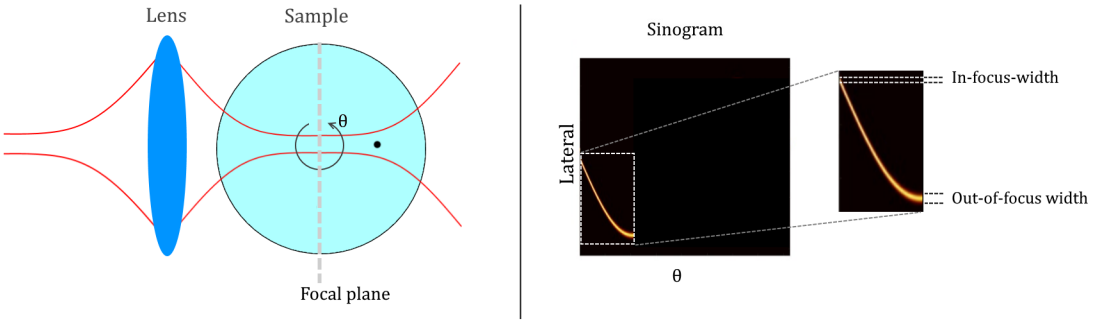

(b) $\theta = 90°$, the point source is out of focus, blurring occurs in the sinogram; the sinogram width has increased.

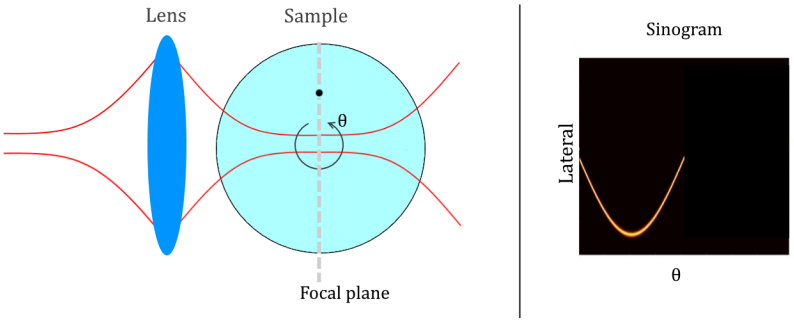

(c) $\theta = 180°$, the point source has returned to the focal plane and the sinogram width has decreased again.

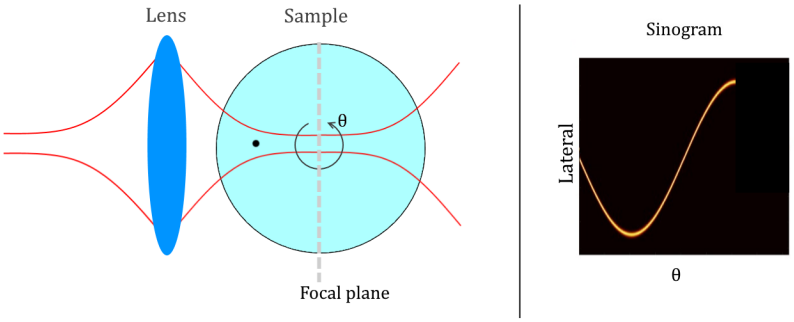

(d) $\theta = 270°$, the point source is out of focus, blurring occurs again; the sinogram width has increased.

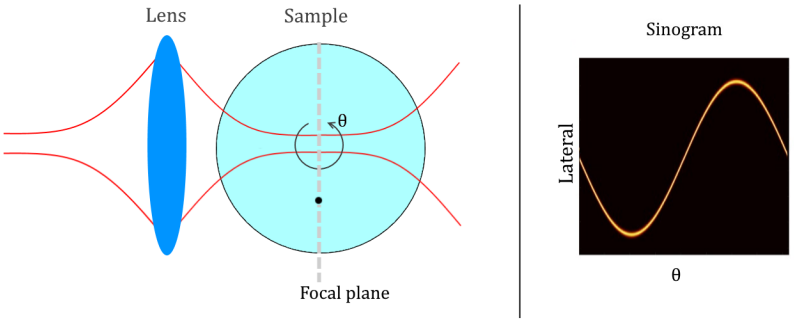

(e) $\theta = 360°$, the point source has returned to its original location.

Figure 2.7: Top view of OPT of a single point source (visualized by the black dot) and the corresponding sinogram with projections observed by the detector laterally up to $\theta = 0°, 90°, 180°, 270°$ and $360°$.

Image Reconstruction

As shown in Figure 2.7 the collection of OPT measurements for a full object rotation can be presented as a sinogram. For an off-centre point in the object, the lateral position with respect to the detector will change during rotation, and the consecutive presentation of the subsequent projections resembles a sinus, hence the name sinogram. This set of projections is effectively the Radon transformation of the structure of the object [24]. Strictly speaking, the Radon transform is valid only for straight ray tomography with an infinite number of projections. Still, the inverse Radon transform can be used to transform the raw projections of the sinogram into a reconstruction of the object. An example of the sinogram of an off-centre point obtained with OPT and the reconstruction obtained with the inverse Radon transform can be seen in Figure 2.8. The further a point in the object is removed from the axis of rotation, the larger the blurring in the sinogram will be when it is out of focus. Simulations and experiments have shown that an increase of the distance from the centre of rotation results in an increase in blurring in the tangential direction, which is perpendicular to the radial direction, in the reconstructed image [43]. Figure 2.9 shows nine different reconstructions for OPT of nine different point sources, positioned at (x_i, y_i), and the FWHM (Full Width at Half Maximum) of the intensity distribution of the reconstruction in radial and tangential direction as a function of the point's radial distance from the centre of rotation. An increase in the tangential blurring can be seen for an increase in radial distance from the centre of rotation but the radial resolution remains constant.

After a reconstruction is obtained, additional reconstruction methods to counter unwanted effects like the blurring due to defocus, can be applied to increase the image quality. Several reconstruction methods are discussed in Section 5.2.

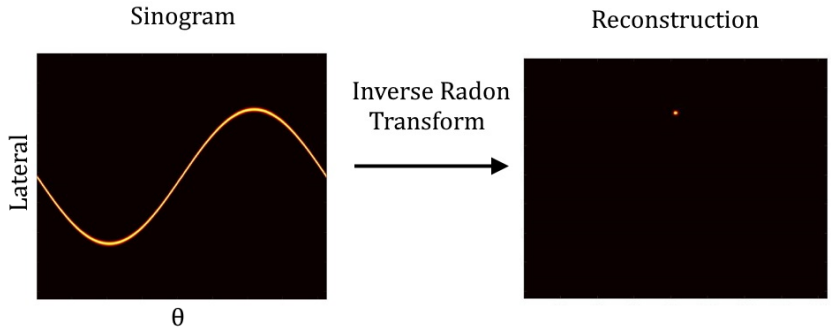

Figure 2.8: An example of the inverse Radon transform of a sinogram.

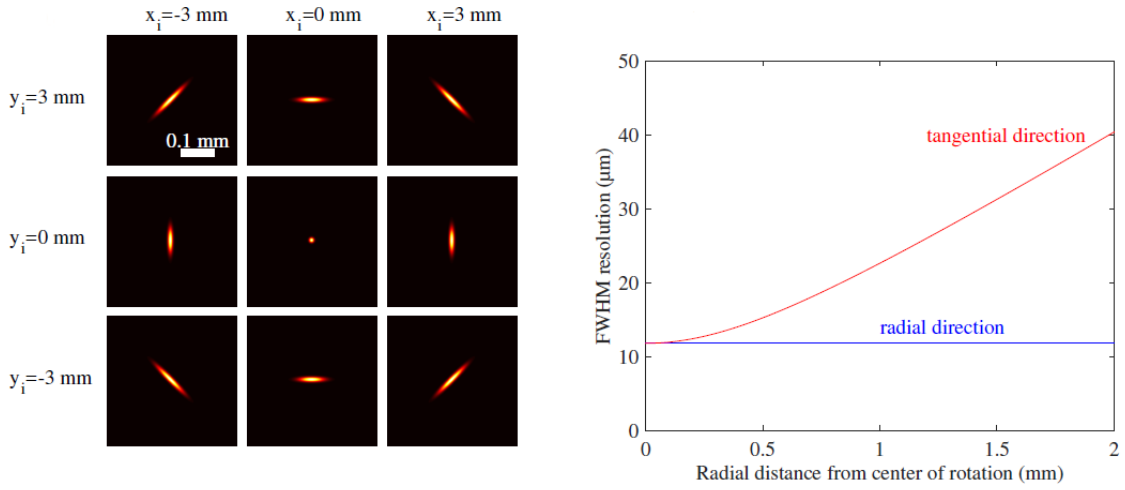

Figure 2.9: Left: Image reconstructions for point sources at different positions (x_i,y_i) in the object. Right: Radial and tangential Full-Width-at-Half-Maximum resolution as a function of the radial distance from the centre of rotation. ω_0 = 10 µm and λ = 515 nm. Source: [43].

Samples

The most widely used biological samples for OPT are zebrafish because of their small size and the ex utero development of transparent embryos. Zebrafish lose their transparency as they develop although transparent adult mutants are available [33]. An ideal scenario would be one where OPT would be performed on a living organism multiple times throughout its life to track, for example, the development of a tumor. This would reduce the number of samples needed for research and would allow the tracking of individuals. Optical clearing is performed to increase the transparency of samples like older zebrafish. The water inside a biological object can be replaced by a solution with a higher refractive index. This reduces the refractive index contrast between cellular structures and the fluid in between these structures. Subsequently, the scattering coefficient of the tissue is reduced for large pieces of tissue making the tissue more transparent. This process is called optical clearing [53]. Optical clearing of biological samples can take weeks to complete due to the extensive chemical processing required. Most optical clearing agents are not suitable for in-vivo imaging, and those that are offer only modest improvements with unknown long term effects on the living tissue [53]. Thus, optical clearing of the sample is unsuitable for in-vivo OPT. However, to achieve the best result, optical clearing is needed in OPT to reduce scattering effects.

If the extended DoF and the self-healing properties of non-diffracting beams would sufficiently reduce scattering effects during imaging, sample clearing may no longer be necessary in OPT. However, self-healing may also occur at the cost of useful information.

2.5.1. Depth of Field Extension in OPT

Ideally, the shape of a beam used for OPT would have both a small radius high intensity beam core corresponding to a high resolution and a large DoF which would minimize image blurring due to defocus. This is not the case for Gaussian beams. Several approaches are known to increase the DoF with Gaussian beams. As mentioned, a straight-forward solution is the execution of multiple measurements at different focal positions [9]. Data is recorded from multiple focal planes and the DoF issue is resolved. However, this involves an increase in measuring time and/or an increase in the complexity of the OPT system. Computerized deblurring can be applied but the outcome of the deconvolution of the measurement and the beam description is tied to the Gaussian data that is available.

Since the diffraction limitations are inherent to the Gaussian beam shape alternative beam shapes ought to be considered for OPT. Non-diffracting beams, as described in Section 2.3, have a relatively large DoF and may even hold self-healing properties in turbid media [15]. With these properties, they may be useful in solving the limited DoF problem in OPT. In the next chapter different non-diffracting beams are assessed for use in OPT for DoF extension.

3

Depth of Field Extension with Non-Diffracting Beams

As has already been mentioned in Section 2.3, non-diffracting beams show potential to serve DoF extension in OPT. In this chapter the properties of non-diffracting beams are discussed. The properties of the Bessel beam are given special attention.

3.1. Non-Diffracting Beams

Beams that propagate without diffraction are called diffraction free beams or non-diffracting beams [14] [13]. The terms 'non-diffracting' and 'diffraction free' are controversial as diffraction is only strictly absent for theoretical non-diffracting beams with an infinite propagation distance, carrying an infinite amount of power. These theoretical true non-diffracting beams cannot be realized as that would violate the law of conservation of energy. Therefore, realized non-diffracting beams are often referred to as quasi non-diffracting beams, or the beam type with which they are constructed is added to the name, i.e. 'Bessel-Gauss' beam. In this thesis the term 'non-diffracting' will be used nonetheless. In practice, the distance that a non-diffracting beam can propagate without significant alteration in their transverse profiles is limited by the design of the optical system. In the context of the research presented in this thesis, samples are within this distance and these beams can be considered to be practically non-diffracting.

Although there are multiple kinds of non-diffracting beams, all of them share key characteristics: an extended range of uniform intensity distribution resulting in an extended DoF with regard to optics, and self-reconstructing capabilities after perturbations are met. The term 'non-diffracting beams' was first proposed by Durnin in 1987 [13]. Free-space, beamlike exact solutions of the wave equation were presented, not subject to diffraction. The solutions are nonsingular and often have sharply defined intensity distributions which can be as small as several wavelengths. Mathematical theory on non-diffracting beams is lengthy but here we focus on the application of these beams. From here on, Bessel beams are elaborated on. The choice for use of Bessel beams in OPT DoF extention rather than alternative non-diffracting beams can be found in Appendix A.

3.2. Bessel Beam

The Bessel beam was the first beam to be discussed in early research concerning non-diffracting beams [13] [14]. In the lateral profile of the zeroth-order Bessel beam a high intensity core surrounded by numerous concentric rings are found. In the case of the ideal Bessel beam an infinite amount of energy would extend the beam indefinitely in the radial direction. Realistic spatially limited approximations can be generated, still with long ranges of uniform intensity distribution [11]. Bessel beam shapes are then achieved by creating interference patterns. An example of a typical finite Bessel beam is shown in Figure 3.1. This example is generated by illuminating an axicon with a Gaussian beam. The color bar indicates the normalized intensity. The long, relatively thin beam core allows for a large DoF in imaging with a high resolution. The dimensional parameters of real life Bessel beams are dependent of the method of generation, more on this in Section 3.3

and Chapter 4.

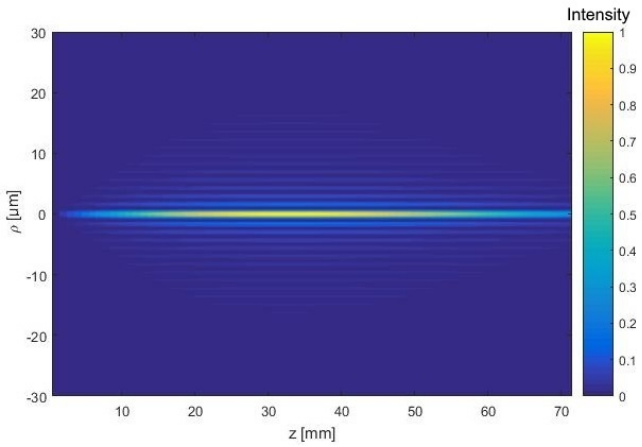

(a) Typical finite Bessel profile in the propagation plane.

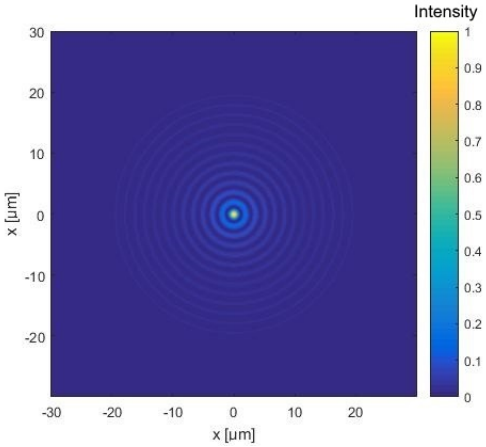

(b) Lateral cross-section of the Bessel beam with maximum intensity.

Figure 3.1: Bessel beam intensity profile in x, z-plane **(a)** and cross section in the y, z-plane at z=35 mm **(b)** for a Bessel beam with axicon angle $\alpha = 20\,°$, ω_0 =0.01 cm and $\lambda = 550$ nm. Note the high intensity beam core with many concentric rings which decrease in intensity with distance from the centre.

Bessel Beam Fringe Construction

This section serves to explain the principle of self-interference and the construction of the concentric rings in a Bessel beam. Figure 3.2 shows the 2D cross-section of an axicon lens, which in 3D is shaped like a circularly symmetric rounded prism. The shape of the lens refracts all radii of an incoming beam towards the paraxial axis, the axis denoted by z. The beam intersects itself, and within the intersection volume a pattern of standing waves emerges in the form of parallel lines. These lines, bright red in Figure 3.2, are oriented parallel to the bisector of the angle between the two beam segments. High amplitudes are produced by constructive interference (bright red lines) with low amplitudes in between, due to destructive interference. The result is a range of uniform intensity distribution. Note that the situation is circularly symmetric and what are referred to as 'beam segments' and 'lines' in this 2D representation, are in fact cylindrical shells of light in 3D. Also, in this simplified explanation the intensity profile of the incident beam has been left undiscussed. In this example the beam is constructed with a lens but in the next section multiple methods to construct Bessel beams will be discussed.

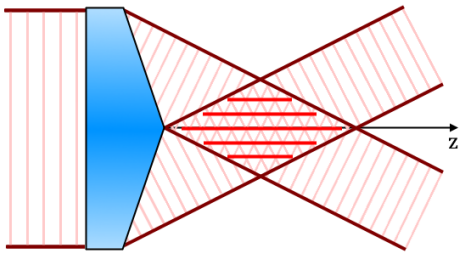

Figure 3.2: Schematic representation of fringe construction due to self interference. In this example a Bessel beam is created with an axicon lens.

The use of Bessel beams in imaging poses some challenges. Obviously, the concentric rings will result in artefacts in the generated image and will have to be dealt with either physically or computationally to obtain high quality images. Physical blockage of these rings will only leave the thin beam core for imaging and is only useful for scanning applications, ergo not for OPT. Also, as the concentric rings will act as information carriers in the imaging process, a proper retroactive solution is preferred to use all available information. The characteristic energy distribution in Bessel beams makes for low peak intensities compared to focused con-

ventional Gaussian beams. In fact, the increased DoF offered by Bessel beams compared to that of Gaussian beams comes at the expense of power in the central core and the peak intensity [28] [27]. As with all non-diffracting beams, the self-healing properties of the Bessel beam may also provide increased imaging depth in turbid media [15]. This is under the condition that the self-healing properties of the beam do not cause a loss of usable information. The principle of regeneration is shown in Figure 3.3 for a Bessel beam. Figure 3.4 displays simulated and experimental images of the regeneration of a Bessel beam over its propagation after encountering an obstacle [2]. Note that the obstruction eventually results in the dark outer rings visible in Figure 3.4d and h.

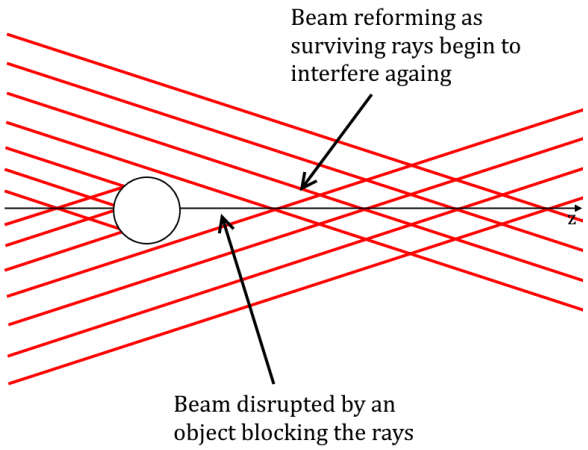

Figure 3.3: Self-regeneration of a Bessel beam (red rays) during propagation in z-direction. Source: [36].

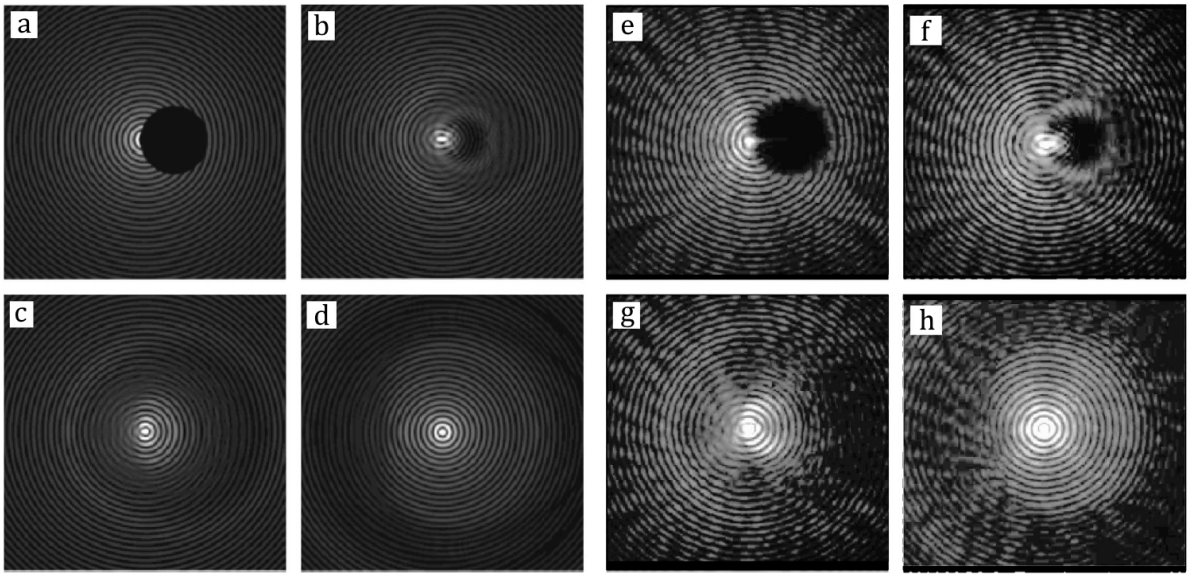

Figure 3.4: Self-regeneration of a Bessel beam, simulated (a, b, c, d) and experimental (e, f, g, h). The Bessel beam is created with an annular aperture and a lens with f = 35 cm and wavelength λ = 633 nm. The beam has a centre core radius of 40 µm. (a, e) initial condition, (b, f) at 8 cm from the obstacle, (d, g) at 30 cm from the obstacle, and (d, h) at 45 cm from the obstacle. Source: [2].

3.3. Generation of Bessel Beams

There are different ways to construct non-diffracting beams, all of them based on wave interference. The principle methods used to realize non-diffracting beams are the use of masks, spatial light modulation and lenses such as axicon lenses.

3.3.1. Masks

A basic way of creating interference from wavefronts is the use of a mask. In the earliest experiments with conical beams, a circular slit has been used to create a light cone with an interference pattern corresponding to that of a Bessel beam [29]. In the first experimental investigation of non-diffracting beams a lens was added [14]. Figure 3.5a shows the interference pattern created by the circular slit and the resulting Bessel profile diffraction patterns which make up a line focus. Figure 3.5b shows the slit, placed in the focal plane of a lens.

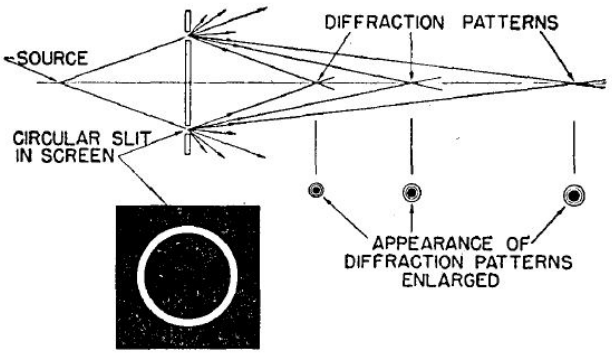

(a) Circular slit interference pattern. Source: [29].

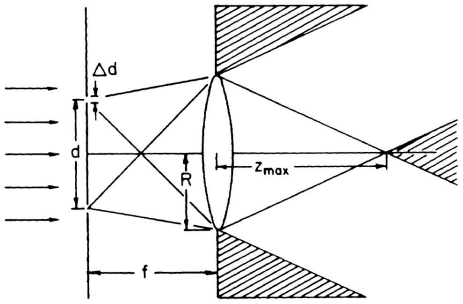

(b) Slit and lens combination with slit diameter d, output aperture radius R, range of uniform intensity distribution Z_{max} and shadow regions. Source: [14]

Figure 3.5: Bessel beam generation with mask

The use of a slit is relatively simple and intuitive, however only a small portion of the light used to illuminate the slit is not blocked and used to form the beam. This results in a beam with a relatively low intensity. This is undesirable as Bessel beams already show low intensity. In fact, for the Bessel beam an N-fold gain in focal depth involves precisely an N-fold loss of intensity [47].

Forms of phase masks are still used for all kinds of applications to this day, such as the extension of the DoF with a binary phase spatial filter in an optical probe for endoscopy [49] and application of binary phase spatial filters in optical coherence microscopy [26]. Also, a symmetric binary pupil filter has been optimized and used to maximize the extension of a two-dimensional light sheet formed by a cylindrical lens in Light Sheet Microscopy (LSM) [48]. In LSM a thin sheet of light is used to illuminate a thin slice of a sample and selectively perform emission based microscopy. In this research an optimization that minimizes the root mean square deviation from the maximum focal intensity was used to design simple and relatively cheap filters with a long flat focus and a wide DoF. Figure 3.6 shows the phase filter and the LSM configuration.

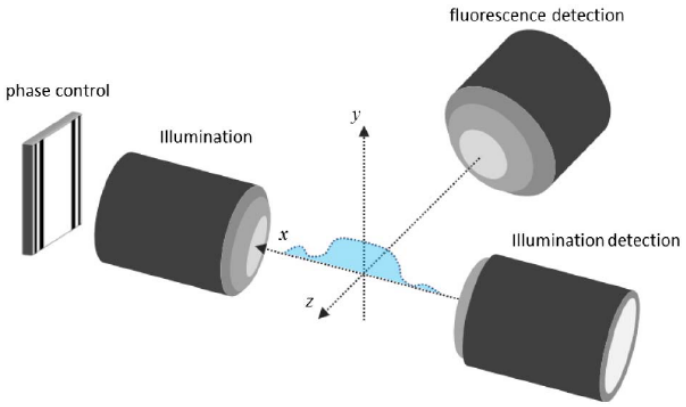

Figure 3.6: Axes configuration in the focal plane for Light Sheet Microscopy with an extended light sheet. The light enters from the left via the phase element and is focused along the xy-plane. Source: [48].

3.3.2. Spatial Light Modulation

Spatial Light Modulators, or SLM's, are devices that are used to spatially modulate the amplitude and phase of an optical wavefront in two dimensions. SLM's can be programmed to produce light beams with optical wavefronts using numerically defined phase elements, essentially replacing real phase masks. Figure 3.7a shows a 2D binary phase pattern to modulate a Gaussian beam to optically reconstruct a Bessel beam, shown in Figure 3.7b.

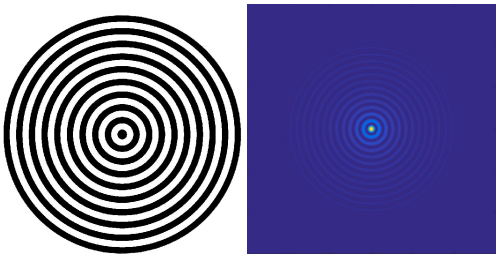

(a) Binary Bessel phase pattern.

(b) Resulting Bessel profile after some propagation .

Figure 3.7: Simulation results of binary Bessel phase pattern and corresponding beam.

SLM's use liquid crystals. The optical properties of the liquid crystals are modified by means of an electric field. This technique makes SLM's rather complex and expensive devices compared to masks and lenses.

3.3.3. Axicon Lenses

Axicon lenses are cylindrically symmetric glass cones which create interference patterns similar to the circular slits in Section 3.3.1. However, axicon lenses do not block any light, resulting in larger regions of interference with higher intensities. The term axicon was first coined by McLeod in 1954 [29]. The name 'axicon' means axis image, and has been chosen because a 'line image' is created. All conical, rounded cones and similar lenses which create line images, or more accurately put, a range of uniform intensity distribution over a line, are called axicons. The interference patterns created by circular slits are often also referred to as axicons. In this section we focus on the properties of the glass cone lens.

Axicon Lens Image Formation

Figure 3.8 shows the interference pattern created by an axicon lens illuminated by a Gaussian beam, with the intensity profile of the interference pattern indicated on the right hand side. The intensity profile in the depth of focus region is Bessel-like with a narrow high intensity beam centre core which is responsible for an extended DoF combined with a relatively high resolution. Note that the range of uniform intensity distribution z_{max}, denoted by DoF in the figure, is twice as long as the mask generated Z_{max} in Figure 3.5b. As mentioned in Section 3.2 the DoF extension comes at a price as the peak intensity of the Bessel profile is lower than that of a Gaussian beam with a similar beam core radius due to its characteristic energy distribution.

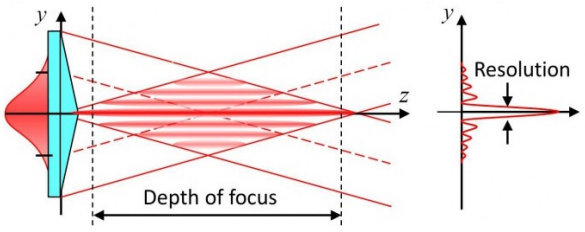

Figure 3.8: Axicon set-up for image formation.
Adaptation of: *http://obel.ee.uwa.edu.au/research/techniques/beam-shaping/*

Axicon lenses have already been used in several imaging techniques. In the field of OCT a custom-made micro-optic axicon has been used to perform endoscopic OCT with a measured invariant resolution of 8 μm across a 4 mm measured DOF [25]. In other work arrangements of multiple convex and concave axicons were used to create an endoscopic device that has a considerably shorter optical system length than conventional

systems [46]. Also, annular masks and an axicon have been used in LSM to generate scanned light sheets from Bessel beams [32]. Bessel beams have also been used in Optical Coherence Microscopy for in-vivo imaging of the global mouse brain ischemia, a restriction in blood supply causing an oxygen shortage [34]. An axicon lens was used to produce the Bessel beam and an annular aperture was added to block residual rays. A beam core width of smaller than 2.2 µm along a path of 800 µm was achieved.

Axicon Lens Light Collection

Axicons are often used for the generation of Bessel beams from Gaussian incident beams. The question remains whether the axicon can also be used for the collection of other light sources. Research on axicon lens light collection has been performed with bright reflective light sources [35] [50] [51]. Here, the axicon is illuminated in the same orientation as it is for transmission purposes as shown in Figure 3.9a with the addition of an objective lens. In Section 4.2.3 light collection with the axicon in this set-up is considered in more detail. The axicon can also be set-up reversed, so that the tip faces the isotropic light source, as shown in Figure 3.9b.

(a) Axicon set-up for light collection. **(b)** Reversed axicon set-up for light collection

Figure 3.9: Axicon set-ups for light collection.
Adaptation of: *http://obel.ee.uwa.edu.au/research/techniques/beam-shaping/*

Not many examples can be found on the use of axicons for the collection of light in this manner in the literature. In one case, a reversed axicon coupled to a spatial filter is used [22]. It is shown that an axicon coupled to a spatial filter can provide the distribution of incoherent emission as a function of depth while the spatial filter is used to restrict the collected emission to the optical axis. This set-up can only be used for scanning systems. In another research axicons are used to make up a cone illumination and detection configuration to construct a probe for depth-sensitive fluorescence measurements in turbid media [30]. Two axicons are used to form ring-shaped excitation light and the third axicon lens turns this into cone illumination of the sample and is used to collect the fluorescence emitted light. It is experimentally demonstrated that this cone shell configuration detects fluorescence with a higher sensitivity. The same researchers proposed a similar system with a more complex fibre bundle with five rings of collection fibers, each located a different radial distance away from the centre. The fibre bundle can obtain multiple fluorescence spectra corresponding to a range of successive targeted depths simultaneously [31].

3.3.4. Preferred Bessel Beam Generation

Non-diffracting Bessel beams show potential to increase the DoF in OPT thanks to some of their characteristic properties such as an extended range of uniform intensity distribution, making them superior to the Gaussian beam and its inherent limitations in some respects. However, their peak intensities are lower and it is unsure whether their self-reconstructing properties are beneficial to DoF extension. Bessel beams with a finite range of uniform intensity distribution can be constructed from conventional beams such as the Gaussian beam without loss of energy with axicon lenses. For these reasons the application of axicon lens generated Bessel beams in OPT is chosen for further research.

4

Axicon generated Bessel Beams

In this chapter the properties of Bessel beams generated by axicon lenses are explored. The Bessel beam is compared to the Gaussian beam and its characteristics are described quantitatively.

4.1. Mathematical Description

Figure 4.1 shows the formation of a Bessel beam by an axicon illuminated by a flat wavefront with a Gaussian intensity profile. This beam has a finite range of uniform intensity distribution, as opposed to the ideal theoretical strictly non-diffracting Bessel beam described earlier. The dimensions of the Bessel beam formed by a thin axicon are determined by the axicon refractive index n and its base angle α. The corresponding axicon conical angle β yields:

$$\beta = \arcsin\left(\frac{n}{n_0}\cos\left(\frac{1}{2}\pi - \alpha\right)\right) - \alpha. \tag{4.1}$$

With these axicon parameters the intensity distribution of an axicon generated Bessel beam can be described as a function of the radial distance from the beam centre ρ and the propagation distance z [7]:

$$I(\rho, z) = \frac{4Pk\sin\beta}{\omega_0}\frac{z}{z_{max}}J_0^2(k\rho\sin\beta)\exp\left(-\frac{2z^2}{z_{max}^2}\right), \tag{4.2}$$

where J_0 is the zero order Bessel function, ω_0 is the half width of the incident Gaussian beam, P is the total power of the incident Gaussian beam and the range of uniform intensity distribution is defined as $z_{max} = \omega_0\cos\beta/\sin\beta$. Diffraction effects from the outer edges of the axicon are ignored as effects on near-field irradiance patterns are negligible when the aperture radius is at least twice the Gaussian illumination spot radius [8].

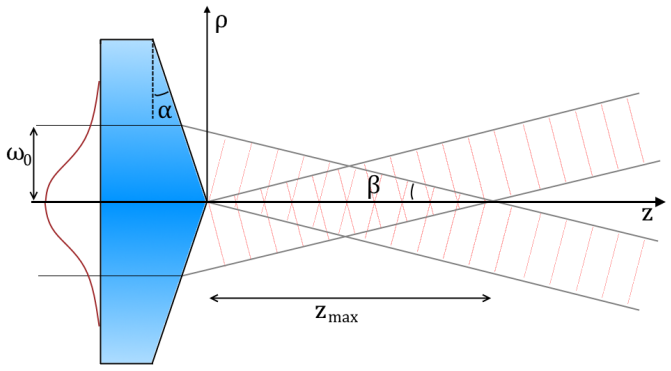

Figure 4.1: Formation of a Bessel beam by an axicon illuminated by a flat wavefront with a Gaussian intensity with beam waist ω_0, axicon base angle α, conical angle β and range of uniform intensity distribution z_{max}.

4.2. Intensity Distribution

Usable parameters for OPT are chosen to characterize the mathematical description of an exemplary Bessel beam. Figure 4.2 shows a visualization of the intensity distribution of an axicon generated Bessel beam with $\alpha = 20°$ and $n = 1.45$. With a Gaussian incident beam of $\omega = 1$ cm and a wavelength of 550 nm the resulting range of uniform intensity distribution $z_{max} = 5.8$ cm. The radius of the high intensity core ρ_0 can be found by determining the first zero of the Bessel function $J_0(k \sin\beta\rho_0) = 0$ [10]. Hence, the centre core radius can be described as $\rho_0 = 2.4048/(k \sin\beta)$, with 2.4048 being the first zero for a normalised zero-order Bessel function. For this example $\rho_0 = 1.26$ µm.

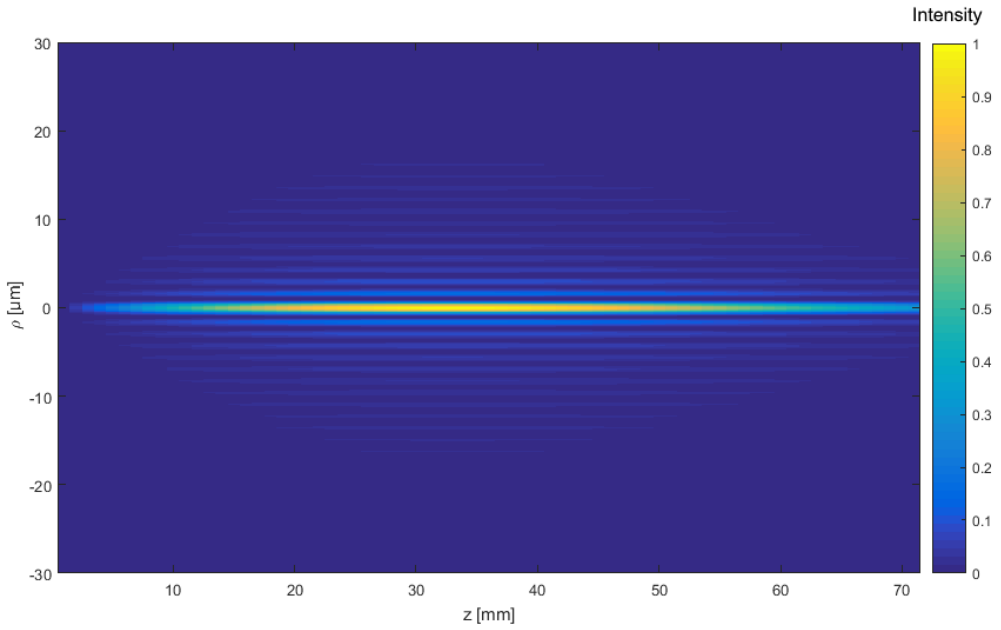

Figure 4.2: Normalised intensity distribution of an axicon generated Bessel beam with beam waist $\omega_0 = 1$ cm, wavelength $\lambda = 550$ nm, axicon base angle $\alpha = 20°$, conical angle $\beta = 10°$ and the range of uniform intensity distribution $z_{max} = 5.8$ cm .

The peak intensity of the example shown in Figure 4.2 occurs at $z = 2.9$ cm, halfway of z_{max}. The lateral intensity distribution at this point is shown in Figure 4.3a. The centre high intensity core can be seen with many side lobes which make up the concentric rings seen earlier in Figure 3.1b. Note that both figures display regions of the beam and more unpictured side lobes exist. The most inner ring, closest to the beam core, has a peak intensity of a factor 0.16 of the peak intensity of the centre core. The next ring peaks at a factor 0.09 and the rest of the rings follow at a gradual inhibited decrease. These proportions are typical for all lateral distributions within z_{max}. The transversal paraxial intensity distribution, meaning in the centre of the beam in the propagation plane, is shown in Figure 4.3b.

Round-tipped Axicons

The distribution in Figure 4.3b is a typical distribution for a perfect axicon, that is, an axicon with an infinitely sharp angled tip. Transversal intensity curves are more oscillatory for imperfect or more round-tipped axicons. Round tips of axicons have been modelled as a hyperboloid of revolution of two sheets as shown in Figure 4.4 [7]. The parameters a and b are then used to describe the electric field at $z = 0$ m:

$$E(\rho,0) = E_0 \exp\left(-\frac{\rho^2}{\omega_0^2}\right) \exp(ikn\Delta_0) \exp\left[ik(n_0 - n)\sqrt{a^2 + \frac{\rho^2}{\tan^2(\tau/2)}}\right] \tag{4.3}$$

where Δ_0 is the maximum thickness of the axicon on its axis and $\tau = \pi - 2\alpha$ rad.

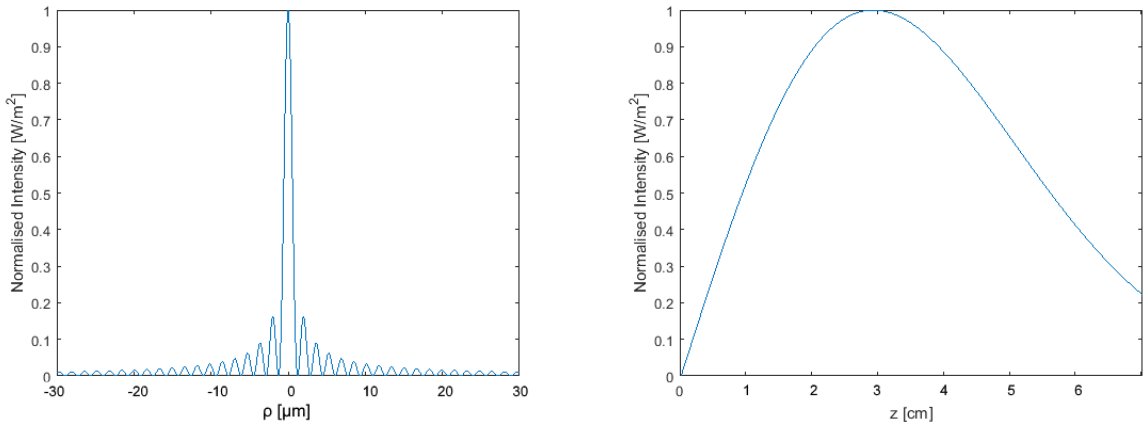

(a) Lateral intensity distribution at $z = 2.9$ cm.

(b) Transversal paraxial intensity distribution.

Figure 4.3: Intensity distributions of an axicon generated Bessel beam. The intensity is normalised.

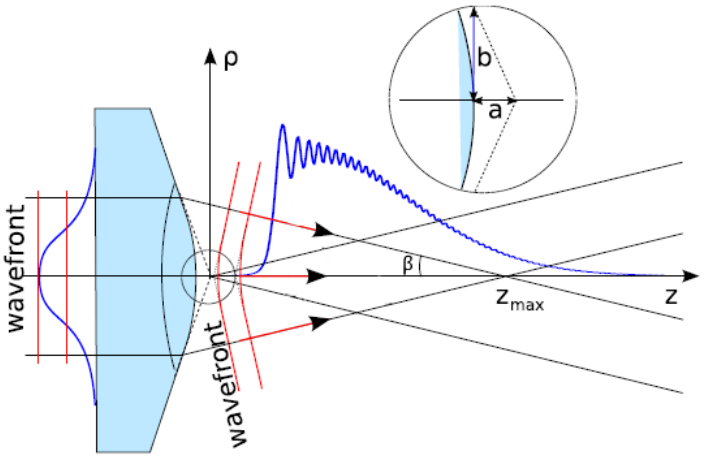

Figure 4.4: Round tips of axicons have been modelled as a hyperboloid of revolution of two sheets. Source: [7].

4.2.1. Resolution and DoF

For the given example of the perfect axicon generated Bessel beam the centre core radius is $\rho_0 = 1.26$ µm. In Figure 4.5 the intensity distribution is compared with that of a focused Gaussian beam described by Equation 2.1 with an in-focus half width equal to ρ_0. The focused beam over the same distance is hardly noticeable in 4.5b. In this case the Rayleigh range, discussed in Section 2.2 is $Z_R = 9$ µm. It is obvious that for these parameters a Gaussian beam would have an extremely small DoF, unusable for OPT. This tells us that if the axicon generated Bessel beam is applicable in OPT (sufficient image contrast is reached and reconstruction is possible), multiple micrometer resolution is possible over a multiple centimetre DoF.

4.2.2. DoF and Peak Intensity Trade-off

As mentioned, the image contrast is of concern with Bessel beams as they yield a lower peak intensity than Gaussian beams due to their energy distribution. The extended Bessel beam DoF comes at the cost of intensity. In fact, an X-fold increase in DoF must result in an X-fold loss of peak intensity. A Fresnel number defined as $N = \omega\beta/\lambda$ can be a describing parameter of the trade-off between DoF and peak intensity for an axicon with a Gaussian incident beam [27]. For $N < 10$, over 10% of the total beam power is carried by the central lobe and the percentage increases rapidly as N decreases. However, a balance has to be found as z_{max} and N are dependent and a workable DoF in the form of z_{max} is needed.

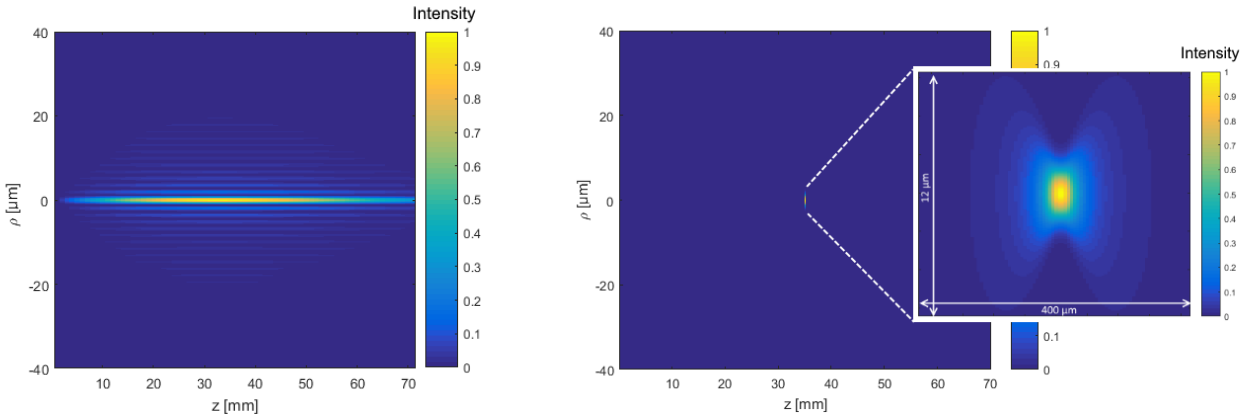

(a) Normalised intensity distribution of an axicon generated Bessel beam with centre beam core $\rho_0 = 1.26$ µm at $\frac{1}{2} z_{max}$.

(b) Normalised intensity distribution of a focused Gaussian beam with $\omega_0 = 1.26$ µm.

Figure 4.5: Comparison of intensity distributions of an axicon generated Bessel beam and a Gaussian beam with identical beam core radii in focus. $\lambda = 550$ nm, axicon base angle $\alpha = 20$ °. The colorbar denotes normalized intensity.

Uniformity shaping

Although axicon generated Bessel beams have an approximately uniform axial intensity distribution, especially compared to Gaussian beams, one can see above the distribution is not strictly uniform and even oscillatory for round-tipped axicons. An effort has been made to create Bessel beams with a uniform axial intensity [20]. The suggested technique compensates for the linearly growing axial intensity profile of a sharp-edged axicon by introducing 1/r illumination of the axicon in a theoretical study. A significant improvement of the axial intensity uniformity is reached but wave-propagation simulations indicated residual oscillations. An analytic approach to suppress these oscillations has been proposed but experimental realization of these shaped beams has not been performed as it requires 'highly precise complex modulation of the field as well as aberration free optical pathway' [11].

Oblique illumination

Oblique illumination of axicons has been researched extensively. A full theoretical and experimental study of the diffraction patterns presented by oblique illumination has resulted in a well-describing analytic description of patterns versus illumination angle and distance [6]. Some results of this study are shown in Figure 4.6, where $M = kz\frac{(n-1)^2\alpha^2 \sin\eta}{4}$ is used to arrange results as diffraction patterns denoted by M can be the same for different combinations of illumination angle η and distance z. Again, α denotes the axicon angle, k denotes the wave number and n denotes the axicons refractive index. As one would expect the main conclusion is that 'the diffraction pattern becomes more complicated along with the increase in the oblique angle and the distance from the axicon'.

4.2.3. Light Collection with an Axicon

The Bessel beam shown until now is generated by the illumination of an axicon with a beam with a Gaussian intensity profile. For OPT we would like the axicon lens to collect undirected light from (point) sources. In the case of light collection by illumination of the axicon lens it has been found that the intensity distributions in the illuminated region with plane, converging or diverging monochromatic waves all have the form of the zero-order Bessel function [50]. For polychromatic light the superposition of the intensities in individual monochromatic patterns make up the intensity patterns. The same study provides analysis of fields generated by an axicon with an objective lens illuminated by a plane wave, a converging wave and a diverging wave. The same set-up and field analysis has been used in another study to demonstrate the axicons insensitivity to misfocusing, i.e. extended DoF, with a light collecting axicon both in simulation and experiments [51]. The text on a computer chip was illuminated by an incoherent light source in the form of a white LED and measurements were made in the paraxial distance. The results were evaluated qualitatively. It was found that the axicon degrades the original image quality of the optical system, but helps to make the system less sensitive to defocus. The obtained images were post-processed with a Wiener filter to increase the quality.

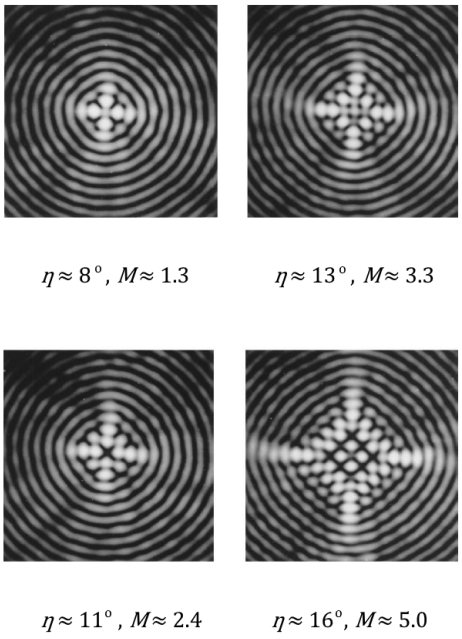

Figure 4.6: Experimental results of oblique illumination at angle η and distance $z = 3000$ mm. Source: [6].

Also, a text on paper was imaged. An example of the results is depicted in Figure 4.7. These studies were performed with bright, incoherent illumination of objects. Experiments with objects illuminated with coherent light or collection of emitted light with an un-apertured axicon are yet to be performed.

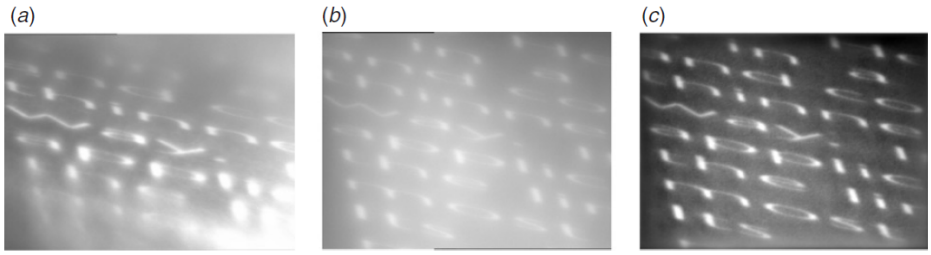

Figure 4.7: *(a)* Images captured by the optics system without the axicon (Gaussian). *(b)* Images captured by the optics system with the axicon. *(c)* Restoration result of *(b)* with Wiener filter. Source: [51].

Axicon with Objective Lens Model

For light collection we discuss the combination of an axicon and an objective lens. The axicon with objective lens model from the literature described above is used [50]. This model uses the diffraction pattern of an axicon to analyse fields generated by an axicon with an objective lens illuminated by different waveforms. A brief overview of the equations used in the model can be found in Appendix C. Figure 4.8 displays the three situations distinguished by the model; the set-up illuminated by a diverging wave, a plane wave and a converging wave, each corresponding to a range of point source distance from the objective lens.

The model has been analysed for different paraxial point source positions for three different situations; illumination with coherent light corresponding to a laser ($\lambda = 515$ nm), illumination with incoherent light corresponding to an LED ($\lambda = 350$-400 nm with steps of 5 nm) and illumination with extremely incoherent light ($\lambda = 350$-950 nm with steps of 60 nm). The objective lens focal length is chosen at $f = 2.5$ cm, and the distance between the objective and the axicon is chosen at $s = 1$ cm, resulting in a theoretical DoF of 4 cm [50]. Analysis of the field descriptions obtained with these parameters is shown in Figure 4.9. For each of the three situations two graphs are shown, the left graph depicts the intensity distribution for a point source 2.75 cm (arbitrarily chosen) removed from the objective lens and the right graph depicts the centre core FWHM for different point source positions on the paraxial axis.

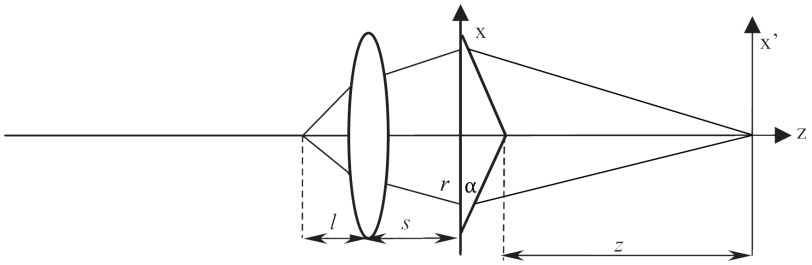

(a) Axicon illuminated by a diverging wave, $l < f$.

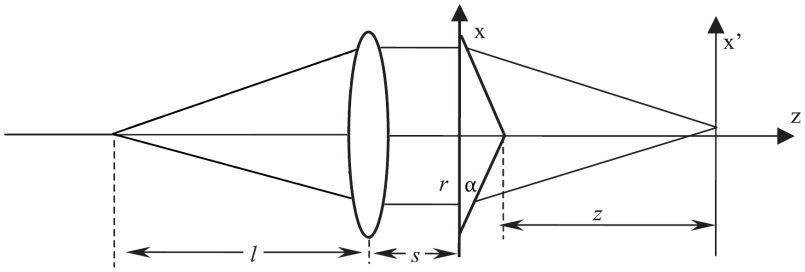

(b) Axicon illuminated by a plane wave, $l = f$.

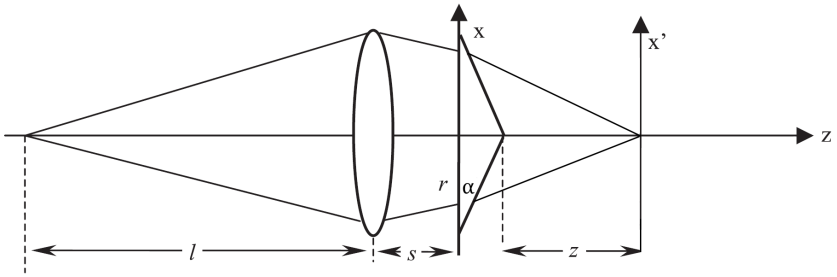

(c) Axicon illuminated by a converging wave, $l > f$.

Figure 4.8: Axicon with objective. l is the object distance, f is the objective lens focal length, s is the distance between the objective and the axicon, z is the distance between the axicon and the image plane and α is the axicon base angle. Source: adaptation of [50].

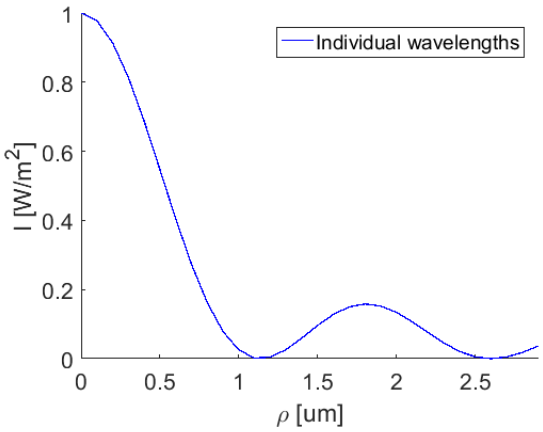

(a) Normalized intensity distribution for a coherent point source 2.75 cm removed from the objective lens; $\lambda = 515$ nm

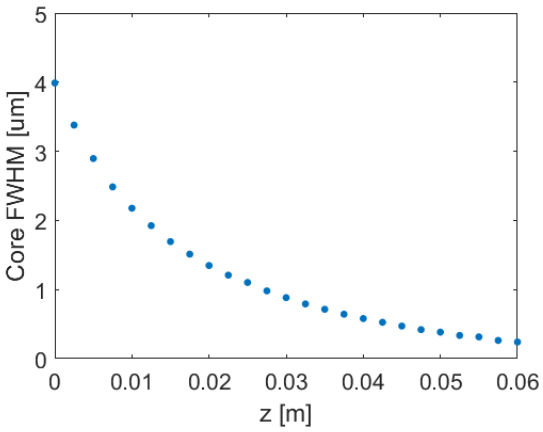

(b) Intensity distribution centre core FWHM for a coherent point source over the paraxial axis.

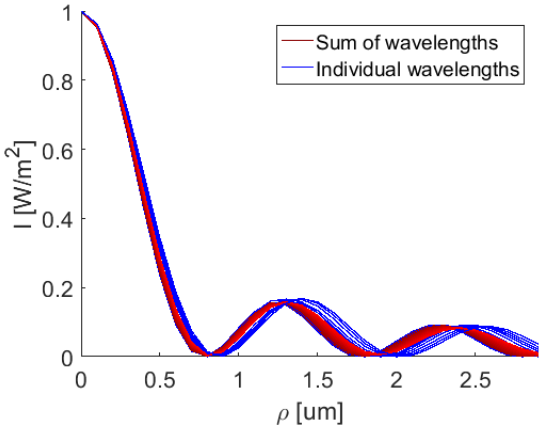

(c) Normalized intensity distribution for an incoherent point source 2.75 cm removed from the objective lens; $\lambda = 350 - 400$ nm with steps of 5 nm.

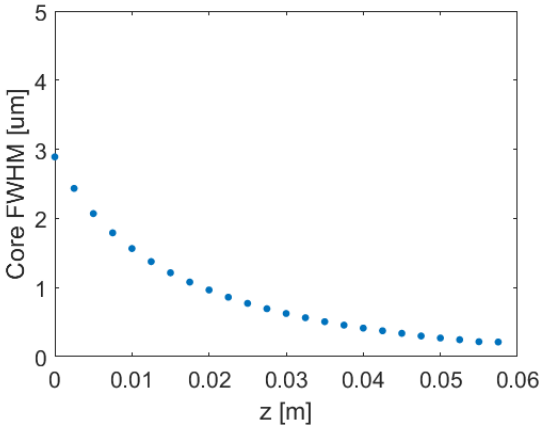

(d) Intensity distribution centre core FWHM for an incoherent point source over the paraxial axis.

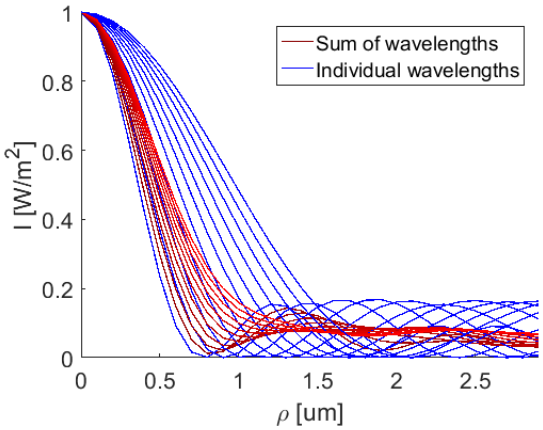

(e) Normalized intensity distribution for an extremely incoherent point source 2.75 cm removed from the objective lens; $\lambda = 350 - 950$ nm with steps of 60 nm.

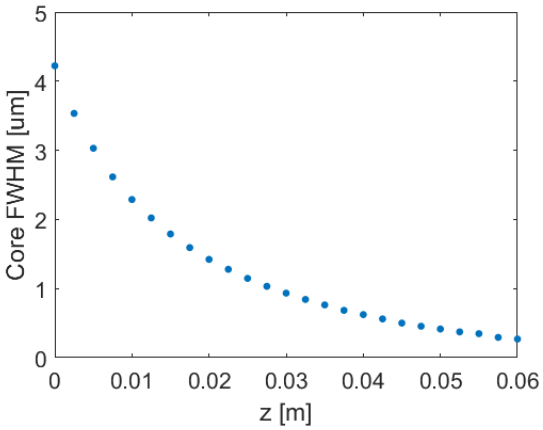

(f) Intensity distribution centre core FWHM for an extremely incoherent point source over the paraxial axis.

Figure 4.9: Normalized intensity distributions for a point source 2.75 cm removed from the objective lens and centre core FWHM's over the paraxial axis. In 4.9a , 4.9c and 4.9e the blue intensity distributions depict the individual wavelengths and the red distributions depict the increasing superpositions as the individual wavelengths are taken into account one by one. The first superposition is dark red and evolves to bright red, which is the superposition of all wavelengths.

The FWHM of the centre core of the intensity distribution decreases as the distance of the point source to the objective lens increases. Figure 4.8 illustrates that as the distance of a point source to the objective lens increases, the wave incident angle on the axicon increases and the axicon exit angle decreases (or the conical angle β, defined in the beginning of this chapter, increases). As a result the range of uniform intensity distribution z_{max} and the beam centre core radius ρ_0 decrease, corresponding to a smaller centre core FWHM. It can be seen that only for extremely incoherent light the vast difference in individual wavelengths adds up to a relatively large FWHM of the superposition. A single wavelength simulation for $\lambda = 375$ nm yielded near-identical results to the $\lambda = 350 - 400$ nm simulation. An increase in wavelength does result in larger FWHM values.

Overlapping Bessel Profiles

It would be useful to know what one can expect for objects that are not perfect point sources. Equation 4.2 is used to create multiple Bessel distributions that are made to overlap each other with spatial offset to simulate different object positions. Note that this is a very conceptual simulation, which merely serves to give a general idea of the intensity distribution for overlapping Bessel distributions. Eleven Bessel distributions with an intensity distribution equal to the superposition profile from Figure 4.9d are repeatedly laid over each other with spacing of 0.6 µm. This is repeated in the perpendicular direction for the row of 11 distributions with the same spacing, resulting in 11 x 11 Bessel distributions of which the summed intensity is shown in Figure 4.10a. This asymmetrical mishmash of distributions is created to illustrate what the profile of an axicon image of a larger structure might look like.

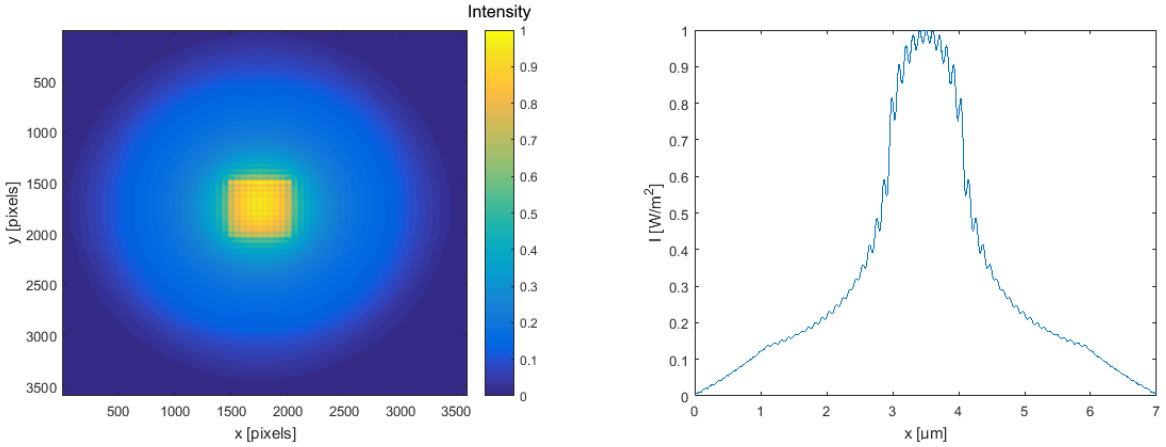

(a) Sum of 11 x 11 simulated Bessel intensity distributions, with 0.6 µm spacing.

(b) Simulated profile of the middle row of 4.10a.

Figure 4.10: 121 superpositioned Bessel profiles and a corresponding lateral profile. The colorbar denotes the normalised intensity.

Figure 4.10b shows the normalised intensity profile of the middle row of 4.10a. This distribution is relatively wide and shallow compared to the distribution of a single Bessel profile. Spikes in intensity are still present. The image shows that as more and more Bessel profiles are overlaid the image resolution decreases.

4.3. Propagation Simulation

Equation 4.2 describes the intensity distribution of an axicon generated Bessel beam. This description can be used to perform an OPT simulation. Before this is done, it is valuable to know whether this description is approximately similar to a realized axicon generated Bessel beam with finite energy, especially in range of the high intensity core and within the range of uniform intensity distribution z_{max}. To this end, a numerical propagation simulation is performed and the analytic description of the axicon generated Bessel beam is compared with this numerical simulation of a realized axicon generated Bessel beam. An axicon generated Bessel beam with an axicon angle $\alpha = 20°$, an incident Gaussian beam with $\omega_0 = 1$ cm and $\lambda = 550$ nm will yield a range of uniform intensity distribution $z_{max} = 5.8$ cm. To observe the full z_{max} range with a margin to observe the ceasing of the beam centre core a propagation distance of $z = 7$ cm is chosen.

4.3.1. Fresnel Propagation

A method commonly used for propagation simulation is the Fresnel diffraction propagation with a transfer function. For an initial field description U_1, U_2 is given by [44]

$$U_2(x,y) = \mathfrak{F}^{-1}\{\mathfrak{F}\{U_1(x,y)\}H(f_x,f_y)\}, \tag{4.4}$$

with transfer function H given by

$$H(f_x,f_y) = e^{jkz}\exp\left[-j\pi\lambda z\left(f_x^2,f_y^2\right)\right]. \tag{4.5}$$

Here, x and y denote the horizontal and vertical coordinates both perpendicular to the propagation direction, f_x and f_y are independent frequency variables associated with x and y, k is the wave number, λ is the wavelength, z is the propagation direction coordinate and $j = \sqrt{-1}$.

The axicon lens can be described as a thin lens transformation with a thickness function [17], generating an initial field:

$$U_1(x,y) = U_0\exp\left(\frac{i2\pi\tan(\alpha)\sqrt{x^2+y^2}\,(1-n)}{\lambda}\right), \tag{4.6}$$

where U_0 describes a Gaussian input field and n is the refractive index of the axicon.

Sampling criteria

A sampling regime for critical sampling for Fresnel Transfer Function Propagation is

$$\Delta x = \frac{\lambda z}{L}, \tag{4.7}$$

with lateral step size Δx and domain width L [44]. L must be at least equal to the width of the incident Gaussian beam, $2\omega_0 = 2$ cm, but is preferably larger to avoid edge artefacts. For the desired simulation $\Delta x =$ 1.925 µm. This means a sampling of at least $N = L/\Delta x = 10{,}390$ is required. This happens to be just about the limit of what a modern desktop computer can handle. Figure 4.11 shows the result for a Fresnel propagation simulation for these parameters.

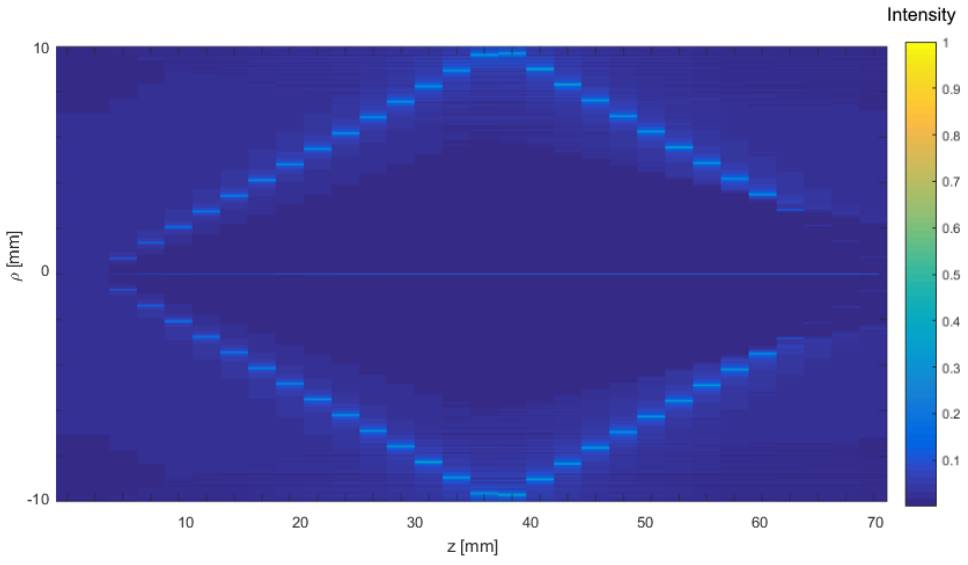

Figure 4.11: Simulation result of an axicon generated Bessel beam with Fresnel propagation. ω_0= 1 cm, λ = 550 nm and z = 7 cm, the colorbar indicates normalized intensity.

The result is clearly invalid. It does not resemble a Bessel beam and artefacts in the form of periodic copies are present in the intensity distribution. A criterion commonly used for determining when the Fresnel

expression can be applied is the Fresnel number $N_F = \frac{w^2}{\lambda z}$ with aperture half width w [44]. The criterium is not violated if $N_F \leq 1$, and the Fresnel expression can be applied. This is not the case for the propagation we wish to simulate, which violates the requirement by more than a factor $2 \cdot 10^3$. An alternative to Fresnel propagation is Fraunhofer propagation but the criterium for this type of propagation is defined as $N_F << 1$. Another alternative must be found.

4.3.2. Hankel Propagation Simulation

One way to relieve the required computational power for propagation simulation is by scaling down the dimensions of the problem. Cylinder symmetry assumption is valid for propagation of a Gaussian beam through an axicon lens. The Hankel transform can describe a circularly symmetric case of the Fourier transform. The relation between the Hankel transform and the Fourier transform is briefly explained in Appendix B. Now, instead of a planar field in x and y, only the radius ρ has to be calculated. The initial field described with the thin lens function now becomes

$$U_1(\rho) = U_0 \exp\left(\frac{i2\pi \tan(\alpha)\rho(1-n)}{\lambda}\right). \tag{4.8}$$

The propagation of this field is obtained using the free-space propagation method based on decomposition of the field in plane z = 0 into a spectrum of plane waves (spatial-frequency spectrum obtained by the Fourier transform). Using an algorithm from the literature which implements the Hankel Transform [10], with addition of the lens description (4.8) and minor code adaptations to optimise computer RAM/CPU usage, a propagation simulation can be performed.

Figure 4.12a shows the analytic description of the axicon generated Bessel beam as described in Equation 4.2 and Figure 4.12b shows the Hankel propagation simulation result. The results are very similar. The beam centre core of the analytic description is ρ = 1.24 µm and is slightly smaller than that of the propagation simulation which is found to be ρ = 1.4 µm. Both beams show a similar z_{max} of around 5.8 cm and both display their maximum intensity at 3.5 cm. The analytic description and the propagation simulation are found to be a match and the analytic description is deemed to be usable for an OPT simulation.

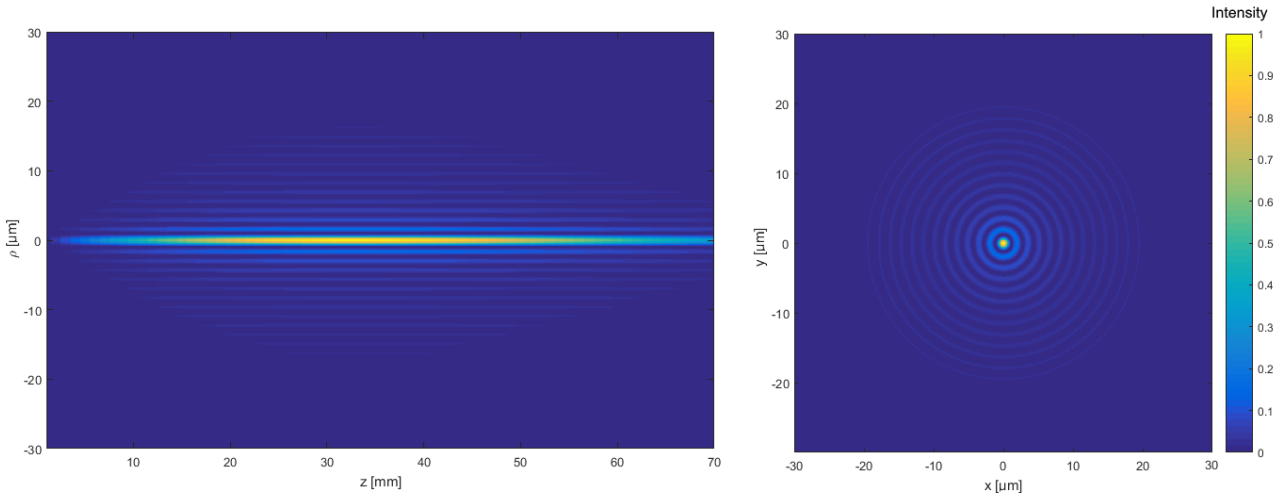

(a) Analytic description of an axicon generated Bessel beam along the optical axis (left) and the xy-plane with the maximum intensity at $z = 35$ mm (right).

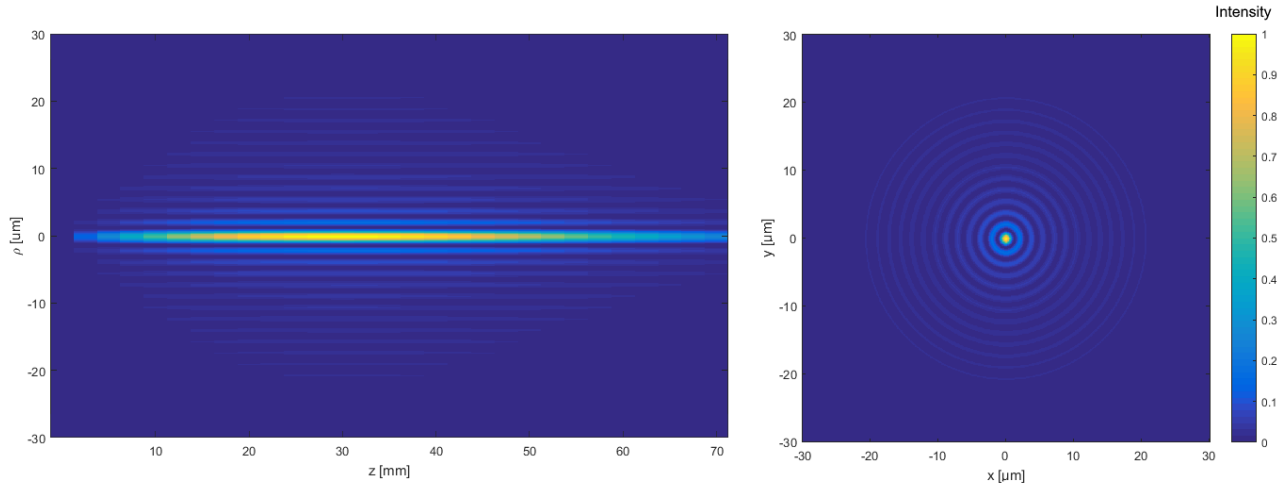

(b) Hankel propagation simulation of an axicon generated Bessel beam along the optical axis (left) and the xy-plane with the maximum intensity at $z = 35$ mm (right).

Figure 4.12: Analytic description **(a)** and propagation simulation **(b)** of an axicon generated Bessel beam. $\omega_0 = 1$ cm, $\lambda = 550$ nm and axicon base angle $\alpha = 20$ °. The colorbar denotes normalized intensity.

5

Optical Projection Tomography, Theory and Simulation

In the first section of this chapter a theoretical approach to OPT from the literature is presented. The description of the intensity distribution for an axicon generated Bessel beam in Equation 4.2 is then integrated into the OPT theory in order to establish a derivation for a description of the horizontal sections of the 2D projections in OPT with a Bessel imaging PSF. In the second section of this chapter the principles behind several computerized image reconstruction methods are discussed. In the last section OPT simulations of Gaussian and Bessel systems are presented and compared.

5.1. Theory

The Point Spread Function, or PSF, describes the response of an imaging system to a point source or point object. The degree of spreading or blurring of the point object is a measure for the quality of an imaging system and an indicator of the resolution of the system. It is quite literally the impulse response of an optical system. The PSF of the imaging system, where single projections are made, is directly related to the tomographic PSF, where a collection of projections acquired at different angles is considered. The Fourier optics description of the PSF of the imaging system can be used to derive the PSF of the tomography system.

An analysis has been performed by Van der Horst and Kalkman [43] for a tomographic PSF with an imaging PSF equal to a focused Gaussian beam. The following analysis, Section 5.1.1 and the first part of 5.1.2, is excerpted from this work. A new analysis for a Bessel PSF is presented in the second part of Section 5.1.2. The analysis is performed for fluorescence tomography but is equally valid for transmission tomography.

5.1.1. Image Formation

Let us consider an object with fluorescence distribution $f(t,s,z)$. Projections of the object are created because light emitted by the object is focused onto a 2D detector as depicted in Figure 5.1. The coherent PSF of the imaging system is denoted by $h(t,s,z)$. A 3D convolution of the object function $f(t,s,z)$ and this incoherent PSF of the imaging optics $|h(t,s,z)|^2$ describes the intensity in the image space:

$$p(t',s',z') = f(t,s,z) \circledast |h(t,s,z)|^2 \tag{5.1}$$

In conventional straight ray based tomography only a straight line from the source to the detector is sampled [24]. But in OPT the measured points sample a volume of the object described by the PSF $|h(t,s,z)|^2$. The system images the plane $s = 0$ in object space onto the plane $s' = 0$ in image space.

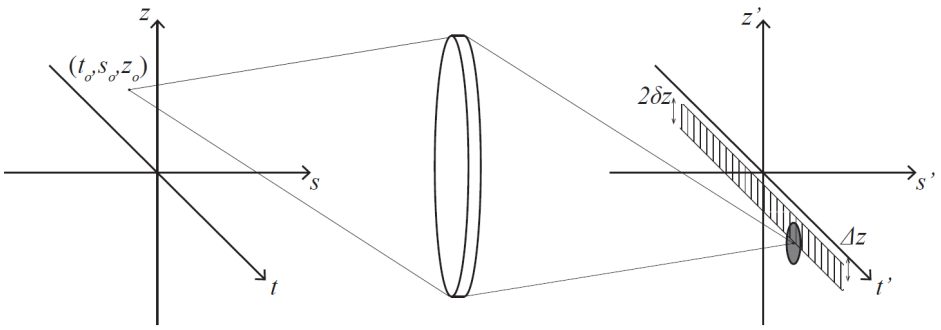

Figure 5.1: Schematic representation of a single point detection in fluorescent tomography. Source: [43].

5.1.2. Tomographic Point Spread Function

A top view of the object plane is shown in Figure 5.2a with point object (x_0, y_0). It is assumed from here on that the $z-$axis is the rotation axis which means the rotation axis is in the focal plane. Also, the detector is positioned in $s' = 0$. A projection p at angle θ can be described in the reference frame of the detector (t', s', z'). The relation between the object coordinates in the rotating frame (x, y, z) and the detector frame (t, s, z) can be described by:

$$\begin{bmatrix} t \\ s \\ z \end{bmatrix} = \begin{bmatrix} \cos(-\theta) & -\sin(-\theta) & 0 \\ \sin(-\theta) & \cos(-\theta) & 0 \\ 0 & 0 & 1 \end{bmatrix} \begin{bmatrix} x \\ y \\ z \end{bmatrix} \tag{5.2}$$

The response of the tomographic imaging system to a point object function reveals the resolution of the system: $f(x, y, z) = \delta(x - x_o, y - y_o, z - z_o) = \delta(t - t_o, s - s_o, z - z_o)$. Visually this is shown in Figure 5.2a, with an example of a projection $p(\theta, t)$. With the assumption that the point object is placed in the plane $z_o = 0$ the PSF becomes:

$$p(\theta, t', z') = |h(t' - t_o, -s_o, z')|^2 \tag{5.3}$$

All horizontal sections of the 2D projections correspond to one or multiple rows of detector pixels at the corresponding vertical position of the slice. With Δz being the vertical distance between the point source and the slice, and $2\delta z$ being the slice thickness one can write:

$$p(\theta, t') = \int_{\Delta-\delta z}^{\Delta+\delta z} |h(t' - t_o, s_o, z)|^2 dz \tag{5.4}$$

All 1D projections make up the sinogram. The Fourier transform of Equation 5.4 along transversal direction yields the frequency description of the projection:

$$P(\theta, f_t) = \mathfrak{F}\left\{ p(\theta, t') \right\} \tag{5.5}$$

The projection slice theorem states that under the assumption of a parallel-beam geometry the 2D Fourier transform of the image of the object, optical transfer function $OTF(f_x, f_y)$, is composed of the frequency content of the projections $P(\theta, f_t)$. Figure 5.2b shows that the radial cross-section of $OTF(f_x, f_y)$ is formed by each projection $P(\theta, f_t)$ at angle θ. The OTF can be calculated from Equation 5.5 with

$$s_o = s_o(\theta) = r_o \sin(\theta_o - \theta), \quad \theta = \tan^{-1}\left(\frac{f_y}{f_x}\right), \quad r_o^2 = x_o^2 + y_o^2 \quad \text{and } f_t = \sqrt{f_x^2 + f_y^2}. \tag{5.6}$$

The inverse Fourier transform of the OTF is the tomographic PSF. Following the steps described above, for a Gaussian imaging PSF the tomographic PSF as derived in [43] yields:

$$PSF(u, v) = \sqrt{\frac{1}{\pi^2 a_u a_v}} \exp\left(-\left[\frac{u^2}{a_u} + \frac{v^2}{a_v} \right] \right) \tag{5.7}$$

with $a_u = \omega_0^2/2$, $a_v = \left(\omega^2(r_o)/2\right)$ and

$$\begin{bmatrix} u \\ v \end{bmatrix} = \begin{bmatrix} \cos(-\theta_o) & -\sin(-\theta_o) \\ \sin(-\theta_o) & \cos(-\theta_o) \end{bmatrix} \begin{bmatrix} x - x_o \\ y - y_o \end{bmatrix}. \tag{5.8}$$

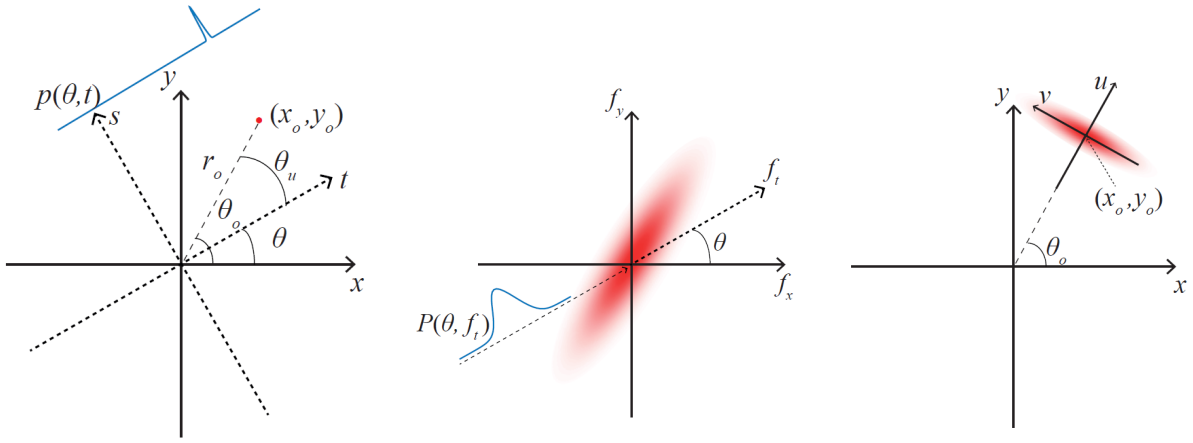

(a) Top view of the point object (x_0, y_0) in the object and camera frames of reference.

(b) Frequency domain representation of the reconstructed image for a point object. The frequency content of a single projection is indicated at angle θ.

(c) Reconstructed image of a point object.

Figure 5.2: Source: [43].

Bessel PSF

In Chapter 4 an analytic description of a theoretical axicon generated Bessel beam was introduced from literature. Equation 4.2 allows for the derivation of the PSF of the tomographic imaging system for OPT with an imaging PSF defined by an axicon generated Bessel beam in a similar manner as the derivation for the tomographic PSF with a Gaussian imaging PSF performed by Van der Horst and Kalkman.

The imaging PSF is assumed to be a focused axicon generated Bessel beam. As Bessel beams have a large range of uniform intensity distribution the area of focus can be quite large. We consider the focus to be at the point with the highest intensity on this range, which is at $\frac{1}{2}z_{max}$ for a Gaussian incident beam as mentioned in Chapter 4. Equation 4.2 is used to express the imaging PSF:

$$|h(t,s,z)|^2 = \frac{4Pk\sin\beta}{\omega_0}\frac{s+\frac{1}{2}s_{max}}{s_{max}}J_0^2(k\sqrt{t^2+z^2}\sin\beta)\exp\left(-\frac{2(s+\frac{1}{2}s_{max})^2}{s_{max}^2}\right), \tag{5.9}$$

Note that the previously denoted z coordinate and the constant z_{max} in Equation 4.2 are denoted here as s and s_{max} for the sake of consistency. Also, the earlier radial description ρ is now replaced by $\sqrt{t^2+z^2}$ since we have parted from cylindrical coordinates.

A description of the horizontal sections of the 2D projections can be obtained from the imaging PSF, which can be described with Equation 5.9 after the substitution into Equation 5.3 and integration over the height of the detector row with Equation 5.4.

Substition of Equation 5.9 into Equation 5.3 and Equation 5.4 yields:

$$p(\theta,t') = \frac{4Pk\sin\beta}{\omega_0}\frac{s_0+\frac{1}{2}s_{max}}{s_{max}}\exp\left(-\frac{2(s_0+\frac{1}{2}s_{max})^2}{s_{max}^2}\right)\int_{\Delta z-\delta z}^{\Delta z+\delta z}J_0^2(k\sin\beta\sqrt{(t'-t_0)^2+z^2})dz \tag{5.10}$$

What follows is an extensive stepwise derivation leading to an expression for $p(\theta,t')$ after integration over z. The integration variable z is only present in the squared zeroth order Bessel function term. The zeroth order Bessel function can be expressed as

$$J_0(x) = \sum_{n=0}^{\infty}\frac{(-1)^n}{(n!)^2}\left(\frac{x}{2}\right)^{2n}, \tag{5.11}$$

and its square can be written as

$$J_0^2(x) = \sum_{n=0}^{\infty}\left(\sum_{m=0}^{\infty}\frac{(-1)^{n+m}}{(n!)^2(m!)^2}\left(\frac{x}{2}\right)^{2(n+m)}\right) \tag{5.12}$$

and with $q = n+m$ and $l = n$, the first term is reorganized

$$J_0^2(x) = \sum_{q=0}^{\infty}\underbrace{\sum_{l=0}^{q}\frac{(-1)^q}{(l!)^2\left((q-l)!\right)^2}}\left(\frac{x}{2}\right)^{2q} \tag{5.13}$$

$$\frac{1}{(q!)^2}\sum_{l=0}^{q}\frac{(q!)^2}{(l!)^2\left((q-l)!\right)^2} = \frac{1}{(q!)^2}\sum_{l=0}^{q}\binom{q}{l}^2 \tag{5.14}$$

5.14 can be rewritten as

$$\frac{1}{(q!)^2}\binom{2q}{q} \tag{5.15}$$

and substituted in 5.13

$$J_0^2(x) = \sum_{q=0}^{\infty}\frac{(-1)^q}{(q!)^2}\binom{2q}{q}\left(\frac{x}{2}\right)^{2q}. \tag{5.16}$$

Relating back to 5.10, let us write the quadratic Bessel term as

$$J_0^2\left(\gamma\sqrt{z^2+(t'-t_0)^2}\right) \tag{5.17}$$

with $\gamma = k\sin\beta$, and let us write the other terms as

$$A = \frac{4Pk\sin\beta}{\omega_0}\frac{s_0+\frac{1}{2}s_{max}}{s_{max}} \quad \text{and} \quad B = \exp\left(-\frac{2(s_0+\frac{1}{2}s_{max})^2}{s_{max}^2}\right)$$

So that 5.10 becomes

$$p(\theta,t') = AB\int_{\Delta z-\delta z}^{\Delta z+\delta z} J_0^2\left(\gamma\sqrt{z^2+(t'-t_0)^2}\right)dz. \tag{5.18}$$

Writing the Bessel term as in 5.16,

$$J_0^2\left(\gamma\sqrt{z^2+(t'-t_0)^2}\right) = \sum_{q=0}^{\infty}\frac{(-1)^q}{(q!)^2}\binom{2q}{q}\left(\frac{\gamma\sqrt{z^2+(t'-t_0)^2}}{2}\right)^{2q} \tag{5.19}$$

$$= \sum_{q=0}^{\infty}\frac{(-1)^q\gamma^{2q}}{(q!)^2 4^q}\binom{2q}{q}\left(z^2+(t'-t_0)^2\right)^q, \tag{5.20}$$

allows for an integration of the Bessel term

$$\int_{\Delta z-\delta z}^{\Delta z+\delta z} J_0^2\left(\gamma\sqrt{z^2+(t'-t_0)^2}\right)dz = \sum_{q=0}^{\infty}\frac{(-1)^q\gamma^{2q}}{(q!)^2 4^q}\binom{2q}{q}\int_{\Delta z-\delta z}^{\Delta z+\delta z}\left(z^2+(t'-t_0)^2\right)^q dz. \tag{5.21}$$

The last part can be rewritten

$$\int_{\Delta z-\delta z}^{\Delta z+\delta z}\left(z^2+(t'-t_0)^2\right)^q dz = \int_{\Delta z-\delta z}^{\Delta z+\delta z}\sum_{i=0}^{q}\binom{q}{i}z^{2(q-i)}(t'-t_0)^{2i}dz \tag{5.22}$$

$$= \sum_{i=0}^{q}\binom{q}{i}(t'-t_0)^{2i}\int_{\Delta z-\delta z}^{\Delta z+\delta z} z^{2(q-i)}dz \tag{5.23}$$

$$= \sum_{i=0}^{q}\binom{q}{i}(t'-t_0)^{2i}\frac{1}{2(q-i)+1}z^{2(q-i)+1}\Big|_{\Delta z-\delta z}^{\Delta z+\delta z} \tag{5.24}$$

$$= \sum_{i=0}^{q}\binom{q}{i}\frac{(t'-t_0)^{2i}\left((\Delta z+\delta z)^{2(q-i)+1}-(\Delta z-\delta z)^{2(q-i)+1}\right)}{2(q-i)+1} \tag{5.25}$$

Which, recapping to 5.18, reveals the full integral that gives a description of the horizontal sections of the 2D projections in OPT with a Bessel imaging PSF

$$p(\theta,t') = AB\int_{\Delta z-\delta z}^{\Delta z+\delta z} J_0^2\left(\gamma\sqrt{z^2+(t'-t_0)^2}\right)dz$$

$$= AB\sum_{q=0}^{\infty}\binom{2q}{q}\frac{(-1)^q\gamma^{2q}}{(q!)^2 4^q}\sum_{i=0}^{q}\binom{q}{i}\frac{(t'-t_0)^{2i}\left((\Delta z+\delta z)^{2(q-i)+1}-(\Delta z-\delta z)^{2(q-i)+1}\right)}{2(q-i)+1} \tag{5.26}$$

with

$$\gamma = k\sin\beta,\quad A = \frac{4Pk\sin\beta}{\omega_0}\frac{s_0+\frac{1}{2}s_{max}}{s_{max}}\quad\text{and}\quad B=\exp\left(-\frac{2(s_0+\frac{1}{2}s_{max})^2}{s_{max}^2}\right)$$

Unfortunately, this rather tedious expression does not lend itself for an immediate Fourier transformation. After transformation of Equation 5.26 to the Fourier domain, the OTF of the tomographic system could be described using the relations 5.6. This in turn could lead to a description of the tomographic PSF.

Bessel PSF Invariance

A numerical description of the tomographic PSF could be used for tomographic deconvolution. However, as the Bessel beam profile is expected to be near-invariant along the propagation direction a deconvolution of the projections or the reconstructions with the imaging PSF is expected to suffice for ring removal. This is the case for a simulated deconvolution, shown in Section 5.3.3.

5.2. Reconstruction Theory

The sinogram is made up of all the projections obtained during image acquisition. Computerized reconstruction is used to reconstruct the raw data sinogram into cross-sectional images ready for interpretation. As mentioned in Section 2.5, reconstruction is essentially achieved through the inverse Radon transformation. However, multiple types of reconstruction in different orders can be found in the literature. In this section several types of reconstruction are discussed.

5.2.1. Filtered Back Projection

Filtered Back Projection, or FBP, is the most popular reconstruction method in the field of tomography due to its short reconstruction time [41]. One advantage is that the reconstruction procedure can be started as soon as the first projection has been measured. This not only saves time but it also reduces the amount of data that has to be stored simultaneously [24]. Reconstruction with FBP is done in two stages: back projection and filtering. Back projection resembles the inverse operation of a forward projection: instead of each point on the detector receiving a line integral of the object function, each point on the object domain is described with a value of the detector point where it projects to. This is done over all projection angles θ, summing up the values from each direction:

$$f_{BP}(x,y) = \int_0^{2\pi} p_\theta(x\cos\theta + y\sin\theta)d\theta \tag{5.27}$$

where p_θ is the detector function and x and y are coordinates in the transversal plane. The top row of Figure 5.3 shows results of the back projection process for different numbers of angles θ. It can be seen that even for a large number of angles, the outline of the shape in the image is not clear. One could say that with FBP the projections are simply run back through the image to obtain a rough approximation to the original. The projections will interact constructively in regions that correspond to the sources in the original image. A problem that arises is the blurring effect that occur in other parts of the reconstructed image. The low frequencies in the Fourier domain of the object are sampled with a higher density than the high frequencies. The low frequencies account for smooth surfaces, and the high frequencies account for details and edges. For this reason a multiplication with a high-pass filter in the frequency domain is introduced. This is often the Ram-Lak filter, named after Ramachandran and Lakshminarayanan [24]. With this filter, the weight of each frequency increases with its height until a cut-off is reached for noise reduction. The filtered back projection yields:

$$f_{FBP}(x,y) = \int_0^{2\pi} q_\theta(x\cos\theta + y\sin\theta)d\theta \tag{5.28}$$

where q_θ is the inverse Fourier transform of the multiplication of p_θ with the high-pass filter in Fourier domain. The bottom row of Figure 5.3 shows the filtered version of the back projection process for different

numbers of angles θ shown in the top row.

Hilbert Transform

FBP may also be performed in frequency domain. Note that q_θ in equation 5.28 represents filtering operation

$$Q_\theta(t) = \int_{-\infty}^{\infty} P_\theta(w)|w|e^{j2\pi wt}\,dw \tag{5.29}$$

in frequency domain with polar coordinate system (θ, w) and $t = (x\cos\theta + y\sin\theta)$. With some intermediate steps this equation can be expressed in terms of Inverse Fast Fourier transforms [24]:

$$Q_\theta(t) = \{\text{IFT of } j2\pi wP_\theta\} * \{\text{IFT of } \frac{-j}{2\pi}\text{sgn}(w)\} \tag{5.30}$$

which may in turn be written as

$$Q_\theta(t) = \frac{1}{2\pi^2 t} * \frac{\delta p_\theta(t)}{\delta t} \tag{5.31}$$

which is the Hilbert Transform of $\frac{\delta p_\theta(t)}{\delta t}$. The Hilbert Transform is usually expressed as a filtering operation and defined as

$$H(w) = \begin{cases} -j, & w > 0. \\ j, & w < 0. \end{cases} \tag{5.32}$$

More alternatives to execute FBP exist. FBP is widely used, however, in case the PSF is not ideal FBP reconstruction can cause artefacts and severe blurring in the reconstructed image [41]. Therefore, FBP is often used in combination with additional computerized reconstruction. Figure 5.4 shows a visualisation of the additional reconstruction methods discussed in this section and their use of FBP.

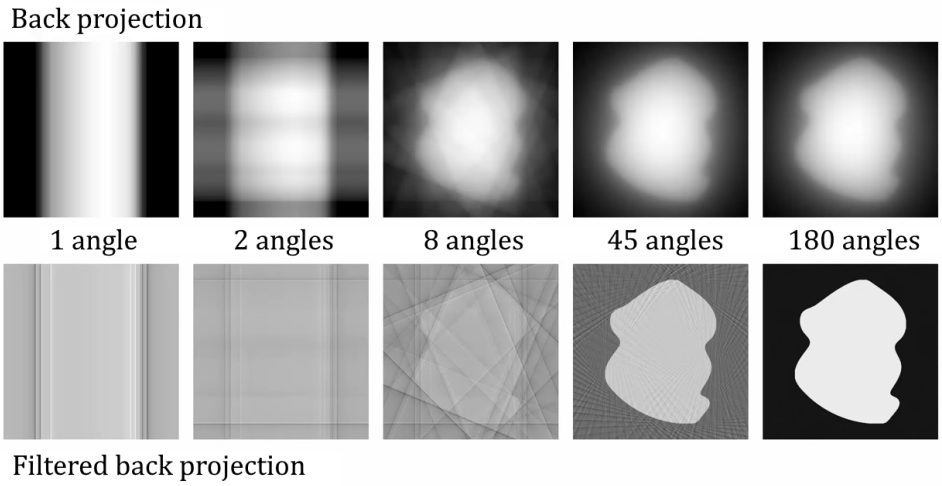

Figure 5.3: FBP for different numbers of angles for the tomography of an arbitrary shape. The top row shows the back projection, the bottom row shows the filtered equivalent. Source: *https://www.youtube.com/watch?v=pZ7JlXagT0w*

5.2.2. Frequency-Distance Relationship

The term Frequency-Distance Relationship, or FDR, is used to describe a frequency space filter based on the frequency–distance relationship of sinograms to deconvolve the distance-dependent PSF and reduce the influence of highly defocused data from the emission based OPT sinograms before they are reconstructed using FBP [45]. The blurring of the sinogram in the Fourier domain P_b can be described as

$$P_b(f_x, f_y) = H(f_x, f_y)P_o(f_x, f_y) \tag{5.33}$$

where H is a filter based on the PSF which describes the blurring and P_o is the Fourier transform of the sinogram of the object. There exists an inverse filter H^{-1} which can be used to remove the blurring caused by

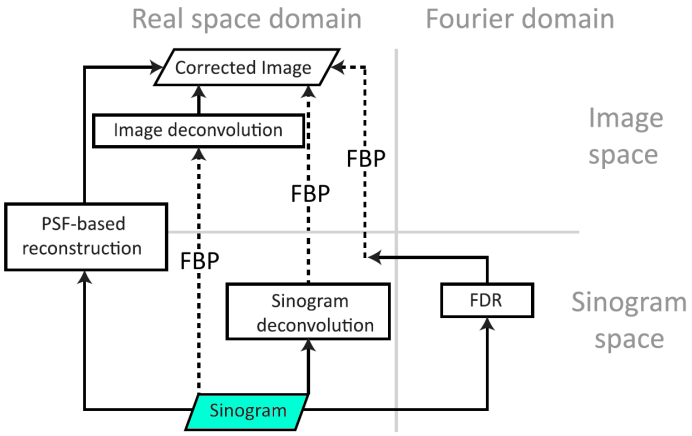

Figure 5.4: Visualization of the domain transformations and FBP operations used in different reconstruction methods. Source: adaptation of [41].

H. This is the essence of FDR. Experimental work has shown that FDR is inferior to the other reconstruction methods discussed from here on [41]. The reason for this is attributed to the fact that the H^{-1} is an approximation that is only exact if the optical transfer function of the imaging system varies slowly over the rotation angle, which is not always the case. Also, when noisy data is present the FDR filter has regions in the Fourier domain where a division is performed by values close to zero which amplifies the noise.

5.2.3. Deconvolution

As noted in the first part of this chapter the tomographic PSF is a complicated expression of the imaging PSF. It was shown in Equation 5.7 that for a Gaussian beam the tomographic PSF varies spatially. The resolution in the tangential direction deteriorates as the distance to the rotation axis increases, but the resolution in the radial direction is constant. Using a conversion to polar coordinates, the image can be successively deconvolved in the radial and angular direction, after which it is transformed back into Cartesian coordinates to obtain a deblurred reconstruction [43]. An example of the deconvolution of a fluorescent bead, close to a point object with a blurring similar to Figure 5.2c, is shown in Figure 5.5. For sparse objects, deconvolution shows the best reconstruction performance of the methods described in this section [41].

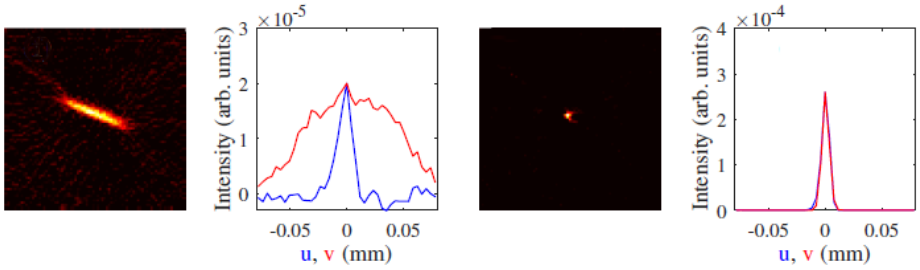

Figure 5.5: Reconstructed image of a blurred fluorescent bead and its intensity distribution followed by its deconvolution with a Gaussian tomographic PSF. Orientation of coordinates is as in Figure 5.2c. Source: [43].

It is expected that varied spatial blurring due to the PSF will not be as significant as seen here when an axicon generated Bessel beam is used with a long constant DoF. Instead of a spatially descriptive tomographic PSF the imaging PSF may yield sufficient performance when used in reconstruction with deconvolution. However, the concentric rings found in Bessel beams will cause distortions and deconvolution may play its part here.

5.2.4. PSF-based reconstruction

Point-spread function based, or PSF-based reconstruction, incorporates the point spread function of the imaging lens in an iterative reconstruction [40]. As shown in Figure 5.4 the sinogram is not filtered before FBP reconstruction and the image is not filtered after FBP reconstruction but the PSF of the focusing by the lens is directly included in the tomographic reconstruction. In essence, an optimization is performed to reconstruct the object **f** from the measured projections **p** and the effect of the imaging system PSF **A** using the least-squares method:

$$\underset{\mathbf{f}}{\operatorname{argmin}} \frac{1}{2} ||\mathbf{A} \cdot \mathbf{f} - \mathbf{p}||_2^2. \tag{5.34}$$

PSF-based reconstruction yields the best reconstruction performance of the methods described in this section for high signal-to-noise ratio and nonsparse objects [41].

5.3. OPT Simulation

OPT simulations have been performed for point sources in a Gaussian imaging system by Van der Horst and Kalkman [43]. In the first part of this section the findings of this Gaussian simulation will be revisited. In the second part of this section the imaging PSF for a Bessel imaging system, as described in Equation 5.9, is integrated into the existing OPT simulations and the result are discussed and compared with the Gaussian results.

5.3.1. Simulated Gaussian OPT

The simulation performed by Van der Horst and Kalkman, with results shown in Figure 2.9, is reproduced. The result is shown in Figure 5.6. As mentioned before, for Gaussian OPT the radial FWHM remains constant and the tangential FWHM increases for an increasing radial point source distance from the centre of rotation.

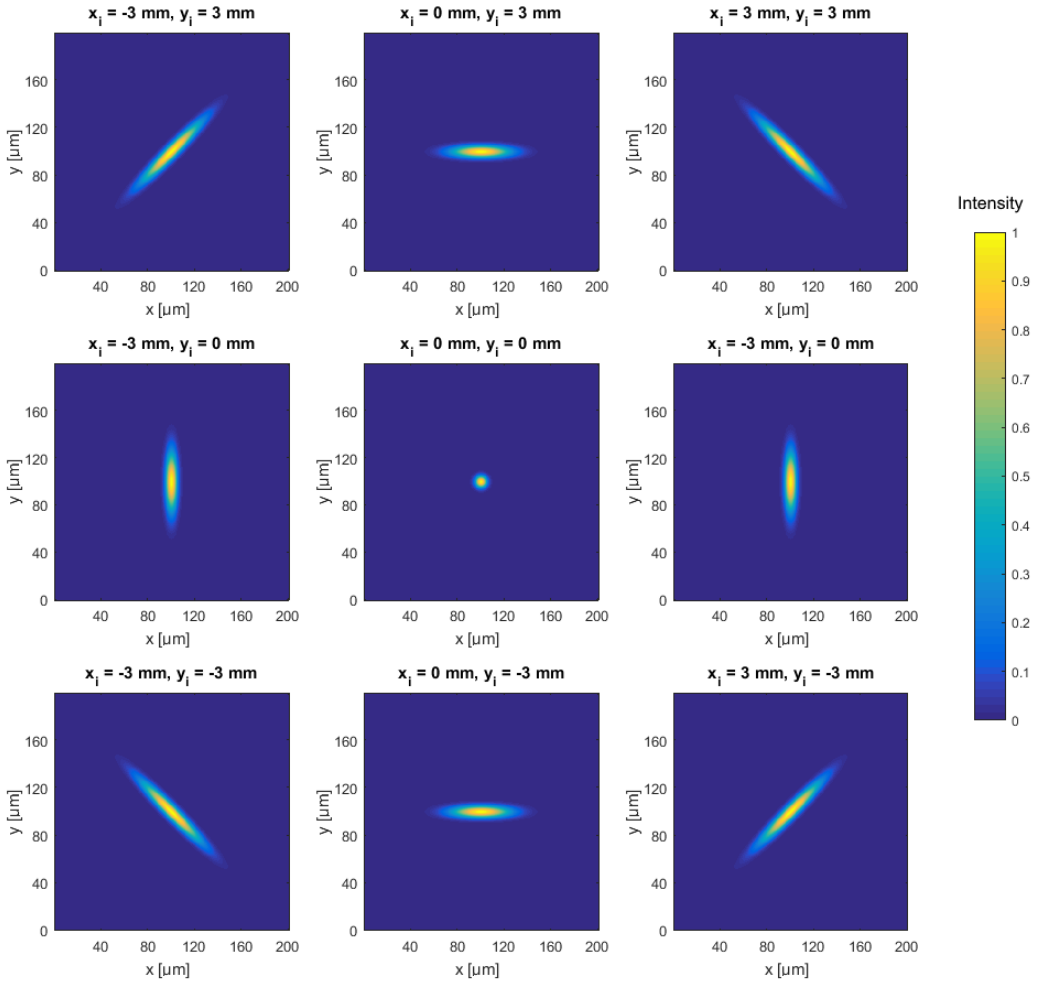

Figure 5.6: Image reconstructions of Gaussian OPT simulation for point sources at different positions (x_i ,y_i) in the object. The colorbar indicates normalized intensity.

5.3.2. Simulated Bessel OPT

Equation 5.9 is integrated as the imaging PSF into the OPT simulation. The simulation parameters are ω_0 = 1.0 cm, λ = 515 nm and axicon angle α = 20 °. Figure 5.8 shows the resulting tomographic PSF's for the same point source positions (x_i, y_i) as in the Gaussian OPT simulation. The intensities are normalized for each reconstruction. The individual intensities have been compared and the maximum difference in maximum

intensity amongst all the reconstructions is no more than 1%. A striking difference with the Gaussian case is the absence of visible blurring. This implies a consistent resolution over a relatively large DoF. For the chosen parameters the resulting centre spot diameters are much smaller than what would be achievable with a Gaussian OPT set-up. Another striking but expectable feature is the presence of concentric circles.

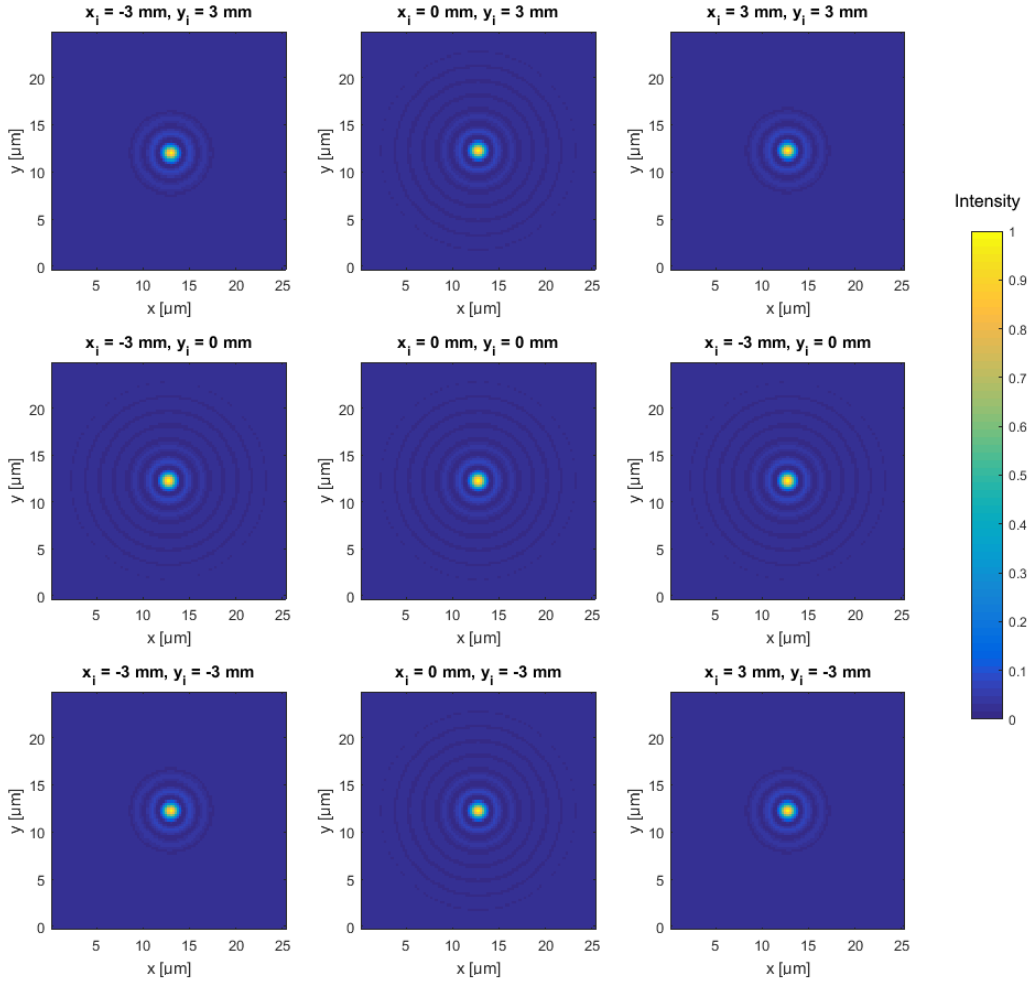

Figure 5.7: Image reconstructions of Bessel OPT simulation for point sources at different positions (x_i, y_i) in the object. ω_0 = 1.0 cm, λ = 515 nm and axicon angle α = 20 °. The colorbar indicates normalized intensity.

Figure 5.8 serves to accentuate the concentric circles that are present in the OPT result. The data of the centered reconstruction of 5.7, with (x_i = 0 mm, y_i = 0 mm), is logarithmically scaled and an excerpt of the newly normalized intensities is shown. Quantitatively Figure 5.8 is nugatory, it merely serves to accentuate the presence of concentric circles.

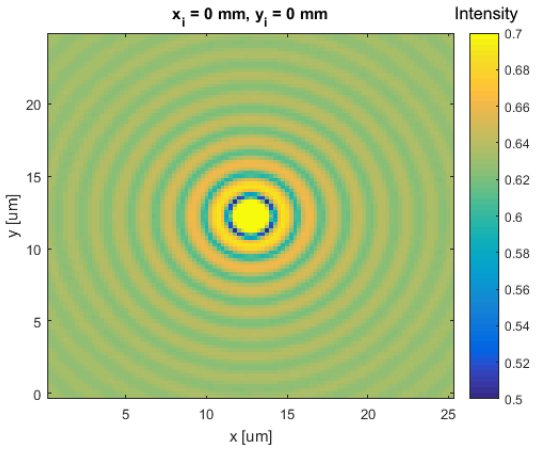

Figure 5.8: Image reconstructions of Bessel OPT simulation for point sources at (x_i = 0 mm, y_i = 0 mm) in the object with logarithmic scaling. The colorbar indicates normalized intensity for the logarithmically scaled data.

FWHM versus Distance from centre

Simulations are performed for point sources with different radial distances from the object centre in the same fashion as shown for the Gaussian case in Figure 2.9. Figure 5.9 shows a quantification of the effect of radial point source displacement in x-direction on the radial and tangential FWHM resolution of the centre spot of the reconstruction. The tangential resolution hardly deteriorates as the radial position of the object increases within the range of typical point source radial displacement values for visible light OPT (r < 3 mm). The right part of Figure 5.9 shows tangential direction FWHM increase for more extreme radial displacements. The FWHM in radial direction remains constant over the entire range of radial displacement. The theoretical results for FWHM deterioration for radial displacement show that a consistent resolution can be maintained over the entire range of a typical OPT object.

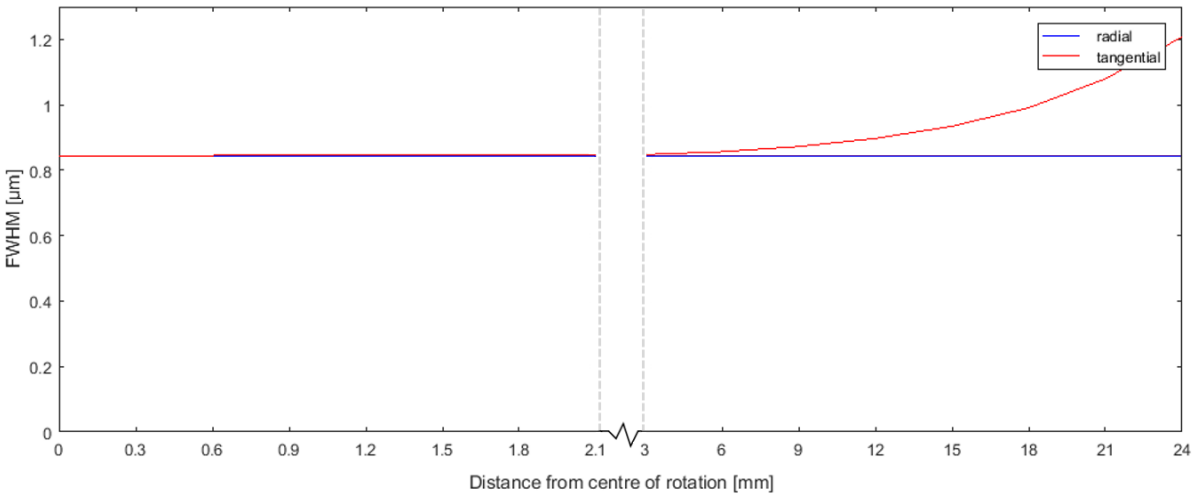

Figure 5.9: Theoretical FWHM in the radial and tangential direction as function of the radial distance from the centre of rotation.

One-on-one Gaussian-Bessel OPT Comparison

The parameters chosen for the Bessel OPT simulation are not directly comparable with the Gaussian OPT simulation. Even though the difference between the dimensional order of magnitude between the reconstruction results for the shown Bessel case and the Gaussian case is already substantial, this section is not complete without a 'one-on-one' comparison. The reconstruction of the Bessel OPT with point source position (x_i = 3 mm, y_i = 3 mm) yields a centre spot radius of 1.1 µm. A Gaussian OPT simulation is performed with a focused Gaussian beam waist of ω_0 = 1.1 µm.

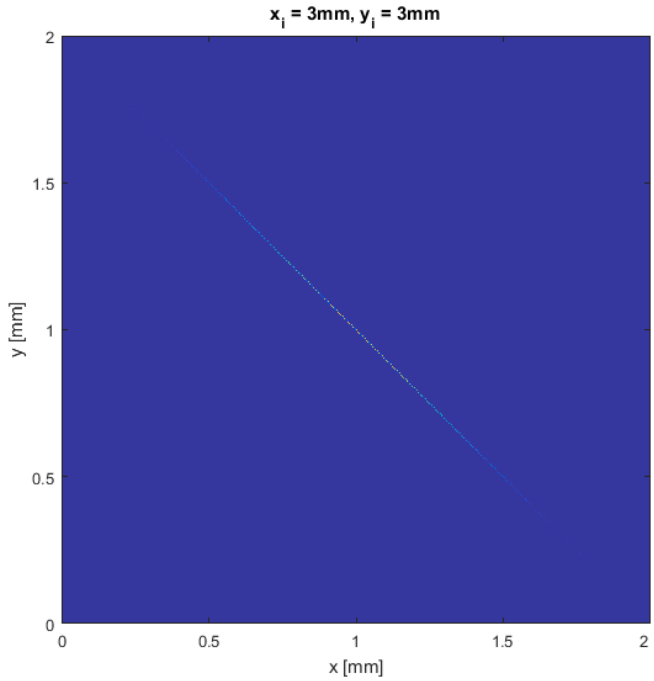

Figure 5.10: Reconstruction of the Gaussian OPT with point source position (x_i = 3 mm,y_i = 3 mm) with a focused beam waist of 1.1 µm.

The reconstruction of the Gaussian OPT is depicted in Figure 5.10. The blurring is extreme, with an FWHM in the tangential direction of 0.57 mm. Figure 5.11 shows the Gaussian and the Bessel reconstruction side-by-side on the same scale. Note that the radial resolution of the Gaussian reconstruction remains constant for radial displacement and is equal to that of the Bessel reconstruction.

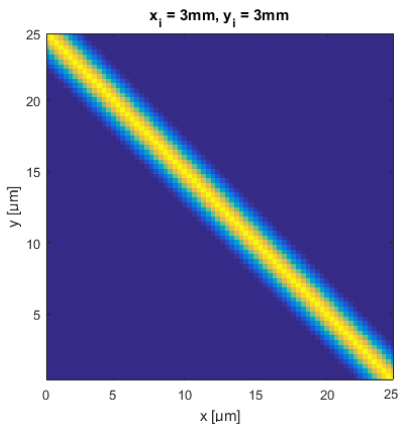

(a) Zoom in on reconstruction of the Gaussian OPT with point source position (x_i = 3 mm,y_i = 3 mm) with a focused beam waist of 1.1 µm.

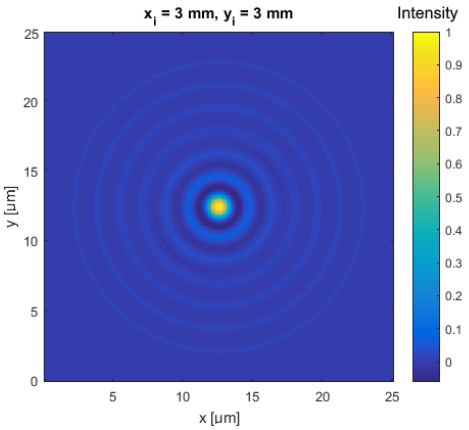

(b) Reconstruction of the Bessel OPT with point source position (x_i = 3 mm,y_i = 3 mm) with a centre spot radius of 1.1 µm.

Figure 5.11: Reconstructions of the Gaussian and the Bessel OPT of a point source at (x_i = 3 mm,y_i = 3 mm). Gaussian ω_0= 1.1 µm and equals the centre spot radius of the Bessel reconstruction. The colorbar indicates normalized intensity.

Bessel OPT Limits

Although no significant blurring occurs for the theoretical tangential FHWM in the range of a typical OPT object, blurring does occur eventually. Figure 5.12 shows the Bessel OPT sinogram and reconstruction result

for a point source at (x_i = 20 mm, y_i = 20 mm). Note that the projections in the sinogram have been aligned according to their peak intensity, hence the absence of a sinusoidal shape.

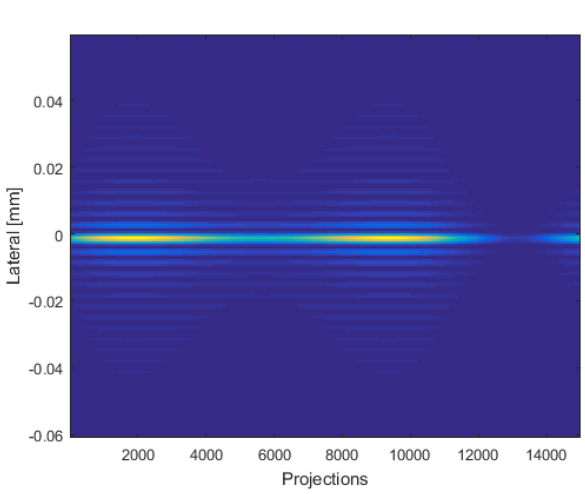

(a) Bessel OPT reconstruction results for (x_i = 20 mm, y_i = 20 mm).

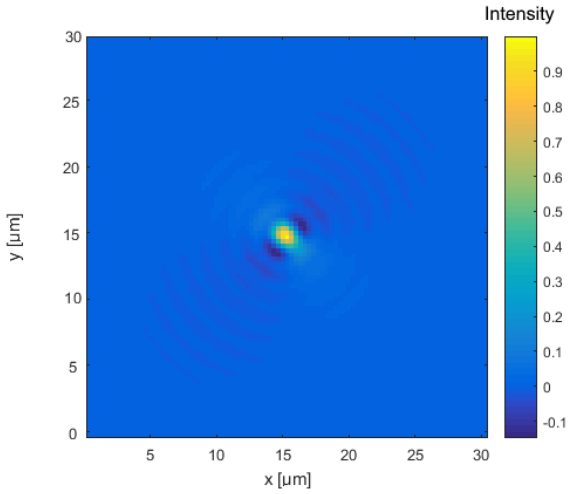

(b) Bessel OPT reconstruction results for (x_i = 20 mm, y_i = 20 mm).

Figure 5.12: Bessel OPT sinogram and reconstruction results for (x_i = 20 mm, y_i = 20 mm). ω_0 = 1.0 cm, λ = 515 nm and axicon angle α = 20 °.

It is visible in the sinogram that, even though the Bessel beam is very wide, for an extreme displacement as (x_i = 20 mm, y_i = 20 mm) the point source can be out of focus. This results in blurring of the reconstruction in 5.12b. The reconstruction contains negative intensity values, this may occur when using the FBP algorithm of Matlab's `iradon`. This is very likely an artefact from the filtering step and is of course invalid.

5.3.3. Simulated Bessel OPT Deconvolution

The concentric circles that are present in the Bessel OPT reconstructions may be removed through deconvolution in the reconstructed image, as is done to remove blurring for the Gaussian case as discussed in Section 5.2.3. A 2D deconvolution of a Bessel OPT reconstruction obtained with an OPT simulation for (x_i = 0 mm, y_i = 0 mm) is performed with the imaging PSF described by Equation 5.9. Matlab's `deconvlucy` function is used for deconvolution with its default settings. Figure 5.13 displays the reconstruction, the PSF and the deconvolution result.

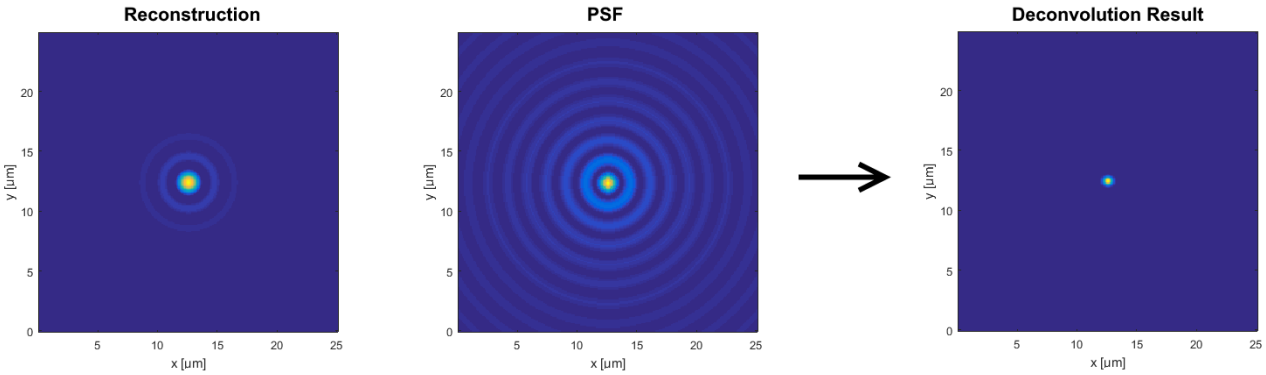

Figure 5.13: Deconvolution of OPT reconstruction for (x_i = 0 mm, y_i = 0 mm) with analytic Bessel PSF. ω_0 = 1.0 cm, λ = 515 nm and axicon angle α = 20 °. The intensity is normalized.

The concentric rings in the reconstruction are successfully removed with the simulated deconvolution. The reconstruction deconvolution is tested for (x_i) up to 2.5 mm and remains successful.

An alternative to deconvolution of the reconstruction is deconvolution of the projection. Figure 5.14 shows the deconvolution of the projection of a point source with position (x_i = 0 mm, y_i = 0 mm) and the

PSF. The concentric rings in the projection are successfully removed with the simulated deconvolution. Theoretically, deconvolution can be used to remove the concentric rings both in the Bessel projection and the Bessel OPT reconstruction.

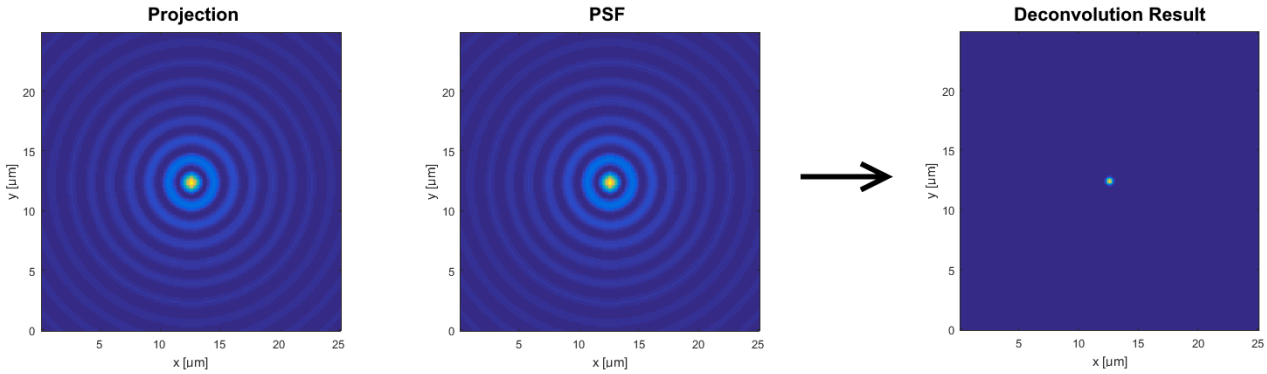

Figure 5.14: Deconvolution of projection for (x_i = 0 mm, y_i = 0 mm) with analytic Bessel PSF. ω_0 = 1.0 cm, λ = 515 nm and axicon angle α = 20 °. The intensity is normalized.

6

Materials and Methods

Practical work is carried out to investigate the DoF extension with an axicon set-up. The axicon is combined with an objective lens, as described in Section 4.2.3, and a 4f system for image magnification.

Four cases are considered for PSF measurements in transmission:

- Coherent aperture illumination with a Gaussian system
- Incoherent aperture illumination with a Gaussian system
- Coherent aperture illumination with a Bessel system
- Incoherent aperture illumination with a Bessel system

Furthermore, four similar cases of resolution target measurements are considered in transmission:

- Coherent resolution target illumination with a Gaussian system
- Incoherent resolution target illumination with a Gaussian system
- Coherent resolution target illumination with a Bessel system
- Incoherent resolution target illumination with a Bessel system

6.1. PSF Measurements

The goal of these measurements is to emulate a bright point source and observe the response of the imaging system in order to obtain an experimental Point Spread Function.

6.1.1. Materials

Figure 6.2 displays pictures of the set-ups used for the four different cases of PSF measurement. A Laser Diode Module (A) (CPS635R - Collimated Laser Diode Module, 635 nm, 1.2 mW, Round Beam, Ø11 mm Housing, Thorlabs) acts as a coherent light source. The incoherent light source is an LED (A) (LZ1-00U600, Led Engin), with a data sheet power spectrum as depicted in Figure 6.1. The FWHM bandwidth of the LED is 12 nm. Both light sources are focused onto a 10 µm aperture (C) using an objective (B) (X Plan-Neofluar 2.5x/0.075 Pol M27, Zeiss). The Gaussian 4f imaging system is comprised out of two lenses: one with focal distance f = 10.0 mm (D) (LB1157-A - N-BK7 Bi-Convex Lens, Ø6.0 mm, Thorlabs) and the other with focal distance f = 100 mm (E) (LB1676-A - N-BK7 Bi-Convex Lens, Ø1", Thorlabs). The image is detected using a camera (F) (ORCA-ER, Hamamatsu).

In the Bessel system an axicon and an objective lens are added to the set-up. The objective lens (G) has a focal distance of f = 25.4 mm (LA1951-A - N-BK7 Plano-Convex Lens, Ø1", Thorlabs). The axicon (H) has a base angle of α = 20 °(AX2520-A - 20.0 °, Ø1", Axicon).

A linear translation stage (25 mm Travel Translation Stage, Thorlabs) is used to move the light source, objective and aperture assembly with respect to the imaging system.

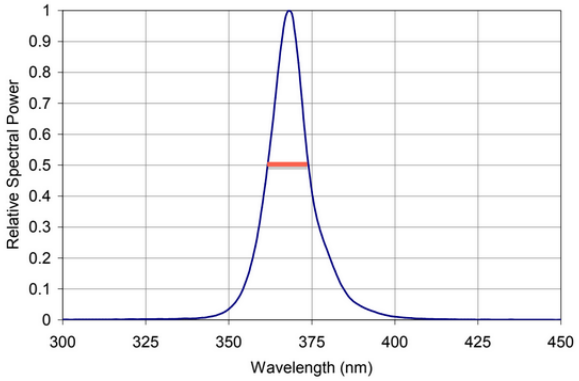

Figure 6.1: Power spectrum of the incoherent light source (LZ1-00U600, Led Engin). The FWHM bandwidth is 12 nm.

6.1.2. Methods

The axicon objective lens (G) and the axicon (H) are positioned according to the Bessel imaging set-up described in 4.2.3 [50]. The axicon objective lens (G) is 10 mm removed from the axicon. The axicon (H) is 25 mm removed from the object plane of the Gaussian 4f system comprised of lens (D) and (E).

Images have been recorded of the emulated point source with the paraxial distance to the imaging system (either Gaussian or Bessel) varying in steps of 0.5 mm. For the Gaussian coherent, Gaussian incoherent and Bessel coherent set-ups a camera integration time of 0.01 s was used. For the incoherent Bessel set-up an integration time of 0.01 s hardly yielded any signal. It was found more detailed results with higher contrast were achieved for longer integration times and a camera integration time of 20 s was used.

6.2. Resolution Target Measurements

The goal of these measurements is to investigate the DoF extension when imaging a 2D object in transmission using a Bessel imaging system.

6.2.1. Materials

For the resolution target illumination a similar set-up to the PSF measurement set-ups is used, where the objective and the aperture are replaced by a 1951 US Air Force Resolution Target (3" x 3" Positive, 1951 USAF Resolution Target, Edmund Optics). A collimated beam of light with a wavelength of 514 nm is created using an Argon laser (150m Select, Laser Physics) to serve as a coherent light source. Again, the incoherent light source is an LED (LZ1-00U600, Led Engin). The Gaussian 4f imaging system is comprised out of two lenses: one with focal distance f = 50.0 mm (LA1131-A - N-BK7 Plano-Convex Lens, Ø1", Thorlabs) and the other with focal distance f = 200.0 mm (AC254-200-C - Achromatic Doublet, Ø1", Thorlabs). The image is detected using a camera (ORCA-ER, Hamamatsu).

In the Bessel system an axicon and an objective lens are added to the set-up as in the PSF measurement set-ups. The objective lens has a focal distance of f = 25.4 mm (LA1951-A - N-BK7 Plano-Convex Lens, Ø1", Thorlabs). The axicon has a base angle of α = 20 °(AX2520-A - 20.0 °, Ø1", Axicon). A linear translation stage (Thorlabs 25 mm Travel Translation Stage) is used to move the resolution target with respect to the imaging system.

6.2.2. Methods

The axicon objective lens and the axicon are positioned according to the Bessel imaging set-up described in 4.2.3 [50]. The axicon is 25 mm removed from the object plane of the Gaussian 4f system. No signal is detected when the coherent illumination is strictly paraxial. Therefore, in the coherent case, the target is illuminated under a slight angle to the optical axis. Images have been recorded of the resolution target with the paraxial distance to the imaging system (either Gaussian or Bessel) varying in steps of 0.5 mm. Images were captured of Group 2, Element 5 and 6 of the US Air Force Resolution Target. For the coherent illumination a camera

integration time of $2 \cdot 10^{-5}$ s was used. For the incoherent illumination a camera integration time of 0.02 s was used.

The shading of the target varies over its position on the paraxial axis due to the off-axis illumination in the coherent illumination case. Therefore the resolution target is adjusted in the direction perpendicular to the paraxial direction every couple of measurements to keep the same elements in the field of view. This is done with a dedicated stand with one degree-of-freedom for adjustment.

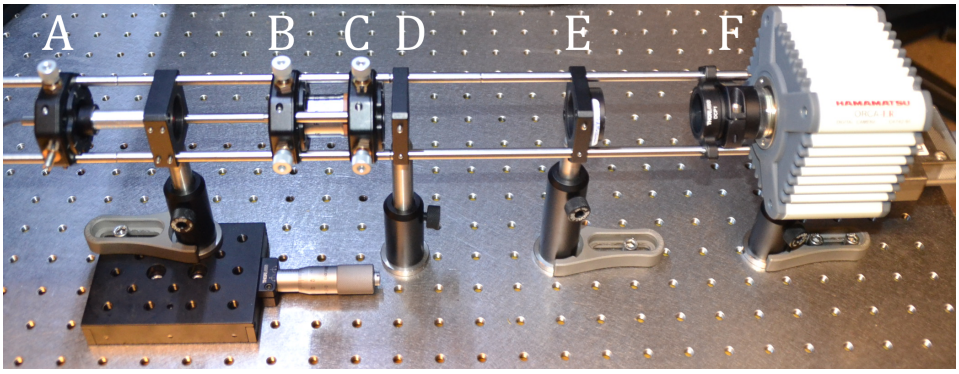

(a) A: coherent light source, B: objective, C: aperture (diameter = 10 µm), D: lens (f = 10 mm), E: lens (f = 100 mm), F: camera.

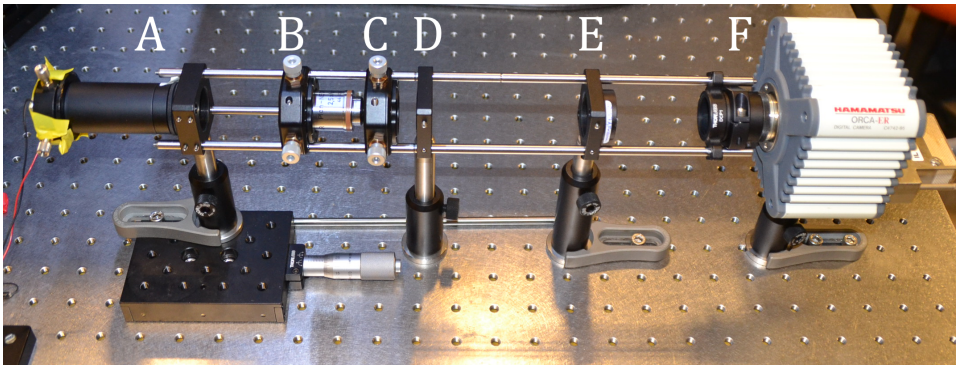

(b) A: incoherent light source, B: objective, C: aperture (diameter = 10 µm), D: lens (f = 10 mm), E: lens (f = 100 mm), F: camera.

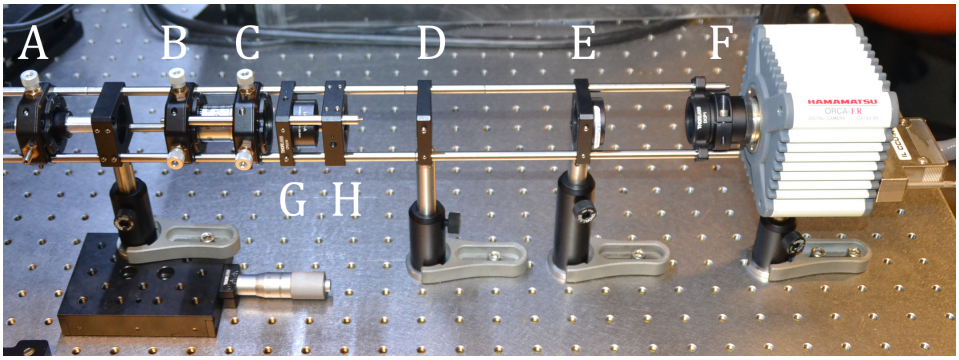

(c) A: coherent light source, B: objective, C: aperture (diameter = 10 µm), D: lens (f = 10 mm), E: lens (f = 100 mm), F: camera, G: lens (f = 25.4 mm), H: axicon (α = 20 °).

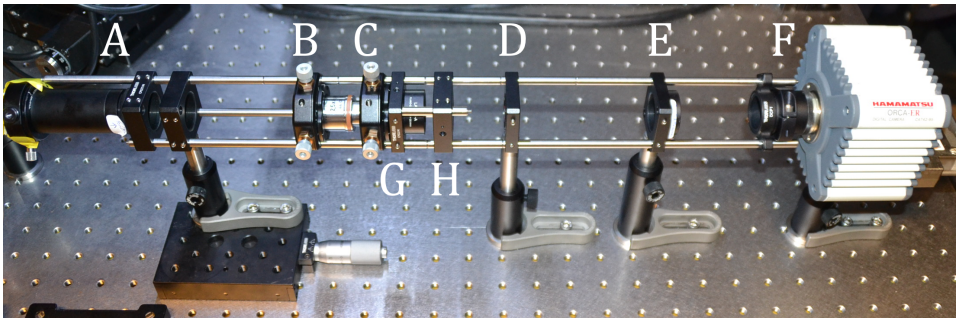

(d) A: incoherent light source, B: objective, C: aperture (diameter = 10 µm), D: lens (f = 10 mm), E: lens (f = 100 mm), F: camera, G: lens (f = 25.4 mm), H: axicon (α = 20 °).

Figure 6.2: PSF measurement set-ups.

7

Results

In this section the results of the measurements explained in the previous section are analysed. The relation between resolution and DoF is considered especially.

7.1. PSF Measurements

7.1.1. Gaussian Beam System

Figure 7.1 shows the 10 µm aperture in focus for both incoherent and coherent illumination with their corresponding profiles. Calibration of the pixel size is done with focused Gaussian measurements of the resolution target. The FWHM of the derivative of the edge of the profile of the incoherent illumination yields 4.1 µm versus 8.8 µm for the coherent illumination.

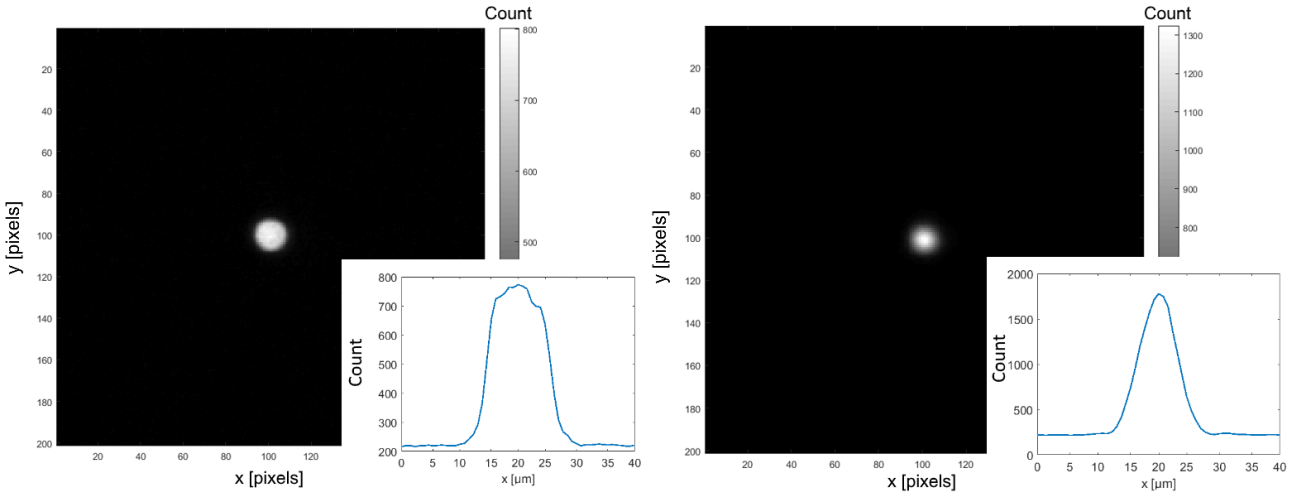

Figure 7.1: Left: 10 µm aperture in focus with incoherent illumination and corresponding profile. Right: 10 µm aperture in focus with incoherent illumination and corresponding profile. The colorbar indicates the number of counts per pixel.

The DoF of the Gaussian system is established by analysis of the FWHM of the Gaussian beam profile for different axial positions. The result is displayed in Figure 7.2. It can be observed that the coherent illumination FWHM is smaller than the incoherent illumination FWHM.

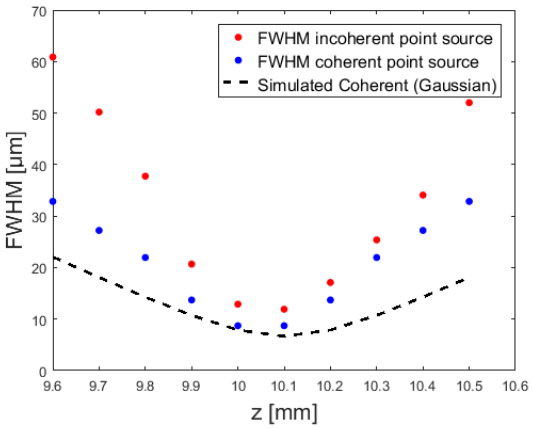

Figure 7.2: FWHM of intensity distribution of point sources versus axial distance, with coherent and incoherent illumination in the Gaussian beam system and for a Gaussian model.

7.1.2. Bessel Beam System

Figure 7.3 shows images of the 10 µm aperture at 5.5 mm from the Bessel beam imaging system for both incoherent and coherent illumination with images of their corresponding profiles. The coherent PSF shows a clear Bessel profile with a clearly distinguishable beam core and side lobes. The incoherent profile is less representative of a Bessel profile, although some concentric rings can be spotted. Figure 7.4 shows the coherent PSF data with adjusted color representation, and the lower intensity concentric rings can be seen more clearly.

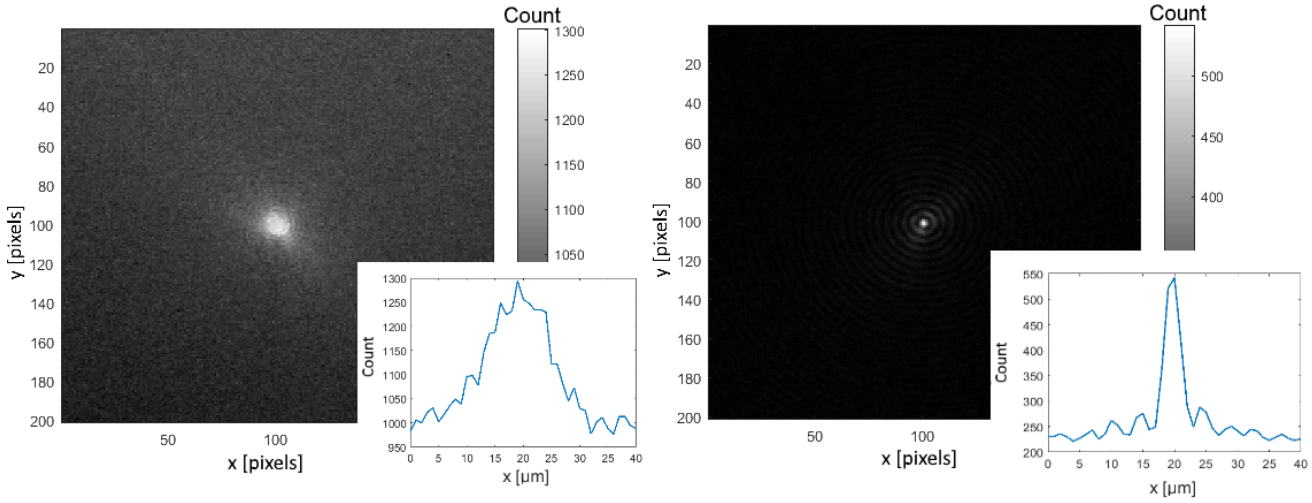

Figure 7.3: Left: 10 µm aperture at 5.5 mm from the Bessel imaging system with incoherent illumination and corresponding profile. Right: 10 µm aperture at 5.5 mm from the Bessel imaging system with coherent illumination and corresponding profile. The colorbar indicates the number of counts per pixel.

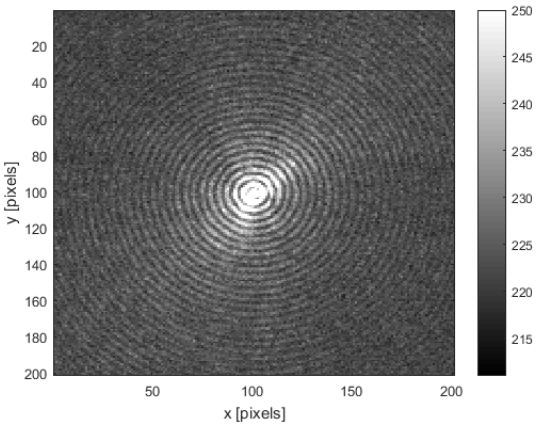

Figure 7.4: 10 µm aperture at 5.5 mm from the Bessel imaging system with coherent illumination, as in Figure 7.3 (right), with adjusted color representation. The colorbar indicates the number of counts per pixel

The DoF of the Bessel system is established by analysis of the FWHM of the centre core beam of the profile for different paraxial positions. Figure 7.5 shows the FWHM of the measured coherent profiles and the simulated FWHM of the axicon set-up model [50] as discussed in Section 4.2.3.

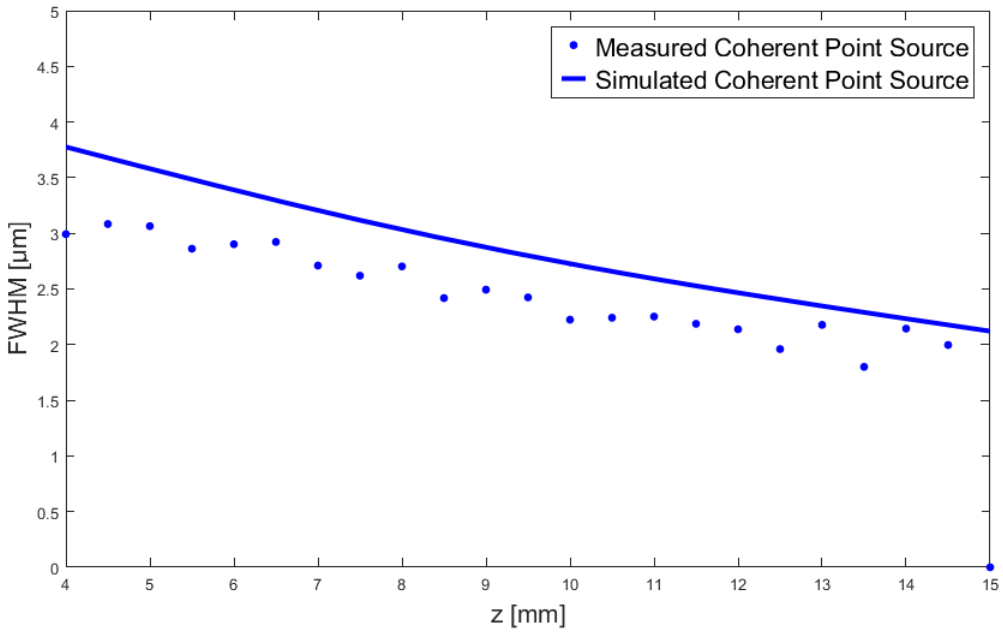

Figure 7.5: FWHM of centre core beam of measurements and simulated model of point source with coherent illumination versus axial distance.

Figure 7.6 shows the same data, with addition of the centre core FWHM of the incoherent point source and a Gaussian model with a focused FWHM = 2.5 µm for the coherent case. The latter is added to demonstrate the extended DoF offered by the Bessel system compared to a conventional Gaussian system. As one would expect with Figure 7.3 in mind, the resolution of the incoherent point source is considerably worse than that of the coherently illuminated case.

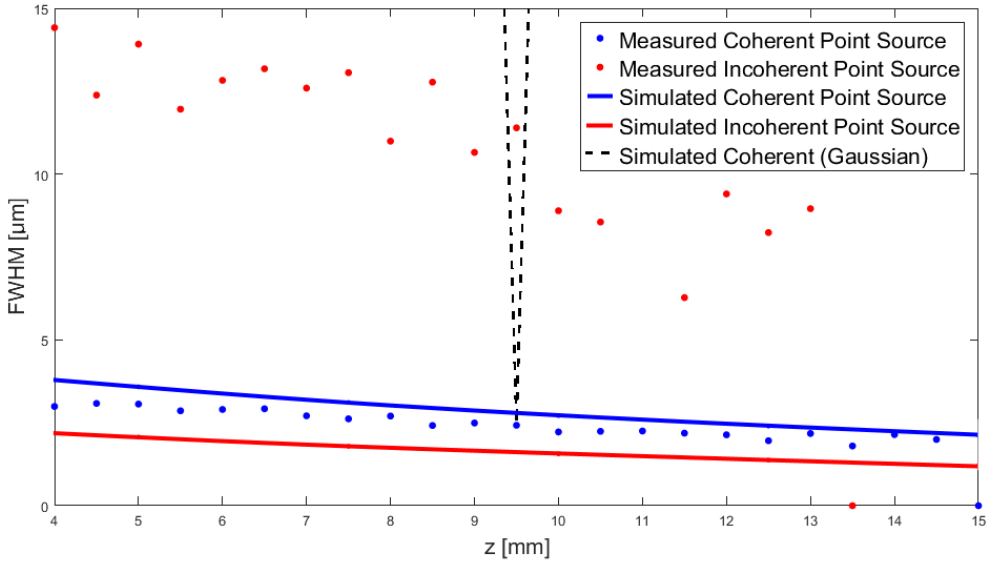

Figure 7.6: FWHM of centre core beam versus axial distance of coherent and incoherent point source measurements , simulated model of a coherent point source and simulated model of a coherent Gaussian point source with FWHM = 2.5 µm in focus.

7.2. Resolution Target Measurements

7.2.1. Gaussian Beam System

Figure 7.7 shows the focused resolution target imaged with the incoherent Gaussian set-up. For each projection made over the paraxial axis a line profile is taken over the horizontal segments of Element 5 of Group 2 of the resolution target, indicated by the red crosses in Figure 7.7. The transition of the transparent glass between the upper and the middle segment to the middle segment is extracted and the transition is fitted with a 'Knife Edge' function [1], depicted in red. This smooth representation of the 'edge' has a derivative of which the FWHM can be determined.

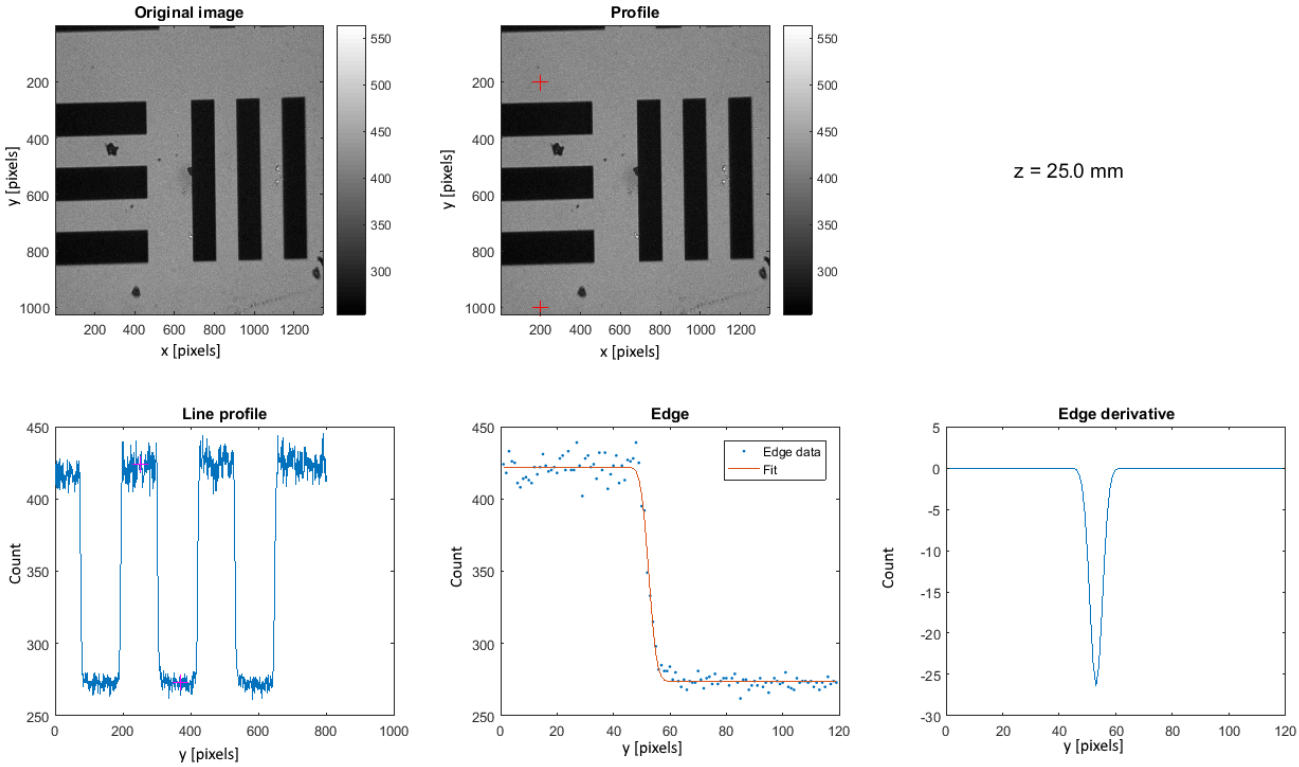

Figure 7.7: Focused resolution target imaged with an incoherent Gaussian beam: the line segment between the red crosses yields the line segment in the bottom left of which one transition is fitted to create a smooth edge. The FWHM of the derivative of the edge is used as a measure of spatial resolution.

Figure 7.8 shows the FWHM determined in this manner for several resolution target positions on the optical axis z. The edge derivative FWHM results are in the same range as the PSF FWHM results, slightly exceeding the coherent PSF results and smaller than the incoherent PSF FWHM results in Figure 7.2.

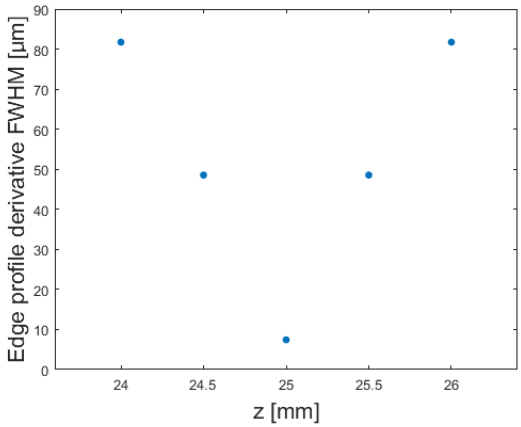

Figure 7.8: The FWHM of the derivative of the edge of Element 5 of Group 2 versus axial distance z.

7.2.2. Bessel System

Coherent Illumination

Figure 7.9 shows the resolution target imaged at 19 mm from the imaging system with the coherent Bessel set-up. The 'edge' derivative FWHM is determined in a similar manner as described in the previous section. However, as the raw images are quite noisy an averaged area profile is used rather than a single line profile to

provide data for the 'Knife Edge' function fit. Others have used smoothing or 2D Wiener filtering to increase image quality [35] [51]. Smoothing does improve the image aesthetically but imposes significant changes to the raw data. This is why averaging is considered more suitable for noise reduction.

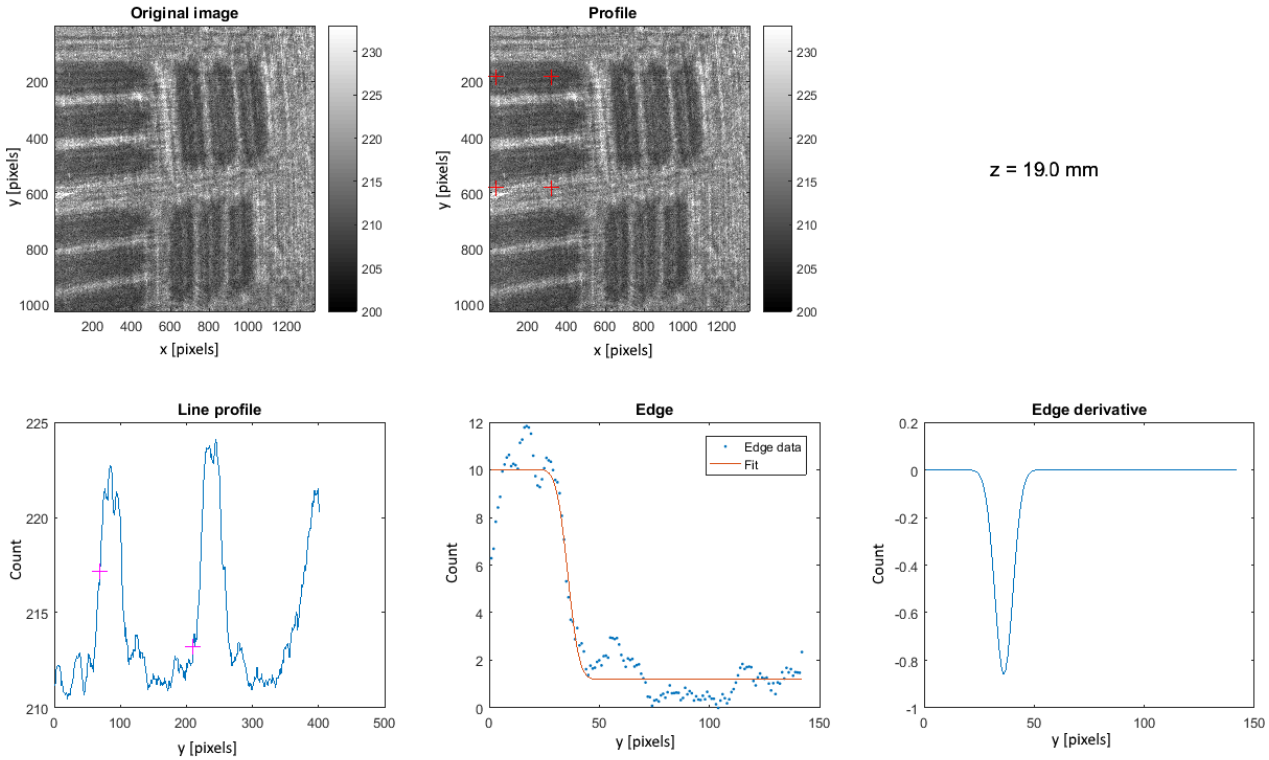

Figure 7.9: Resolution target for the coherent Bessel set-up: the area segment between the red crosses is averaged over the horizontal direction to obtain the line segment in the bottom left of which one transition is fitted to create a smooth edge. The FWHM of the derivative of the edge is used as a measure of spatial resolution.

Figure 7.10 shows the edge derivative FWHM for different paraxial positions of the resolution target. The FWHM values for incoherent illumination are higher than the FWHM values for coherent illumination. Substantial differences in FWHM can be seen within both series of measurements.

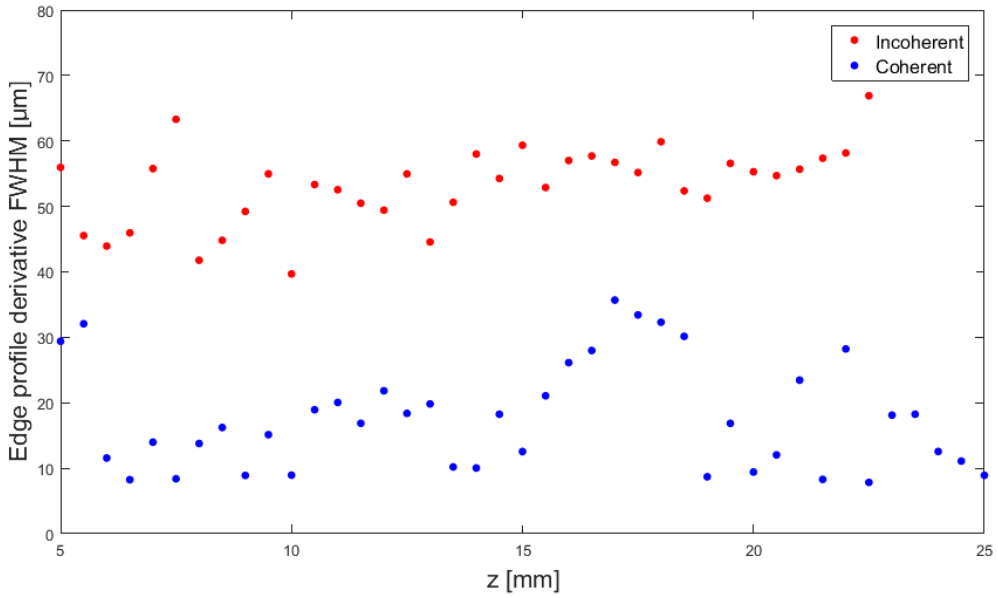

Figure 7.10: The FWHM of the derivative of the edge of Element 5 of Group 2 versus paraxial distance z for the coherent and the incoherent Bessel beam system.

Incoherent Illumination

The 'edge' derivative FWHM is determined for the images of the incoherent Bessel set-up in the same manner as for the coherent Bessel set-up. Figure 7.11 shows the resolution target imaged at 19 mm from the imaging system with the incoherent Bessel set-up. Figure 7.10 shows the resulting FWHM for paraxial locations z. As with the coherent measurements, the FWHM of the incoherent Bessel edge measurements is considerably larger than the centre core beam FWHM of the coherent Bessel PSF measurements.

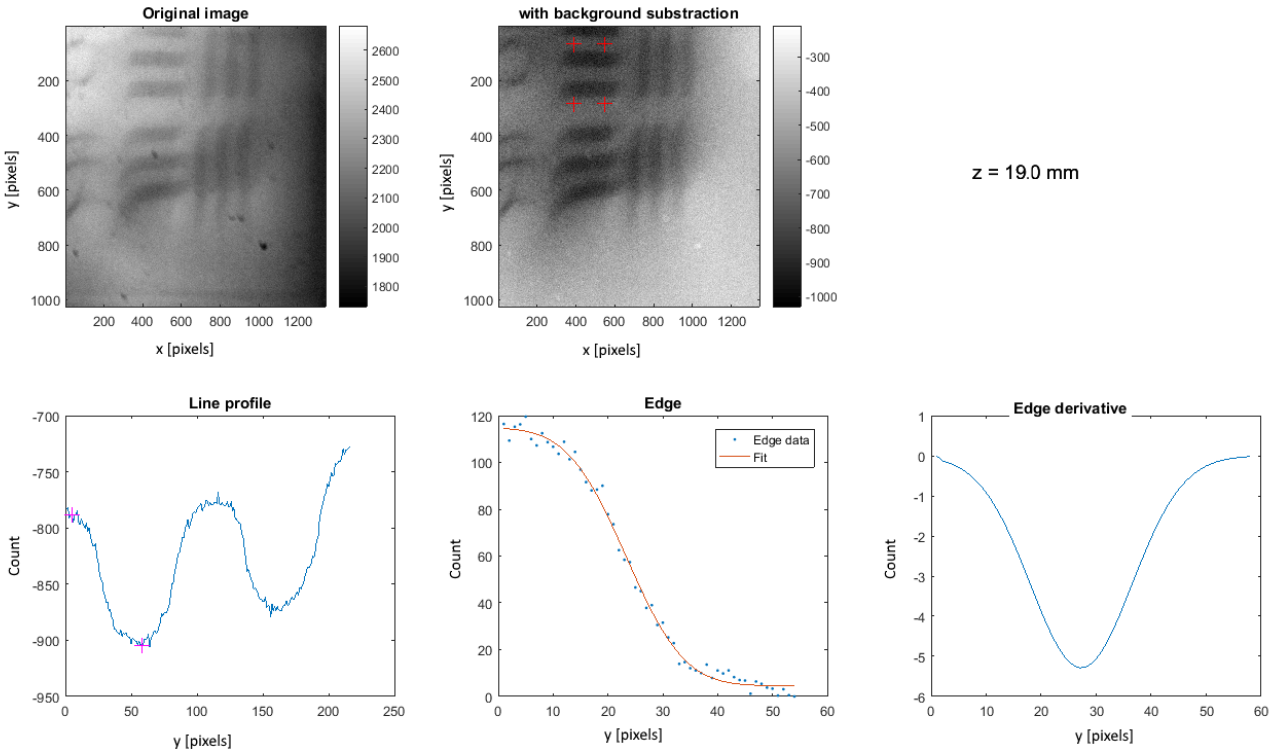

Figure 7.11: Resolution target for the incoherent Bessel set-up: the area segment between the red crosses is averaged over the horizontal direction to obtain the line segment in the bottom left of which one transition is fitted to create a smooth edge. The FWHM of the derivative of the edge is used as a measure of spatial resolution.

8

Conclusions, Discussion & Recommendations

The goal of this research is to extend the depth of field in Optical Projection Tomography. Non-diffracting beams have been found to show potential in DoF extension, axicon generated Bessel beams have been assessed for their application in OPT through theoretical analysis and with numerical simulations and practical work with a Bessel imaging set-up has been performed.

8.1. Conclusions

The findings of this research lead to several conclusions. Numerical simulations of axicon generated Bessel beams show an increase of DoF for images of point sources compared to Gaussian equivalents with similar resolution. This aligns with what is already known from the literature.

The use of Bessel beams in OPT is investigated for the first time and simulations of OPT with axicon generated Bessel beams show virtually no blurring for reconstructed point sources within multiple centimetre ranges.

Experiments with emulated point sources match theoretical descriptions of DoF extension from the literature in terms of resolution for the coherently illuminated case. However, resolution is worse for incoherent illumination. Resolution analysis for objects that are not point sources is performed for the first time. For larger objects the resolution worsens for both coherent and incoherent illumination. At lower resolution, the DoF extension is still significant compared to Gaussian equivalents with similar resolution. This leads to the main conclusion of this research:

Extended depth of field in OPT can be achieved with non-diffracting axicon generated Bessel beams. However, as object size increases the resolution deteriorates rapidly. Therefore, widefield Bessel imaging may be useful for OPT imaging of very large sparse samples but it is not suited for imaging of large objects when a high resolution is desired.

8.2. Discussion

Regarding the Gaussian PSF measurements for coherent and incoherent light, both the FWHMs exceed the FWHMs of a theoretical Gaussian model. The FWHM of the derivative of the edge of the profile of the incoherent illumination is significantly smaller for incoherent illumination. This is as one would expect, as interference along the edges deteriorates resolution for coherent illumination. However, the FWHM of the entire distribution is smaller in the case of coherent illumination. This is not as one would expect. The incoherent intensity profile depicted in blue in the left of Figure 7.1 suggests that the aperture creates a distribution with two edges rather than a point source.

A contribution to the unexpected difference in FWHM of the incoherent and coherent focused Gaussian measurement may be made by something known as 'Edge shifting' [12] [17]. A property of coherent images with regard to edges is that the intensity profile crosses the location of the actual edge with only $\frac{1}{4}$ of its asymptotic value of intensity, whereas the incoherent image crosses with a value of $\frac{1}{2}$ of its asymptotic value.

Figure 8.1a depicts an illustration of a typical edge shifting example. Figure 8.1b shows the unscaled intensity distributions of the focused Gaussian PSF measurements, aligned at their centres, with a rough estimate of the actual location of the edge based on the asymptotic values of the intensities. Quantitatively, a 5 µm aperture radius would place the edge approximately five pixels from the centre, which does not agree with the estimation. Reservations are in place when comparing these situations as 8.1a considers a straight edge, and the PSF measurements involve a circular aperture.

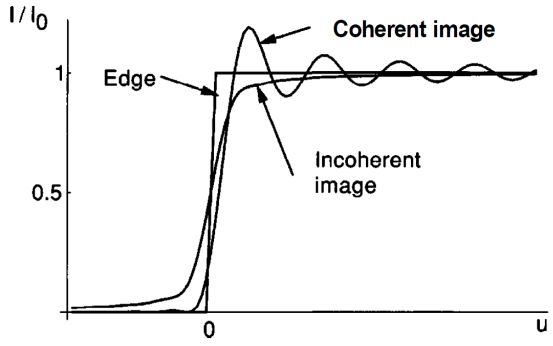

(a) Typical intensity profiles of an edge illuminated with coherent and incoherent light. Source: [17].

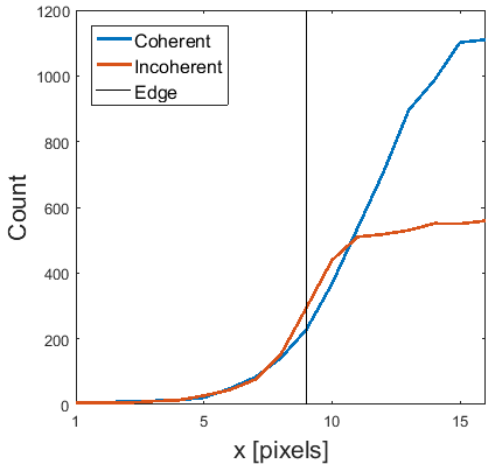

(b) Intensity profiles of the aperture illuminated with coherent and incoherent light. A rough estimate of the position of the edge has been made.

Figure 8.1: Edge shifting in a typical example and in unscaled intensity distributions of the focused Gaussian PSF measurements.

The difference in lighting conditions due to the use of two different light source may also contribute to differences in the coherent and incoherent FWHM values, complicating comparisons with theoretical expectations.

Regarding the Bessel PSF measurements, the point source with coherent illumination shows a typical Bessel distribution. A clear beam core can be seen in the right image in Figure 7.3. An adjusted color representation reveals the expected concentric rings, shown in Figure 7.4. The FWHM analysis shown in Figure 7.6 shows that the measurements agree with the simulated point source resolutions. In fact, the measured FWHM are somewhat smaller than the simulated FWHM. However, the measured DoF falls short at only 36% of the DoF predicted by the simulation, at 14.5 mm instead of 40 mm. In images thereafter ring shaped illumination is observed, indicating the end of the z_{max} of the Bessel beam. The reason for the difference in theoretical and experimental DoF is not known. A shorter experimental DoF would be expected when smaller lenses or aperture stops are used in the experimental axicon with objective lens set-up but this is not the case.

The incoherent distribution, seen in the left image in Figure 7.3, is less representative of a Bessel distribution. It somewhat resembles the distribution one would expect for an image with spatially overlapping Bessel distributions, similar to the result of the speculative simulation shown in Figure 4.10a. This is accompanied by worse resolution with respect to the coherent case. Similarly, differences in the edge resolution can be seen for the coherent and incoherent resolution target measurements. In both cases the Bessel beam system seems to yield better resolution for coherent illumination than for incoherent illumination.

The 'edge shifting' described for the Gaussian PSF measurements may contribute to the FWHM difference in the Bessel beam system as well. The difference between the coherent and incoherent measurements suggest that the edge shifting that occurs for coherent illumination narrows the coherent intensity distribution such that spatial Bessel distribution overlapping does not occur. If so, a coherently illuminated measurement with a larger aperture should show a similar result to that of the incoherently illuminated point source. Additional measurements show that this is the case. Figure 8.2 shows measurements with coherent light for larger apertures at 5.5 mm from the objective lens (as in Figure 7.3). Figure 8.2a displays the image created with a 15

µm diameter aperture. Overlap of Bessel distributions can be seen, resulting in multiple beam cores. Figure 8.2b displays the image created with a 150 µm diameter aperture. For this measurement a painted white glass plate is used to diffuse the laser light before it enters the large aperture and a camera integration time of 1 s was used instead of 0.01 s. Overlap of numerous Bessel distributions can be seen, resulting in a fairly chaotic display of specks.

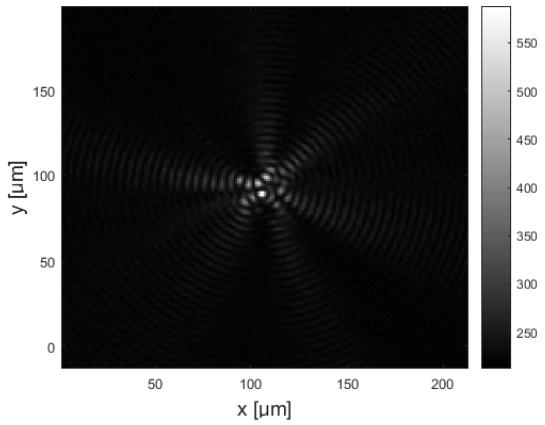

(a) Bessel PSF measurement of a 15 µm aperture with coherent illumination.

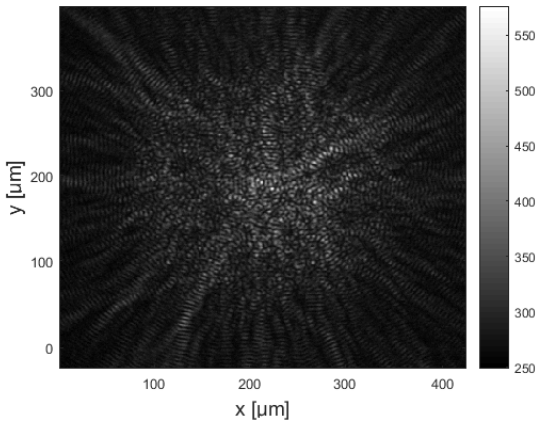

(b) Bessel PSF measurement of a 150 µm aperture with coherent illumination.

Figure 8.2: Coherently illuminated Bessel PSF measurements of larger apertures at z = 5.5 mm from the objective lens.

Regarding the resolution target measurements, one would expect to see Bessel profiles in the images of the resolution target imaged with the coherent Bessel set-up, as was the case for the PSF measurements with coherent Bessel set-up and the Bessel beam simulations. However, in Figure 7.9 Bessel profiles are not visible. A dense line structure can be seen. This is likely due to many Bessel distributions and interference effects. A deconvolution with either a simulated or the measured Bessel PSF profile does not result in removal of these structures. The FWHMs are larger than the beam core FWHMs found in the coherent Bessel PSF measurements. The DoF is also much larger and during measuring the target elements, be it vaguely, could still be seen with the target as far as 9 cm from the imaging system. It is possible that this is due to the Talbot effect [17], where the image of a periodic diffraction grating is repeated at regular distances from the grating plane.

The incoherent resolution target measurements show larger FWHM values than the coherent measurements. Conventionally, one would expect this to be the other way around, due to interference along the edges in the coherent case. However, as mentioned earlier the means of illumination seems to have a large influence on the image resolution for the Bessel beam system. Also, the 'Knife Edge' function fit seems to disregard the oscillations along the edge in the coherent illumination case which results in lower FWHM values.

During the execution of the practical work the imaging system with axicon has shown to be very sensitive to small changes in set-up. Extremely small changes in distance between the objective lens and the axicon, denoted by s in Figure 4.8, resulted in large changes in image size.

The method of illumination is of major influence on the resulting images. As mentioned in Chapter 6 paraxial coherent illumination of the resolution target did not yield usable images at all. The subsequent slight oblique illumination has effects on the axicons diffraction patterns which in turn may impede deconvolution with a circularly symmetric Bessel distribution.

8.3. Recommendations

In this section several recommendations for further research are made.

Illumination

For the Bessel beam system, the influence of coherent and incoherent illumination on the image resolution has been analysed using the axicon with objective lens model from the literature [50]. The influence of illumi-

nation coherence on the images in a Bessel system may be investigated further with numerical propagation simulations of the axicon with objective lens system with coherent and incoherent illumination.

Experimentally, large differences in resolution were found for incoherent and coherent illumination. A laser and an LED were used as coherent and incoherent light sources. In follow-up experiments an effort should be made to equalize the lighting conditions for the coherent and incoherent light sources to allow for more objective comparison between the two.

Paraxial coherent illumination of the resolution target did not yield usable images, even though basic geometric incident angle calculations did not predict any problems for paraxial illumination. The cause of this is uncertain and calls for further investigation of the influence of illumination on imaging with an axicon. The range of angles over which the system can accept light may be investigated further.

Subsequently, in this work illumination under a slight angle to the optical axis was used to obtain the resolution target images. For these images deconvolution with a circular symmetric Bessel distribution was not succesful. The diffraction effects of oblique illumination of the axicon can be predicted and may be corrected for to facilitate successful deconvolution with non-paraxial illumination.

Regeneration

It is known that Bessel beam regeneration occurs with axicon imaging but the magnitude of its influence on the images obtained in this research is not clear. Further research may clarify whether beam regeneration plays a significant part in the deterioration of the resolution witnessed in the experimental results. If so, axicons with a lower base angle can be used to reduce regeneration effects. A lower base angle axicon will yield a longer obstruction shadow, as shown in Figure 8.3. An optimum will have to be found, as use of a lower base angle axicon will also go paired with a wider beam core analogue to a lower resolution.

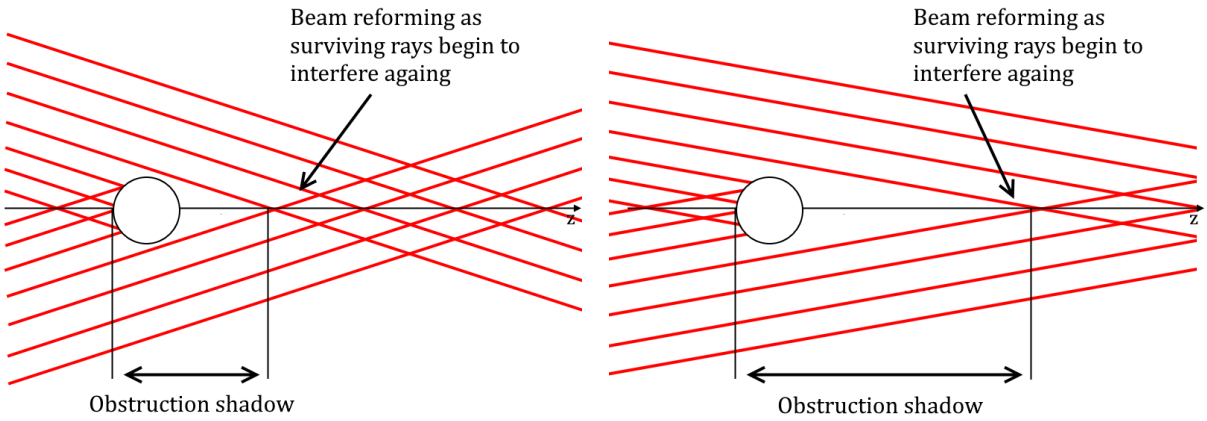

(a) Self-regeneration of a Bessel beam generated by an axicon with a relatively high base angle. The obstruction shadow is shorter than in Figure 8.3b.

(b) Self-regeneration of a Bessel beam generated by an axicon with a relatively low base angle. The obstruction shadow is longer than in Figure 8.3a.

Figure 8.3: Self-regeneration for axicon generated Bessel beams for axicons with high and low base angles. Source: adaptation of [36].

Applications

The use of Bessel beams in optical imaging shows a significant increase in DoF. But for large objects spatial overlapping of the Bessel distributions has a negative effect on resolution. For this reason, Bessel imaging without spatial filtering is particularly suitable for applications where a large DoF is desired and high resolution is less of a priority. Furthermore, widefield Bessel imaging may be useful for imaging and OPT of very sparse but large objects. The benefits of the high intensity core of Bessel beams may be used in scanning applications by aperturing the beam, ignoring the rest of the Bessel distribution. Bessel beam imaging combined with spatial filtering has already shown its use in providing the distribution of incoherent emission collected in the optical axis as a function of depth [22].

8.4. OPT Outlook

Exploratory transmission OPT measurements have been performed for qualitative evaluation. The set-up used for the resolution target measurements has been used to perform transmission OPT with the incoherent light source (LED operating at maximum power of 5 W). A cylindrical sample with a diameter of 1.3 mm contains ceramic beads with a diameter of 63-125 µm (SiLibeads 94003) in 2% low melting point agarose gel. A total of 359 projections are made with 1° intervals with the sample at a distance of 2 cm from the objective lens using a motorized stage assembly. The assembly performs x, y and z translation (8MT167M-25LS, Standa) as well as a θ rotation (8MR151, Standa). Fine tuning of the sample position is done with an x-y translation mount (SCP05, Thorlabs), and a tip-tilt mount (KC05-T/M, Thorlabs). The agarose sample is glued to a metal cylinder attached to the lower end of the tip-tilt mount.

Figure 8.4a shows a side-view image of the sample. The cylindrical sample is set-up in the vertical z-direction. The blue arrows indicate the positions of four ceramic beads. The contrast is quite poor. Figure 8.4b shows a reconstructed slice of the OPT measurements. Even though averaged background subtraction is performed not much can be seen. As the unprocessed reconstruction does not show distinguishable objects a 2D Gaussian filter is applied in Matlab using `imgaussfilt` with a smoothing kernel with a standard deviation of 1. The result is shown in Figure 8.4c. A bead can be recognized, but both the contrast and the resolution are low.

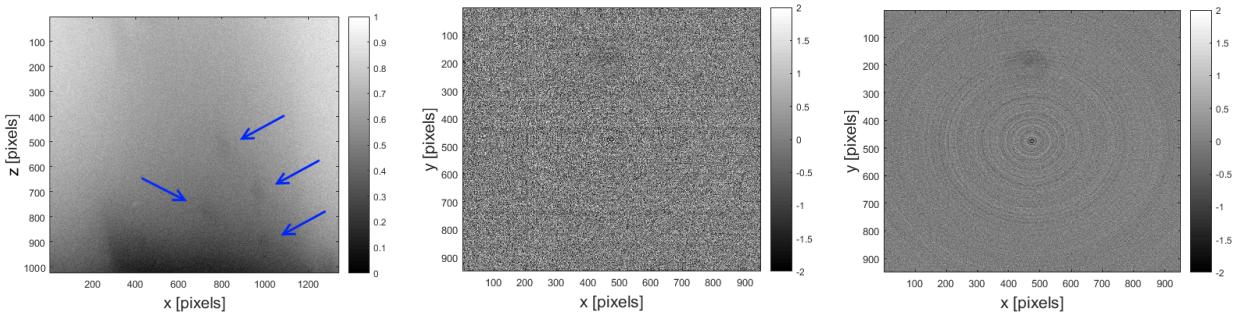

(a) **(b)** **(c)**

Figure 8.4: Transmission OPT image, slice reconstruction and processed slice reconstruction.

The OPT result is not usable for meaningful qualitative comparison with OPT simulations due to its low quality. Contrast may be improved if a more powerful light source is used. As stated in Section 8.3, the influence of regeneration is not known and may account for the poor contrast. With that in mind, emission OPT with small light sources may yield images with higher resolution.

A

Other Non-Diffracting Beams

In this appendix some additional non-diffracting beams to the Bessel beams are discussed and the choice to use the Bessel beam for further research in DoF extension in OPT is explained.

The non-diffracting beams mostly found in the literature, besides the Bessel beam, are the Airy, Mathieu and Weber beams. They are discussed in this section.

Airy

Unlike ordinary optical wavefronts, Airy beams show transversal acceleration throughout propagation. That is, they self-bend and the intensity peaks of Airy beams follow parabolic trajectories [5]. A typical example of Airy beam propagation is shown in Figure A.1. In spite of their inherent bending, Airy beams exhibit shape-invariant propagation. They have been found to be remarkably unaffected by perturbations and show regeneration if they are affected. Like the Bessel beam, these qualities show potential for use in OPT as they may be used in turbid systems where scattering is an issue. Airy beams have shown their use in optical trapping on many occasions and have more recently been used for super-resolution imaging of molecules [23].

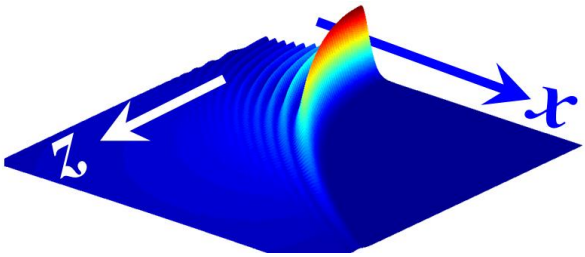

Figure A.1: Typical propagation of an Airy beam with propagation direction z.
Source: *http://www.nonlinearphotonics.com/research/nonlinear-and-singularity-optics/linear-and-nonlinear-control-of-airy-beams/*

Spatial Light Modulators, or SLM's, are devices that are used to spatially modulate the amplitude and phase of an optical wavefront in two dimensions. SLM's can be programmed to produce light beams with optical wavefronts using numerically defined phase elements, essentially replacing real phase masks. Figure A.2a shows a continuous cubic phase pattern that is used to optically reconstruct the finite-energy Airy beam in Figure A.2b [37].
SLM's use liquid crystals. The optical properties of the liquid crystals are modified by means of an electric field. This technique makes SLM's rather complex and expensive devices.

Even though Airy beams have extended DoF's and are resilient to perturbations, the bending behaviour and the lack of rotational symmetry combined with many sidelobes may make them less suited for application in OPT and than Bessel beams.

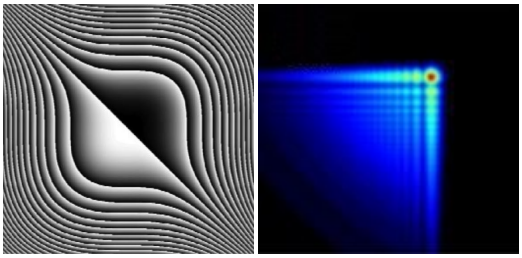

(a) Airy phase pattern. Source: [37]

(b) Resulting Airy profile after some propagation. Source: [37]

Figure A.2: Binary Bessel phase pattern and corresponding beam. Airy cubic phase pattern and corresponding beam.

Mathieu

Based on the separability of the Helmholtz equation into elliptical cylindrical coordinates, an analytic formulation of invariant optical fields has been presented [19]. Again, characteristics include a highly localized intensity distribution along one of the transverse directions and a peaked quasi-periodic structure along the other transverse direction, as can be seen in Figure A.3a. As these fields are described by the Mathieu functions that are exact solutions of the Helmholtz equation, they have been called Mathieu beams. Examples of the intensity profile and the evolution of a Mathieu beam are shown in Figure A.3. An approximation to the theoretical Mathieu beam has been realised experimentally using a line illumination, a circular slit and a lens as shown in Figure A.4 [18]. An application of the experimental Mathieu beam in optics has not been found in the literature.

Weber

Another type of non-diffracting waves is found as spatially accelerating solutions of the Maxwell equations: the Weber waves [4]. Weber waves propagate in parabolic trajectories and again, these waves show self-healing properties. The earlier discussed Airy beam is considered a special case of the Weber beams at the paraxial limit [52] and Weber beams can be described by a modulated Airy function [4]. They are not known to be used in optics.

Both Mathieu and Weber beams have non-paraxial accelerating variants which bend into large angles along circular, elliptical, or parabolic trajectories but still retain non-diffracting and self-healing capabilities [52]. There are many more examples of the complex non-diffracting beam shapes that can be found with wave-packets and other techniques, but these wave shapes are deemed too complex for use in OPT.

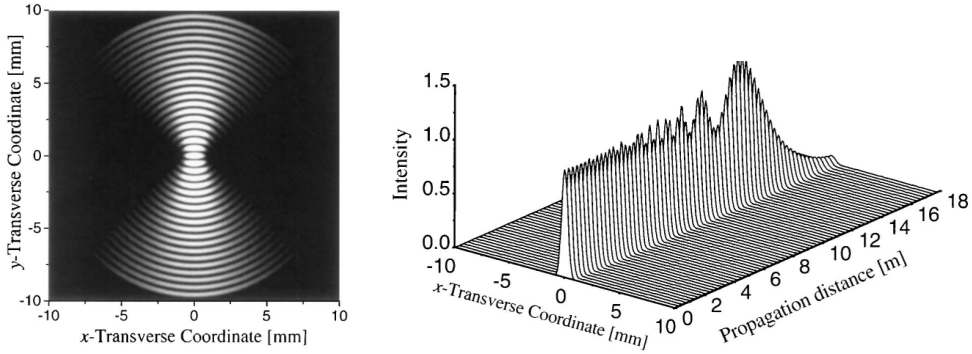

(a) Transverse intensity pattern of a zero-order Mathieu beam

(b) Evolution of an apertured Mathieu beam

Figure A.3: Mathieu beam profiles, source: [19]

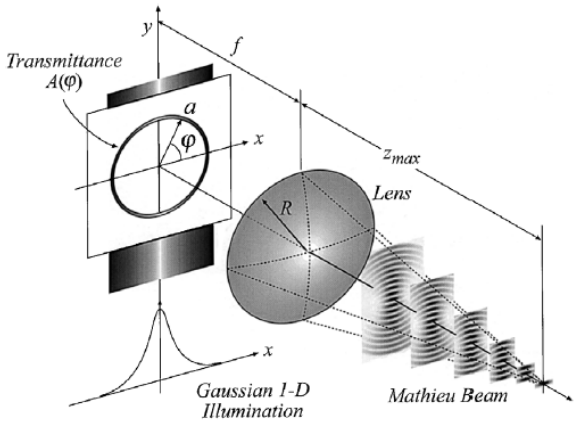

Figure A.4: Experimental generation of the zero-order Mathieu beam. Source: [18]

Non-Diffracting Beams in OPT

Both the Bessel and the Mathieu beams display straight transversal high-intensity centre cores, a property that makes them practical for use in OPT. Of all the investigated beams only the Bessel beam shows circular symmetry. Also, Bessel beams are more easily constructed than the other non-diffracting beams that have been discussed. Bessel beams with a finite range of uniform intensity distribution can be constructed from conventional beams such as the Gaussian beam without loss of energy with axicon lenses. For this reasons the application of axicon lens generated Bessel beams in OPT is chosen for further research.

B

Hankel Transform and the Circularly Symmetric Fourier Transform

This appendix contains a brief explanation of how the Hankel transform and the circularly symmetric Fourier transform are related [3].

The zeroth order Hankel transform of a function $f(r)$ can be written as

$$H_0(k) = \int_0^\infty f(r) J_0(kr)\, r\, dr. \tag{B.1}$$

For a 2-dimensional function $f(r)$ with radial component r, the Fourier transform is

$$F(k) = \int\int f(r) e^{ikr}\, dr \tag{B.2}$$

Switching to a polar coordinate system (r,θ), the Fourier transform can be written as

$$F(k) = \int_{r=0}^\infty \int_{\theta=0}^\infty f(r,\theta) e^{ikrcos(\theta)}\, r\, dr\, d\theta. \tag{B.3}$$

In the case of circular symmetry for f, there is no dependence on the angular variable θ. After integration over θ the Fourier transform can be written as

$$F(k) = 2\pi \int_0^\infty f(r) J_0(kr)\, r\, dr, \tag{B.4}$$

which is the zero-order Hankel transform H_0 of $f(r)$ times 2π.

C

Axicon with Objective Lens Model

This Appendix contains a brief overview of the equations used in the model that describes the intensity distribution of an illuminated axicon with an objective lens. For a more detailed explanation the reader is referred to the original work by Zhongsheng Zhai and Bin Zhao [50].

An axicon illuminated by a plane wave

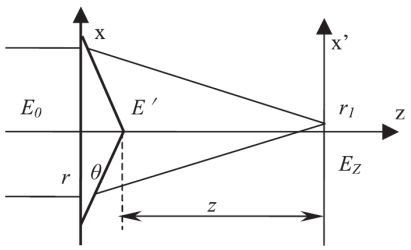

Figure C.1: An axicon illuminated by a diverging wave.

The intensity distribution at distance z for an axicon illuminated by a plane wave, as in Figure C.1, can be described by

$$I(r_1) \approx k^2(n-1)^2\theta^2 z\lambda |J_0[k(n-1)\theta r_1]|^2 + \left[\frac{DJ_0\left(\frac{kDr_1}{2z}\right)}{D-2(n-1)z\theta}\right]^2 - \frac{2k(n-1)\theta D\sqrt{z\lambda}}{D-2(n-1)z\theta} \times J_0\left(\frac{kDr_1}{2z}\right) J_0[k(n-1)\theta r_1] \times \cos\left\{\frac{k}{2z}\left[\frac{D}{2} - (n-1)\theta z\right]^2 + \frac{\pi}{4}\right\},$$

where k denotes the wavenumber, n denotes the refraction index of the axicon, D denotes the axicon diameter, θ denotes the axicon base angle, λ denotes the wavelength and r_1 is the radial component.

An axicon illuminated by a converging wave

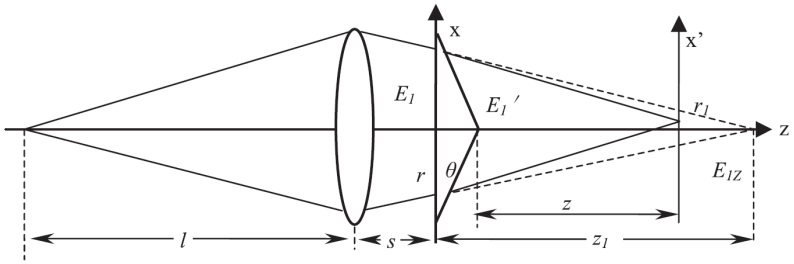

Figure C.2: An axicon illuminated by a converging wave.

Figure C.2 shows an axicon illuminated by a converging wave. Here, l denotes the object distance, s denotes the distance between the objective lens and the axicon and f denotes the focal length of the objective lens. $z_1 = \frac{lf}{l-f} - s$ is the converging radius and $r_{1p} = \frac{zz_1}{z_1-z}(n-1)\theta$ is the stationary point r_{1p}. The intensity distribution at distance z can be described by

$$I(r_1) \approx k^2 r_{1p}^2 \frac{1}{zz_1(z_1-z)\lambda}\left[J_0\left(k\frac{r_{1p}}{z}r_1\right)\right]^2 + \left[\frac{D}{D(z_1-z)-2(n-1)zz_1\theta}J_0\left(\frac{kDr_1}{2z}\right)\right]^2$$
$$-\frac{\frac{2kDr_{1p}}{zz_1}\sqrt{\frac{zz_1}{z_1-z}}\lambda}{D(z_1-z)-2(n-1)zz_1\theta}J_0\left(\frac{kDr_1}{2z}\right)\times J_0\left(k\frac{r_{1p}}{z}\right)\cos\left\{\frac{k(z_1-z)}{2zz_1}\times\left[\frac{D}{2}-(n-1)\theta\frac{zz_1}{z_1-z}\right]^2+\frac{\pi}{4}\right\},$$

where k denotes the wavenumber, n denotes the refraction index of the axicon, D denotes the axicon diameter, θ denotes the axicon base angle, λ denotes the wavelength and r_1 is the radial component.

An axicon illuminated by a diverging wave

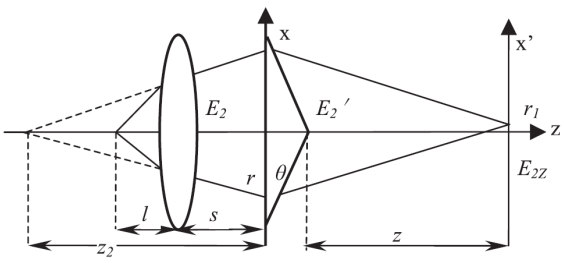

Figure C.3: An axicon illuminated by a diverging wave.

Figure C.3 shows an axicon illuminated by a diverging wave. Here, l denotes the object distance, s denotes the distance between the objective lens and the axicon and f denotes the focal length of the objective lens. $z_2 = \frac{lf}{f-l} + s$ is the converging radius and $r_{2p} = \frac{zz_2}{z_2+z}(n-1)\theta$ is the stationary point r_{2p}. The intensity distribution at distance z can be described by

$$I(r_1) \approx k^2 r_{2p}^2 \frac{1}{zz_2(z_2+z)\lambda}\left[J_0\left(k\frac{r_{2p}}{z}r_1\right)\right]^2 + \left[\frac{D}{D(z_2+z)-2(n-1)zz_2\theta}J_0\left(\frac{kDr_1}{2z}\right)\right]^2$$
$$-\frac{\frac{2kDr_{2p}}{zz_2}\sqrt{\frac{zz_2}{z_2+z}}\lambda}{D(z_2+z)-2(n-1)zz_2\theta}J_0\left(\frac{kDr_1}{2z}\right)\times J_0\left(k\frac{r_{2p}}{z}\right)\cos\left\{\frac{k(z_2+z)}{2zz_2}\times\left[\frac{D}{2}-(n-1)\theta\frac{zz_2}{z_2+z}\right]^2+\frac{\pi}{4}\right\},$$

where k denotes the wavenumber, n denotes the refraction index of the axicon, D denotes the axicon diameter, θ denotes the axicon base angle, λ denotes the wavelength and r_1 is the radial component.

Bibliography

[1] The measurement of a transverse profile of laser beam by Knife Edge method. `people.fjfi.cvut.cz/blazejos/public/ul7en.pdf`, 2013. [Online; accessed 2018].

[2] Marcelino Anguiano-Morales, Marcela M Mendez-Otero, Marcelo David Iturbe-Castillo, and Sabino Chávez-Cerda. Conical dynamics of bessel beams. *Optical Engineering*, 46(7):078001, 2007.

[3] Natalie Baddour. Two-dimensional fourier transforms in polar coordinates. In *Advances in Imaging and Electron Physics*, volume 165, pages 1–45. Elsevier, 2011.

[4] Miguel A Bandres and BM Rodríguez-Lara. Nondiffracting accelerating waves: Weber waves and parabolic momentum. *New Journal of Physics*, 15(1):013054, 2013.

[5] Miguel A Bandres, Ido Kaminer, Matthew Mills, BM Rodríguez-Lara, Elad Greenfield, Morderchai Segev, and Demetrios N Christodoulides. Accelerating optical beams. *Optics and Photonics News*, 24(6):30–37, 2013.

[6] Zhao Bin and Li Zhu. Diffraction property of an axicon in oblique illumination. *Applied Optics*, 37(13): 2563–2568, 1998.

[7] Oto Brzobohatỳ, Tomáš Čižmár, and Pavel Zemánek. High quality quasi-bessel beam generated by round-tip axicon. *Optics express*, 16(17):12688–12700, 2008.

[8] JP Campbell and LG DeShazer. Near fields of truncated-gaussian apertures. *JOSA*, 59(11):1427–1429, 1969.

[9] Lingling Chen, Natalie Andrews, Sunil Kumar, Paul Frankel, James McGinty, and Paul MW French. Simultaneous angular multiplexing optical projection tomography at shifted focal planes. *Optics letters*, 38(6):851–853, 2013.

[10] Tomás Cizmár. *Optical traps generated by non-traditional beams*. PhD thesis, Ph. D. thesis, Masaryk University in Brno, 2006.

[11] Tomáš Čižmár and Kishan Dholakia. Axial intensity shaping of a bessel beam. In *Optical Trapping and Optical Micromanipulation VI*, volume 7400, page 74001Q. International Society for Optics and Photonics, 2009.

[12] Philip S Considine. Effects of coherence on imaging systems. *JOSA*, 56(8):1001–1009, 1966.

[13] J Durnin. Exact solutions for nondiffracting beams. i. the scalar theory. *JOSA A*, 4(4):651–654, 1987.

[14] J1 Durnin, JJ Miceli Jr, and JH Eberly. Diffraction-free beams. *Physical review letters*, 58(15):1499, 1987.

[15] Florian O Fahrbach and Alexander Rohrbach. Propagation stability of self-reconstructing bessel beams enables contrast-enhanced imaging in thick media. *Nature communications*, 3:632, 2012.

[16] Richard Fitzgerald. Phase-sensitive x-ray imaging. *Phys. Today*, 53(7):23–26, 2000.

[17] Joseph Goodman. Introduction to fourier optics. 2008.

[18] JC Gutiérrez-Vega, MD Iturbe-Castillo, GA Ramırez, E Tepichın, RM Rodrıguez-Dagnino, S Chávez-Cerda, and GHC New. Experimental demonstration of optical mathieu beams. *Optics Communications*, 195(1-4):35–40, 2001.

[19] Julio C Gutiérrez-Vega, MD Iturbe-Castillo, and S Chávez-Cerda. Alternative formulation for invariant optical fields: Mathieu beams. *Optics letters*, 25(20):1493–1495, 2000.

[20] Marko Honkanen and Jari Turunen. Tandem systems for efficient generation of uniform-axial-intensity bessel fields. *Optics communications*, 154(5-6):368–375, 1998.

[21] David Huang, Eric A Swanson, Charles P Lin, Joel S Schuman, William G Stinson, Warren Chang, Michael R Hee, Thomas Flotte, Kenton Gregory, Carmen A Puliafito, et al. Optical coherence tomography. *Science*, 254(5035):1178–1181, 1991.

[22] Ignacio Iglesias. Using axicons for depth discrimination in excitation-emission laser scanning imaging systems. *Optics & Laser Technology*, 95:8–13, 2017.

[23] Shu Jia, Joshua C Vaughan, and Xiaowei Zhuang. Isotropic three-dimensional super-resolution imaging with a self-bending point spread function. *Nature photonics*, 8(4):302, 2014.

[24] Avinash C.. Kak and Malcolm Slaney. *Principles of computerized tomographic imaging*. IEEE press New York, 1988.

[25] Kye-Sung Lee and Jannick P Rolland. Bessel beam spectral-domain high-resolution optical coherence tomography with micro-optic axicon providing extended focusing range. *Optics letters*, 33(15):1696–1698, 2008.

[26] Linbo Liu, Cheng Liu, Wong Chee Howe, CJR Sheppard, and Nanguang Chen. Binary-phase spatial filter for real-time swept-source optical coherence microscopy. *Optics letters*, 32(16):2375–2377, 2007.

[27] Dirk Lorenser, C Christian Singe, Andrea Curatolo, and David D Sampson. Energy-efficient low-fresnel-number bessel beams and their application in optical coherence tomography. *Optics letters*, 39(3):548–551, 2014.

[28] David McGloin and Kishan Dholakia. Bessel beams: diffraction in a new light. *Contemporary Physics*, 46 (1):15–28, 2005.

[29] John H McLeod. The axicon: a new type of optical element. *JOSA*, 44(8):592–597, 1954.

[30] Yi Hong Ong and Quan Liu. Axicon lens-based cone shell configuration for depth-sensitive fluorescence measurements in turbid media. *Optics letters*, 38(15):2647–2649, 2013.

[31] Yi Hong Ong and Quan Liu. Fast depth-sensitive fluorescence measurements in turbid media using cone shell configuration. *Journal of Biomedical Optics*, 18(11):110503, 2013.

[32] Thomas A Planchon, Liang Gao, Daniel E Milkie, Michael W Davidson, James A Galbraith, Catherine G Galbraith, and Eric Betzig. Rapid three-dimensional isotropic imaging of living cells using bessel beam plane illumination. *Nature methods*, 8(5):417, 2011.

[33] Fränze Progatzky, Margaret J Dallman, and Cristina Lo Celso. From seeing to believing: labelling strategies for in vivo cell-tracking experiments. *Interface focus*, 3(3):20130001, 2013.

[34] Mounika Rapolu, Hubert Dolezyczek, Szymon Tamborski, Monika Malinowska, Grzegorz Wilczynski, Maciej Szkulmowski, and Maciej Wojtkowski. Bessel beam ocm for analysis of global ischemia in mouse brain. In *European Conference on Biomedical Optics*, page 1041609. Optical Society of America, 2017.

[35] Andrew Grey Saikaley. *Imaging, characterization and processing with axicon derivatives*. PhD thesis, Laurentian University of Sudbury, 2013.

[36] David S Simon. A guided tour of light beams. *A Guided Tour of Light Beams*, page 11, 2016.

[37] GA Siviloglou, J Broky, Aristide Dogariu, and DN Christodoulides. Observation of accelerating airy beams. *Physical Review Letters*, 99(21):213901, 2007.

[38] S Stallinga. Imaging systems, lecture notes, 2017.

[39] Paul A Tipler and Gene Mosca. *Physics for scientists and engineers*. Macmillan, 2007.

[40] Anna K Trull, Jelle van der Horst, Willem Jan Palenstijn, Lucas J van Vliet, Tristan van Leeuwen, and Jeroen Kalkman. Point spread function based image reconstruction in optical projection tomography. *Physics in Medicine & Biology*, 62(19):7784, 2017.

[41] Anna K Trull, Jelle van der Horst, Lucas J van Vliet, and Jeroen Kalkman. Comparison of image reconstruction techniques for optical projection tomography. *Applied optics*, 57(8):1874–1882, 2018.

[42] J van der Horst. High-resolution deep-tissue quantitative optical tomography. 2018.

[43] Jelle van der Horst and Jeroen Kalkman. Image resolution and deconvolution in optical tomography. *Optics express*, 24(21):24460–24472, 2016.

[44] David George Voelz. *Computational fourier optics: a MATLAB tutorial*. SPIE press Bellingham, WA, 2011.

[45] Johnathon R Walls, John G Sled, James Sharpe, and R Mark Henkelman. Resolution improvement in emission optical projection tomography. *Physics in Medicine & Biology*, 52(10):2775, 2007.

[46] Niklas Weber, Dominik Spether, Andreas Seifert, and Hans Zappe. Highly compact imaging using bessel beams generated by ultraminiaturized multi-micro-axicon systems. *JOSA A*, 29(5):808–816, 2012.

[47] Walter Thomson Welford. Use of annular apertures to increase focal depth. *JOSA*, 50(8):749–753, 1960.

[48] Dean Wilding, Paolo Pozzi, Oleg Soloviev, Gleb Vdovin, Colin J Sheppard, and Michel Verhaegen. Pupil filters for extending the field-of-view in light-sheet microscopy. *Optics letters*, 41(6):1205–1208, 2016.

[49] Jingchao Xing, Junyoung Kim, and Hongki Yoo. Design and fabrication of an optical probe with a phase filter for extended depth of focus. *Optics Express*, 24(2):1037–1044, 2016.

[50] Zhongsheng Zhai and Bin Zhao. Diffraction intensity distribution of an axicon illuminated by polychromatic light. *Journal of Optics A: Pure and Applied Optics*, 9(10):862, 2007.

[51] Zhongsheng Zhai, Shanting Ding, QingHua Lv, Xuanze Wang, and Yuning Zhong. Extended depth of field through an axicon. *Journal of modern Optics*, 56(11):1304–1308, 2009.

[52] Peng Zhang, Yi Hu, Tongcang Li, Drake Cannan, Xiaobo Yin, Roberto Morandotti, Zhigang Chen, and Xiang Zhang. Nonparaxial mathieu and weber accelerating beams. *Physical review letters*, 109(19):193901, 2012.

[53] Dan Zhu, Kirill V Larin, Qingming Luo, and Valery V Tuchin. Recent progress in tissue optical clearing. *Laser & photonics reviews*, 7(5):732–757, 2013.